SINGLE-CELL CHARACTERISATION OF AGEING AND DISEASE

Simon Besson-Girard

8th May 2023

Dissertation der
Graduate School of Systemic Neurosciences der
Ludwig-Maximilians-Universität
München

This dissertation was submitted to LMU Munich in fulfillment of the requirements for a PhD at the Graduate School for Systemic Neurosciences.

The presented research works were conducted in the Systems Neuroscience group of the Institute for Stroke and Dementia Research (ISD) under the supervision of Dr. Özgün Gökçe.

Simon Besson-Girard: *Single-cell characterisation of ageing and disease*.
8th May 2023

Supervisor
Dr. Özgün Gökçe

Institute for Stroke and Dementia Research (ISD)
Klinikum der Universität München

Second reviewer
Prof. Dr. Wolfgang Enard

Chair of Anthropology and Human Genomics
Ludwig-Maximilians University Munich (LMU)

Thesis defended on 29th September, 2023

The noblest pleasure is the joy of understanding.

— Leonardo da Vinci

Dedicated to the Besson-Girard family.

ABSTRACT

Over the last decade, emerging single-cell technologies triggered a revolution in our perception of biological systems. While new library generation methods flourished and precipitated a deeper understanding of the mechanisms of life, novel computational analyses saw the light, permeabilising even further the boundaries of the field.

Systemic approaches, by the large scope and complexity that they aim to cover, particularly benefited from this leap. Unravelling the heterogeneity of cells identities is key to understanding their states dynamic and how they influence each others with regards to the host phenotype.

In this cumulative thesis, we present two articles that highlight ageing immune mechanisms as fertile soil for the emergence of neurodegeneration. We demonstrated the critical influence of the cell location on the gene expression and cellular state, especially in the white-matter, a lipid-rich region of the parenchyma that is particularly susceptible to ageing and neurodegeneration.

The first article focuses on a microglial population found in the ageing white matter: the white matter associated microglia (WAM). We show that WAM formation is dependent on TREM2 but not APOE. WAMs present pathways significantly enriched in lipid processing and antigen presentation. They cluster in nodules and are engaged in clearing the myelin degradation accumulating in ageing.

The second article complements the WAM study by exploring further the antigen presentation mechanisms. It also focuses on the question of white-matter volume loss more directly. We show that CD8 T cells, by crossing the blood-brain barrier, and entering the immunologically priviledged central nervous system, play a role in oligodendrocyte degeneration, notably by secretion of interferon-γ, that we confirm to be detrimental specifically in the aged brain.

Overall, we deliver new arguments to enrich the dichotomic debate on the good and bad role of microglia in ageing and disease. Furthermore, we illustrate the current trajectory of single-cell-enriched research at the interface of the neuroscience and immunology fields. We provide revolutionary insights revealing the importance of the location, signalling and environmental context of a cell in the shaping of its identity and the functions that it carries. Identifying further the mechanisms of ageing draws an optimistic horizon for the future of medical treatment and life improvement in ageing and disease.

Life is pretty simple: You do some stuff. Most fails. Some works. You do more of what works. If it works big, others quickly copy it. Then you do something else. The trick is the doing something else.

— Leonardo da Vinci

ACKNOWLEDGMENTS

TO MY TAC MEMBERS

These last years, dedicated to my scientific and personal growth, were the most gratifying of my life. My doctoral studies were like nothing I could anticipate. Today, I feel proud of what we achieved. Everyone with whom I interacted, contributed in some ways to influencing decisions, stimulating creativity, challenging beliefs and supporting our work.

I grant my eternal gratitude to the prime supervisor of my studies, Dr. Özgün Gökçe. He showed a passionate commitment to realising ourselves as scientists and carved the best out of us. My journey with him starts from an online interview that left me eager for the greatness of what science can achieve. It follows with a continuous growth, a gain of confidence and a built of trust along with the development of the lab for many years. Today, I built a clear scientific thinking process, and I can clearly see my inheritance from these shared years. Thank you oZ for dedicating so much time for me and for trusting me and believing in me as much as you did.

"My mind to your mind. My thoughts to your thoughts." – Commander Spock

I extend my warmest thanks to Prof. Dr. Jürgen Bernhagen. For many years we shared our weekly lab meetings. I then directly benefited from his profound experience and his joy for the work that was presented. His lab was my reference point to materialising what is a pure biological lab and the knowledge and practices it involves. He therefore, indirectly but considerably, helped me erode my impostor syndrome as I was entering a new field involving pipettes and a bench. Without him, this thesis would be considerably different.

I express my deep appreciation to Prof. Dr. Mikael Simons. He took a consistently increasing importance into my projects which culminated in a major publication. I am grateful to him for letting me be a part of this scientific journey and witness the science in the making by his side.

Finally, I would like to thank Prof. Dr. Wolfgang Enard. Our interactions were punctual but regular during my studies. Your willingness to share your knowledge and the availability of your lab members were catalytic factors to our projects.

TO MY COLLEAGUES

I believe that personal well-being, construction of confidence, and being part of a group dynamic, are critical factors for continuing the good work and stay positive along the doctorate. I worked in a lively and cheerful environment, surrounded by fantastic colleagues; most of them became good friends.

Fumi, as a colleague, was a model when building the molecular biology skills I have today and she accompanied me when we built the single-cell library preparation pipeline. As a friend, we shared long conversations and considerations about life. On multiple occasions her advice influenced important decisions when I was hesitant.

Buket welcomed me into the team like if I was a part of it for a long time already. I can't thank her enough for all the translations and considerable amount of phone calls on my behalf. Sorry again for formatting your hardrive containing important confocal data.

"If you don't have your data in three places, you don't have data." – oZ

Leo and I kept each other motivated to learn the hidden secrets of the wet-lab work. We shared genuine moments during our road-trip to France.

Hao was the first of a new wave of colleagues who pushed the wheel of productivity to a next level. It was a pleasure to transmit, interact and learn from you. As desk-mates, we shared a diversity of little moments that constitute the daily-life.

Tugberk arrived to uplift the computational power and provide critical additions to the continuously improving analysis pipeline. I am grateful for your valuable contributions to the WAM paper.

Laura surprised everyone with her clarity of mind. I thank you for preventing me to fall into a routine and reminding me to keep questioning the logic and concepts.

Peter represents for me the longer term direction of the lab. I found in you a person with whom I could share my ambitions and personal approach of the future of biological research.

The presence of Katrin in the scientific taskforce gives me full confidence in the future of research.

Some stayed a shorter time but left a significant contribution: Christine, Jona, Konstantinos, Laura, Elena, ...

From the lab of Prof. Bernhagen, I would like to mention particularly Markus for showing me the biotinylation of MIF. This was my first serious bench lab experiment in the lab. Christine rapidly became a valuable collaborator for the B Cell projects. I thank Dzmitry for his blunt honesty, Lisa for her playful character, Priscilla, Tarshika, Laura, Michael and Aleks, Simona, Yuan, ... and many others, for all the moments we shared. There are also all the other persons with whom I interacted in our building. By their diversity of characters I found in my colleagues a rich universe to evolve into and to build myself.

TO MY LIFE AFTER WORK

For me, there was a life before and during the PhD. The life before contributed to shaping my character and strengths; but it also accompanied me during the PhD, reacting to this new person I differenciated into.

During my master degree, I belonged to a small clade of atypical biologists, interested into the computational and mathematical abstraction of life. Even during my PhD, most of us stayed in contact and kept each other motivated. Merci les aMIVs. My gratitude extends to my teachers at the time, as they succeeded into forming us to be the next generation of biologists.

The master degree was the initiating spark for entering into the single-cell genomics field. I spent six months in the lab of Dr. Charles Plessy at the RIKEN in Japan. Thank you Charles for fighting for my rights and for making this internship possible. Along with Ophélie and Stephane, I thank you all for the time you spent elevating my computational and scientific practices as well as demystifying the single-cell technologies. It is during that time that I built the first layer of knowledge onto which crystallised the doctorate. This experience influenced the pace and direction of my PhD.

I also received the moral support of a closer circle of friends, such as Pierre, Henri, Elise, and Lucien. I thank you all for the long phone calls, and for your attention and support along these years.

My familial node was a continuous source of encouragement, advice and inspiration. I owe an enormous part of who I am to my grand-mother, I know how proud she would be to see me graduating from my PhD. There is also my uncle. He is essential in the construction of my critical and logical thinking. His clear vision of the language of nature unceasingly shapes how I perceive the world. My mother developed a salutary intuition that guides her life. I think that she transmitted it to me. I personally call this form of intuition "my good star". I believe that it carried me where I am today. I would also like to thank Jean-Bernard, a longtime family friend. I have always admired his fearless approach of life. I grew up with him as a model of what a scientific researcher is and should be.

Hong-Ru, from the first day I saw you in the lab meeting — to your kind message (and I hope you were right), the time spent living on opposite sides of the planet, our moving together with our cats, my proposal, our wedding, and today — I never ceased to take inspiration from you. I came to Munich to make scientific discoveries and change the world, instead I discovered you and changed my world. Since we met, my life found a meaningful path that I follow mindfully. You are the guardian of my values and the key to finding myself.

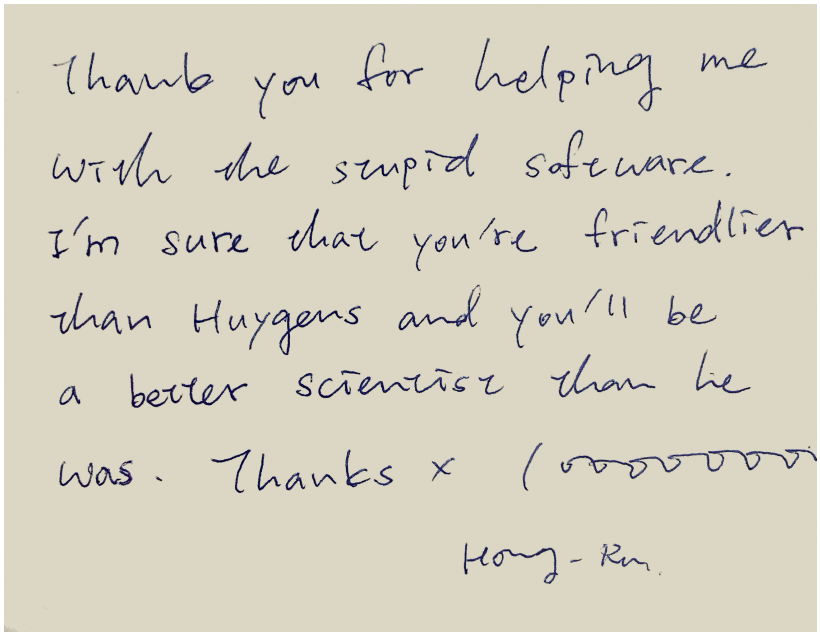

I leave her message here, as a blessing for this thesis. Sorry Huygens!

CONTENTS

LIST OF FIGURES

Part I

INTRODUCTION

In the last decade, while continuously improving on the technical and methodological aspects, single-cell technologies became more accessible. Over the years, this democratisation provided an unprecedented level of details on the mechanisms of ageing and disease. Nowadays, identifying a new and rare population of cells is accessible through commercially available kits. The considerable amount of scientific publications challenges our definitions of cell types and cell states. We are the actors of an ongoing revolution that, more than ever, pushes the boundaries of our understanding of life.

But in my opinion, all things in nature occur mathematically.

— Rene Decartes

1 AGED WHITE-MATTER MICROGLIA

1.1 AGEING AS DRIVER OF NEURODEGENERATION

Ageing is the imprint of time on the living. Because of its inherent nature, what seems to be a triviality needs genuine consideration: ageing is the most prominent risk factor for most neurodegenerative pathologies (Zenin et al., 2019). The institutionalisation of ageing in our contemporary societies might easily lead to forego ageing as a subject of study in the context of research on prominent diseases such as Alzheimer's disease (AD), strongly led by flagship molecules[1] that might shadow other research hypotheses.

[1] *Tau and Aβ are the leading hypotheses in the field*

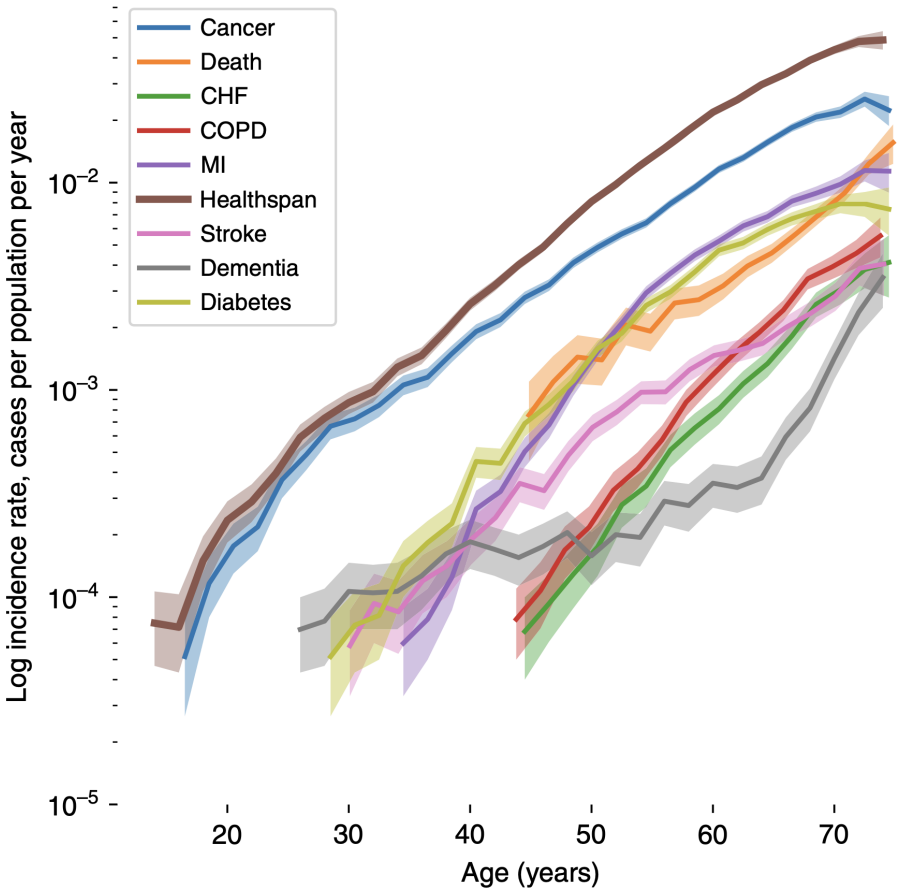

Figure 1: The incidence of the most prevalent chronic diseases – reproduced from Zenin et al., 2019

Figure 1, page 3, from Zenin et al. (2019), depicts the incidence rate of the most prevalent chronic diseases along the age of the in-

dividuals. In this graph, neuropathologies such as AD are grouped under the term "dementia" (in grey), while the regular course of life, disease-free, is indicated as "healthspan" (in brown). Contrary to most diseases, dementia emerges at two different pace, centered around what appears to be an age threshold in that population from the UK. While the evolution of the incidence rate of dementia begins as the slowest compared to the other pathologies, it suddenly presents the fastest acceleration from around 65 years old on. By the time the individuals pass 70 years old, the final incidence of dementia quickly joined the pool of the other most prevalent chronic pathologies related to ageing. In the particular age class of 65 years old, something must be happening in the brain, a change, that will lead to this very acute acceleration of the incidence of dementia.

Ageing appears as a major risk factor for dementia. It is the stage onto which dementia can emerge. Understanding the characteristics of that stage (cellular and molecular ageing processes) is a necessary step to understand why dementia is more prompt to settle in ageing. Acknowledging this fundamental drive, we can approach neuropathologies through the prism of the ageing phenotype, and place ageing at the center of our attention.

1.2 THE AGEING WHITE-MATTER

The phenotype of the ageing brain can be grouped into two components, acting at different scales: structural and molecular changes.

As illustrated in figure 2, page 5, the structural phenotype of the ageing brain is a general atrophy (Blinkouskaya et al., 2021): ventricles are enlarged, gyrification is lost, the cortex thinnens, and the white-matter is degraded.

Among the characteristics of ageing, we focused on the white matter degradation and volume reduction. This phenomenon begins already at around 50 years old in humans (Ge et al., 2002). While the white-matter volume increases slightly between 20 and 40 years old, it only decreases afterwards. This loss progresses in a quadratic manner, to occupy down to 30% of the brain volume by 90 years of age, while it culminated at a maximum average of 40% at around 40 years old (Ge et al., 2002). The pace at which the white-matter volume decreases can even be used to predict the prevalence of cognitive impairment and dementia (Jack et al., 2005).

Conclusions from ageing studies, coupled to Alzheimer's disease risk marker genes, point to immunity changes in ageing. The involve-

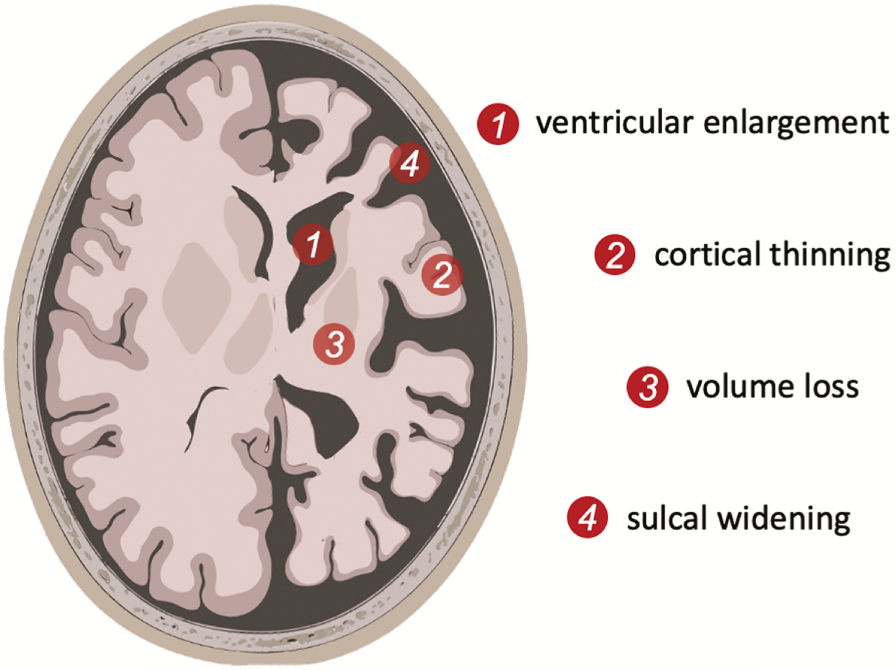

Figure 2: Cerebral atrophy in the ageing brain – reproduced from Blinkouskaya et al., 2021

ment of the immune cells such as microglia became clearer as the field progressed (Hammond et al., 2019).

1.3 MICROGLIA IN THE AGEING BRAIN

Microglia are the brain immune cells. They have multiple roles in both health and disease, as they embrace a large diversity of functions along the life of the individual. They embrace functions of phagocytosis, surveillance, and they are also involved in mechanisms of learning and development (Tremblay et al., 2011).

They are different from most brain cells as they originate from the yolk sac and migrate during development (Kierdorf et al., 2013). In ageing, they are particularly impacted as they get activated, change their morphology from a ramified into an ameboid form and produce several pro-inflammatory cytokines.

The emergence of revolutionary methods of characterisation of single cells have paved the way towards a field-wise race to characterise the diversity of states and the differentiation paths that microglial cells can adopt.

1.4 CELL-FATE AND CELL DIVERSITY

In 1957, in his publication "The Strategy of Genes" (Waddington, 1957), the British biologist Conrad Waddington described a cell fate commitment landscape, that we only begin to delineate through the lens of high resolution methods that are the single-cell omics technologies.

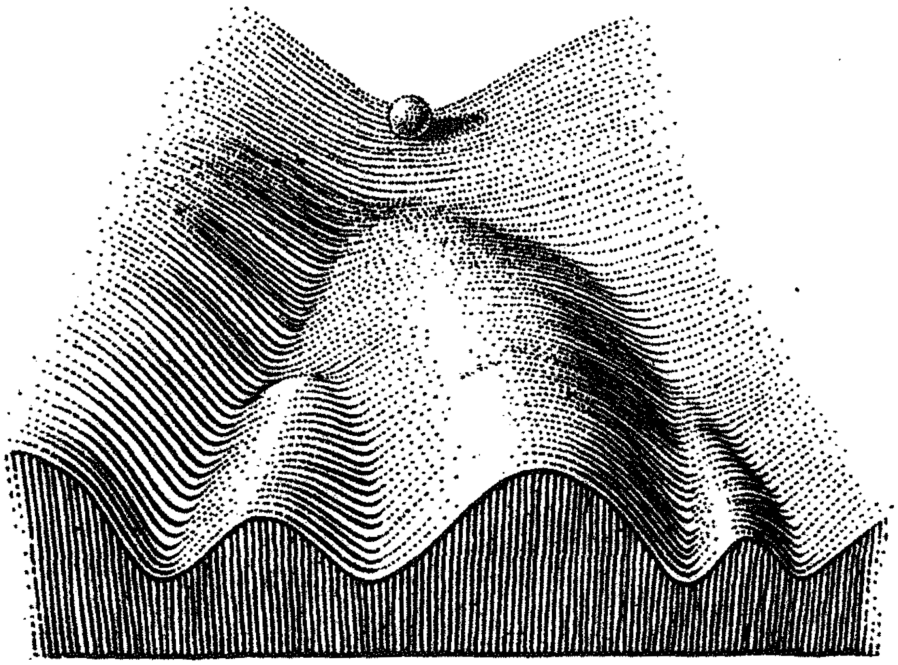

Figure 3: Part of an Epigenetic Landscape – reproduced from Waddington, 1957

Waddington described the ability of single-cells to commit into distinct differentiation and developmental pathways. This differentiation is driven by genes (transcription factors, epigenetic factors, etc.) that, underneath the landcsape, are pulling the valley and pushing the mountains. In this landscape illustrated in figure 3, page 6, cells follow the valley and, like water streams, follow the waterbed, commiting to a singular path when differentiation forks present themselves. Thanks to single-cell -omics technologies, this visual metaphor can nowadays be challenged with extensive details.

1.5 SINGLE-CELL TRANSCRIPTOMICS

Among the single-cell technologies, our main interest here is single-cell transcriptomics (scRNA-seq). scRNA-seq is a method of capture and quantification of the transcriptomic diversity of single cell populations. It presents an instant picture of the transcriptomic land-

scape of samples of interest. This technology was enabled by a series of improvements and innovations that overcame the challenge of single-cell library amplification and multiplexing (Kolodziejczyk et al., 2015).

The ability to study the diversity of the genetic program at the single-cell level is a revolution in contrast to previous bulk approaches. It allows the study of biology at the cellular level, governed by complex gene regulatory networks, that can now be studied in all its diversity. As genes act as a regulatory unit to define a single cell identity, having finally access to the diversity of identities makes it possible to also study cellular interactions and formation of rare populations.

1.6 PATHOLOGICAL STATES: DAM, ARM, MGND MICROGLIA

The possibility to perform *in silico* sorting, unlocked a series of milestone findings that turned obsolete the previous M1 ("bad microglia") / M2 ("good microglia") classification of microglia (Orihuela, McPherson, and Harry, 2016).

The application of scRNA-seq in the study of microglia is marked by the publications of the disease associated microglia (DAM) (Keren-Shaul et al., 2017), activated response micoglia (ARM) (Frigerio et al., 2019), and microglia associated to neurodegeneration (MgND) (Krasemann et al., 2017). These microglial populations were identified in pathological mice models where they identified a continuous state of reactivity of the microglia to its environment. DAM, ARM, MgND were however characterised in the very specific biological context of Alzheimer's disease mouse models; summarising only partially the hallmarks of the disease. Each population presented overlapping gene signatures and functions such as debris clearance. The formation of these population was dependent on the triggering receptor expressed on myeloid cells 2 (TREM2), and the Apolipoprotein E (APOE), whose variants are important risk factors for the emergence of Alzheimers's disease.

TREM2 is a receptor that is expressed on macrophages and microglia, and that binds to anionic molecules such as DNA, gylcoproteins, phospholipids, and in Alzheimer's disease (AD), the amyloid-beta peptide. The activation of this receptor leads to the activation of the microglia and the production of pro-inflammatory cytokines. APOE is a protein that is the principal carrier of cholesterol in the brain and is of importance in AD as it is involved in the clearance of amyloid-beta peptide. The APOE-$\epsilon 4$ allele is associated with an increased risk of Alzheimer's disease.

1.7 STUDYING AGED WHITE-MATTER VIA SCRNA-SEQ

Considering all these elements, we first seeked to explore the microglial diversity of response in ageing. Most specifically, the microglial reactivity towards the decaying myelin in the white-matter. In short, we found that microglia form nodules and are responsible for clearing the accumulating degenerated myelin. We then characterised the gene signature of this special population and found enrichment in the pathways related to phagocytosis and lipid metabolism, but also antigen presentation. This first study was critical to understand the microglial response to degenerated myelin in ageing. However it did not address the white matter volume loss characteristic of ageing. For this, we then focused on oligodendrocytes and T cells, and found both a population of interferon response oligodendrocytes and interferon response microglia in proximity of CD8 T cells. Combined together these studies provide strong material on the critical role of the immune system in ageing and on ageing as a fertile soil for the emergence of neuropathologies.

At the end of the discussion, as an outlook, we will also see that this access to such fine resolution changed the perception of cell states and led to a reorganisation of the field, mostly by challenging our definitions of cell states as we discovered a continuous diversity that contrasted with our regular dichotomous cell-type classification.

2 STRUCTURE OF THIS THESIS

In a few words, this thesis presents single cell studies that aims to understand the interaction between ageing and the role of the immune system. With single-cell transcriptomics approach, we can impute the current states of individual cells, identify populations that react specifically to the ageing condition, and further study their diverse reactions to ageing. This cumulative thesis is organised as follow:

First, we present the starting point of my research, where the WAM microglial population is introduced. *Chapter 3, page 13*

We characterise the transcriptomic signature of a population of microglia that develops specifically with ageing and is located in the white matter. From a technical perspective, this study highlights the importance of associating the location of cells in the analytical process, especially with migrating immune cells such as microglia. In terms of biological knowledge, we identify a new process, and its associated gene signature, by which microglia respond to myelin degeneration during ageing in the white-matter.

Then, we adress more directly the question of the white-matter volume loss in ageing. After the microglia study, we focus mainly on oligodendrocytes, objects of the myelin disruption in ageing. In this publication, we describe a population of interferon responsive oligodendrocytes that interact with CD8 T-cells during ageing. This work puts in relation the CNS specific immunity with the immunity of the rest of the body. We also complement the WAM study with the characterisation of an interferon reactive microglial population. *Chapter 4, page 45*

Finally, we discuss these results and put these findings in perspective to the current knowledge and understanding of the ageing biology. The discussion also extends to a more field-wise reflection of the impact of my work. This is mostly possible because the first article was published 2 years before the completion of this thesis, therefore providing some time to monitor the reception of our publication by the research field. *Chapter 5, page 67*

Part II

RESULTS

After establishing a semi-automated low-volume Smart-seq2 scRNA-seq pipeline in the lab, I optimised the microglial tissue dissociation and library preparation to generate the foundational data and the analytical framework that led to the publication of two major articles, but also many more collaborative projects. The final pipeline provided us with a unique approach on the aged and diseased brain.

Computer Science is no more about computers than astronomy is about telescopes.

— EW Dijkstra

WHITE MATTER AGING DRIVES MICROGLIAL DIVERSITY

3

This article was published in Neuron on 18 February, 2021.

In this article, we aimed to study the microglial response to white matter degeneration. By separating the white- from the gray-matter during the dissociation, we identified a microglial signature that was specific to the white-matter in ageing. We called this population the white matter-associated microglia (WAMs). WAMs presented a signature enriched in immune presentation, phagocytosis and lipid metabolism and shared only a partial signature with the disease-associated microglia (DAM). We further investigated the role of the trigerring receptor expresse on myeloid cells 2 (Trem2) in the apparition of the WAM population and found that Trem2 was necessary for WAMs to develop. However, unlike the DAM, we found WAMs in apolipoprotein E (Apoe) knock-out (KO) mice, showing an independence of WAMs towards Apoe. By reanalysing published data of ageing and Alzheimer's model, we found that the WAM population appeared before the DAM, in an ageing dependent manner. Moreover, by using electronic microscopy correlated with light microscopy (CLEM), we found that WAMs are clearing myelin debris and formed clusters of nodules.

Individual contributions: M. Simons and O.G. conceived and supervised the project. S.S., **S.B.-G.**, T.K., M. Schifferer, L.L., N.K., O.G., H.J., F.U., L.C.-C., M.J.R., R.P., G.G., M.B., D.F., and X.X. performed experiments and analyzed the data. **S.B.-G.** and T.K. developed software and curated and visualized the scRNA-seq data. O.G., M.R., and M. Simons analyzed the data or supervised data acquisition. M. Simons and O.G. wrote the manuscript with input from all authors.

In more details, as a co-first author, I established and optimised the single-cell library generation pipeline and the bionformatics data analysis pipeline that were used to generate the fundamental single-cell data in this publication. For the library generation, I contributed to the development of our protocol that includes actinomycin-D to prevent handling artefacts during the library generation. I performed the transcriptomics library generation and analyses to confirm our findings. I guided and assisted the isolation of the microglia via flow cytometry and I processed and analysed the single-cell data and categorised the different states of microglia, realising that one state was

white-matter specific, I identified the WAM ageing signature; thereby providing immunocytochemistry with specific markers. I provided continuous assistance to writing the manuscript.

Neuron

Article

White matter aging drives microglial diversity

Graphical Abstract

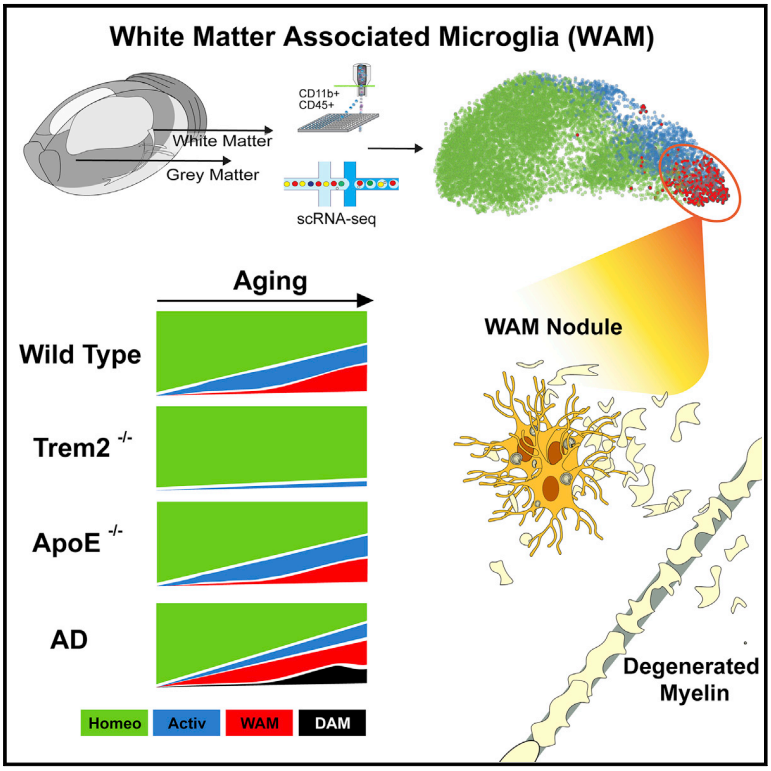

Authors

Shima Safaiyan, Simon Besson-Girard, Tuğberk Kaya, ..., Matthias Brendel, Ozgun Gokce, Mikael Simons

Correspondence

oezguen.goekce@med.uni-muenchen.de (O.G.),
msimons@gwdg.de (M.S.)

In Brief

Safaiyan et al. identify white matter-associated microglia (WAMs), which form in a TREM2-dependent but APOE-independent manner in aging white matter, where they form nodules that are engaged in phagocytosing damaged myelin. Thus, WAMs represents a response required to clear degenerated myelin that accumulates during white matter aging and disease.

Highlights

- scRNA-seq identifies age-dependent white matter-associated microglia (WAMs)
- WAMs form nodules that are engaged in clearing degenerated myelin
- WAM formation depends on TREM2 but not on APOE signaling
- In mouse models of Alzheimer's disease, the WAM response occurs before DAM

Safaiyan et al., 2021, Neuron *109*, 1100–1117
April 7, 2021
https://doi.org/10.1016/j.neuron.2021.01.027

CellPress

CellPress

Neuron

Article

White matter aging drives microglial diversity

Shima Safaiyan,[1,2,9] Simon Besson-Girard,[3,9] Tuğberk Kaya,[1,2,3] Ludovico Cantuti-Castelvetri,[1,2] Lu Liu,[3] Hao Ji,[3] Martina Schifferer,[2] Garyfallia Gouna,[1,2] Fumere Usifo,[3] Nirmal Kannaiyan,[4] Dirk Fitzner,[5] Xianyuan Xiang,[6] Moritz J. Rossner,[4] Matthias Brendel,[7,8] Ozgun Gokce,[3,8,10,*] and Mikael Simons[1,2,8,10,11,*]

[1]Institute of Neuronal Cell Biology, Technical University Munich, 80802 Munich, Germany
[2]German Center for Neurodegenerative Diseases (DZNE), 81377 Munich, Germany
[3]Institute for Stroke and Dementia Research, University Hospital of Munich, LMU Munich, 81377 Munich, Germany
[4]Department of Psychiatry, Ludwig-Maximilians-Universität, 80336 Munich, Germany
[5]Department of Neurology, University of Göttingen, 37075 Göttingen, Germany
[6]Metabolic Biochemistry, Biomedical Center (BMC), Faculty of Medicine, Ludwig-Maximilians-Universität Munich, 81377 Munich, Germany
[7]Department of Nuclear Medicine, University Hospital of Munich, LMU Munich, 81377 Munich, Germany
[8]Munich Cluster of Systems Neurology (SyNergy), 81377 Munich, Germany
[9]These authors contributed equally
[10]Senior author
[11]Lead contact
*Correspondence: oezguen.goekce@med.uni-muenchen.de (O.G.), msimons@gwdg.de (M.S.)
https://doi.org/10.1016/j.neuron.2021.01.027

SUMMARY

Aging results in gray and white matter degeneration, but the specific microglial responses are unknown. Using single-cell RNA sequencing from white and gray matter separately, we identified white matter-associated microglia (WAMs), which share parts of the disease-associated microglia (DAM) gene signature and are characterized by activation of genes implicated in phagocytic activity and lipid metabolism. WAMs depend on triggering receptor expressed on myeloid cells 2 (TREM2) signaling and are aging dependent. In the aged brain, WAMs form independent of apolipoprotein E (APOE), in contrast to mouse models of Alzheimer's disease, in which microglia with the WAM gene signature are generated prematurely and in an APOE-dependent pathway similar to DAMs. Within the white matter, microglia frequently cluster in nodules, where they are engaged in clearing degenerated myelin. Thus, WAMs may represent a potentially protective response required to clear degenerated myelin accumulating during white matter aging and disease.

INTRODUCTION

White matter is composed of mostly myelinated axons that connect neurons from different brain regions into functional circuits. The light appearance of white matter results from the high lipid content of myelin, a multilamellar membrane structure that coats axons and constitutes almost half of the dry weight of white matter (Stadelmann et al., 2019). Long thought to be a passive part of the brain, it is now clear that dynamic, experience-dependent generation of white matter myelin content by oligodendrocytes affects learning and brain function (McKenzie et al., 2014; Mount and Monje, 2017; Pan et al., 2020; Wang et al., 2020; Steadman et al., 2020). In humans, white matter volume reaches its peak at around 40–50 years of age, after which it declines continuously (Sowell et al., 2003). White matter aging is not only associated with tissue shrinkage but also frequently with focal lesions seen upon magnetic resonance imaging (MRI) as hyperintensities related to cognitive impairment and increased risk of stroke and dementia (Prins and Scheltens, 2015). Electron microscopy studies performed in non-human primates have revealed that major pathological alterations that occur during aging are found in white but not gray matter (Peters, 2002), consisting of myelin outfolding, splitting, and accumulation of multilamellar fragments (Peters, 2002; Safaiyan et al., 2016). A better understanding of such age-related white matter pathology and its associated cellular responses is essential because aging is a major risk factor for the most prevalent neurodegenerative diseases. One cell population that responds to aging is microglia, long-lived, self-renewing cells with phagocytic scavenging and immune surveillance functions (Grabert et al., 2016; Füger et al., 2017; Salter and Stevens, 2017; Prinz et al., 2019). Gene expression studies have shown that aged microglia develop a more inflammatory phenotype, particularly in white matter (Poliani et al., 2015; Safaiyan et al., 2016). Age-dependent increase in inflammatory status of microglia is often referred to as primed or sensitized, but the nature of this response is only partially understood (Perry and Holmes, 2014). Several groups have applied single-cell genomics approaches to characterize the shift in microglial states after various pathological insults (Keren-Shaul et al., 2017; Mathys et al., 2017; Friedman et al., 2018; Hammond et al., 2019). This work has established that microglia undergo a relatively stereotypical conversion into disease-associated

microglia (DAM) with a microglia-neurodegenerative (MGnD) or activated response microglia (ARM) phenotype (Keren-Shaul et al., 2017; Krasemann et al., 2017; Sala Frigerio et al., 2019). This conversion is dependent on TREM2 (triggering receptor expressed on myeloid cells 2) activity, which increases phagocytosis and lipid metabolism. DAMs have the potential to restrict pathology by enhancing clearance of misfolded and aggregated proteins that commonly accumulate in neurodegenerative diseases, but to what extent DAMs/MGnD/ARMs are also generated during normal aging is under debate (Keren-Shaul et al., 2017; Friedman et al., 2018; Hammond et al., 2019; Sala Frigerio et al., 2019). Because aging-induced damage to the brain involves degeneration of myelinated nerve fibers, not characterized by protein aggregates but by release of lipid-rich, tightly compacted, and difficult-to-digest myelin debris, we hypothesized that microglial responses should differ between aged gray and white matter. To characterize this microglial response, we combined genetic perturbation, single-cell RNA sequencing (scRNA-seq), immunohistochemistry, and functional assays to comprehensively characterize microglial responses that occur in aged white matter.

RESULTS

TREM2- and age-dependent formation of white-matter associated microglia

To characterize this microglial response, we took advantage of scRNA-seq, a powerful and sensitive technique to reveal transcriptomic cell-to-cell variation of microglia in the normal and diseased brain (Hammond et al., 2019; Keren-Shaul et al., 2017; Krasemann et al., 2017; Masuda et al., 2019; Mathys et al., 2019; Van Hove et al., 2019; Chen et al., 2020). However, transcriptional responses to dissociation have also been shown to alter microglial scRNA-seq analysis (Ayata et al., 2018; Haimon et al., 2018; Hammond et al., 2019; Li et al., 2019). To avoid isolation artifacts, we established an automated dissociation protocol for microglia that inhibits *ex vivo* transcription by addition of actinomycin D (ActD) (Wu et al., 2017). Using scRNA-seq, we tested the effect of ActD addition, which was able to prevent significant induction of four genes (*Jun*, *Lars2, Gm23935*, and *CT010467.1*) and of average expression of immediate-early genes known to respond to brain dissociation (Wu et al., 2017; Figures S1A–S1C; STAR methods). Using this optimized protocol, we dissociated gray matter from the frontal cortex and white matter tracts from the *corpus callosum* as well as the optical tracts and the *medial lemniscus* from wild-type aged mice (18–20 months old; Figure 1A). To compare aging and neurodegeneration effects on microglia, we also isolated microglia from a transgenic Alzheimer's disease (AD) mouse model that expresses five human familial AD gene mutations (5×FAD) (Oakley et al., 2006). Because activation of the DAM gene expression profile depends on TREM2 signaling (Keren-Shaul et al., 2017), we included aged *Trem2* knockout mice (*Trem2*$^{-/-}$) in the analysis. We performed Smart-seq2 (SS2), which has a high transcript capture rate that produces biologically meaningful clusters even for a small number of cells (Picelli et al., 2014; Gokce et al., 2016; Li et al., 2019). After eliminating low-quality SS2 libraries, we included 1,038 microglia from 16 mice. Analysis of sorting data showed that aged wild-type white matter immune cells had significantly increased levels of CD45^{+} and CD11b^{+} labeling compared with gray matter, which was not observed in aged *Trem2*$^{-/-}$ animals (Figures S1D–S1F). Based on known immune cell markers, we identified 847 high-quality SS2 scRNA-seq microglia from aged mice and cells expressing markers for granulocytes, perivascular macrophages, and oligodendrocytes, which were excluded from downstream analyses (Figures S1I and S1J). Next we analyzed the transcriptomes of single cells using unsupervised uniform manifold approximation and projection (UMAP) analysis, a dimension reduction method, which separated aged white matter from aged gray matter microglia (Figure S1K). This white matter microglia-specific cluster was defined by a specific gene signature (STAR methods; Figure S1K; Table S2). Using this white matter microglia gene signature, we distinguished four distinct populations: two white matter-specific clusters, which we called white matter associated microglia (WAMs) and activated microglia, and two additional clusters found in gray and white matter, which we called homeostatic microglia 1 and 2 (Figures 1B–1E; Figure S2A; Table S2). Comparing wild-type with *Trem2*$^{-/-}$ mice revealed that WAMs and activated microglia are TREM2 dependent (Figure 1E; Figure S2A). WAMs are characterized by downregulation of homeostatic genes (set 4 genes; Figure 1C; Figure S3A), such as purinergic receptor (*P2ry12* and *P2ry13*) and checkpoint genes (*Csfr1r*, *Cx3cr1*, *Hexb*, and *Tmem119*) and by upregulation of DAM-associated genes (set 1 genes; Figure 1C; Figure S2A), such as lipid metabolism and phagosome-related genes (*ApoE*, *Cst7*, *Bm2*, *Lyz2*, *Cd63*, and *Clec7a*), cathepsins (*Ctsb*, *Ctss*, and *Ctsz*), and major histocompatibility complex (MHC) class II-related genes (*H2-D1* and *H2-K1*). Activated microglia are marked by upregulation of genes encoding many metabolic genes, mostly ribosomal subunits and mitochondrial genes (set 2 genes), many of which are part of the microglial response to aging (Ximerakis et al., 2019) (set 2 genes; Figures 1C and 1D; Figure S2A). Homeostatic microglia 1 and 2 were detected in white and gray matter and differed from WAMs by higher expression of homeostatic genes such as *Tmem119*, *Csf1r*, *Cx3cr1*, *Hexb*, and *Tmem119* (set 4 genes; Figure 1C; Figure S2A) and lower expression of genes linked to the DAM signature, such as *ApoE*, *Cst7*, *Bm2*, *Lyz2*, *Cd63*, *Clec7a*, *Ctsb*, *Ctss*, *Ctsz*, *H2-D1*, and *H2-K1* (set 1 genes; Figure 1C; Figure S2A).

To validate our results, we performed droplet-based scRNA-seq (Drop-seq) on 24-month-old mice (21,197 high-quality cells from 17 mice used in five Drop-seq runs; Figures 2A and 2B; Figures S2B and S2C; Table S1, tab "Current Study-10X"). We partitioned cells into major cell types (Figure 2B), revealing the white and gray matter cellular landscapes (Figure 2C). The distribution of ciliated and secretary ependymal cells between white and gray matter validated our microdissection because these cells were located on the *corpus callosum* surface. Using the white matter signature genes, we again identified a continuous range of microglia that reproduced the four microglia clusters of the SS2 scRNA-seq dataset (Figure 2D). The gene expression profiles of all four microglia clusters were very similar in both scRNA-seq datasets. None of the 5,991 microglia from the frontal cortex were identified as WAMs, validating allocation of WAMs to aged white matter (Figures 2E–2G). The activated

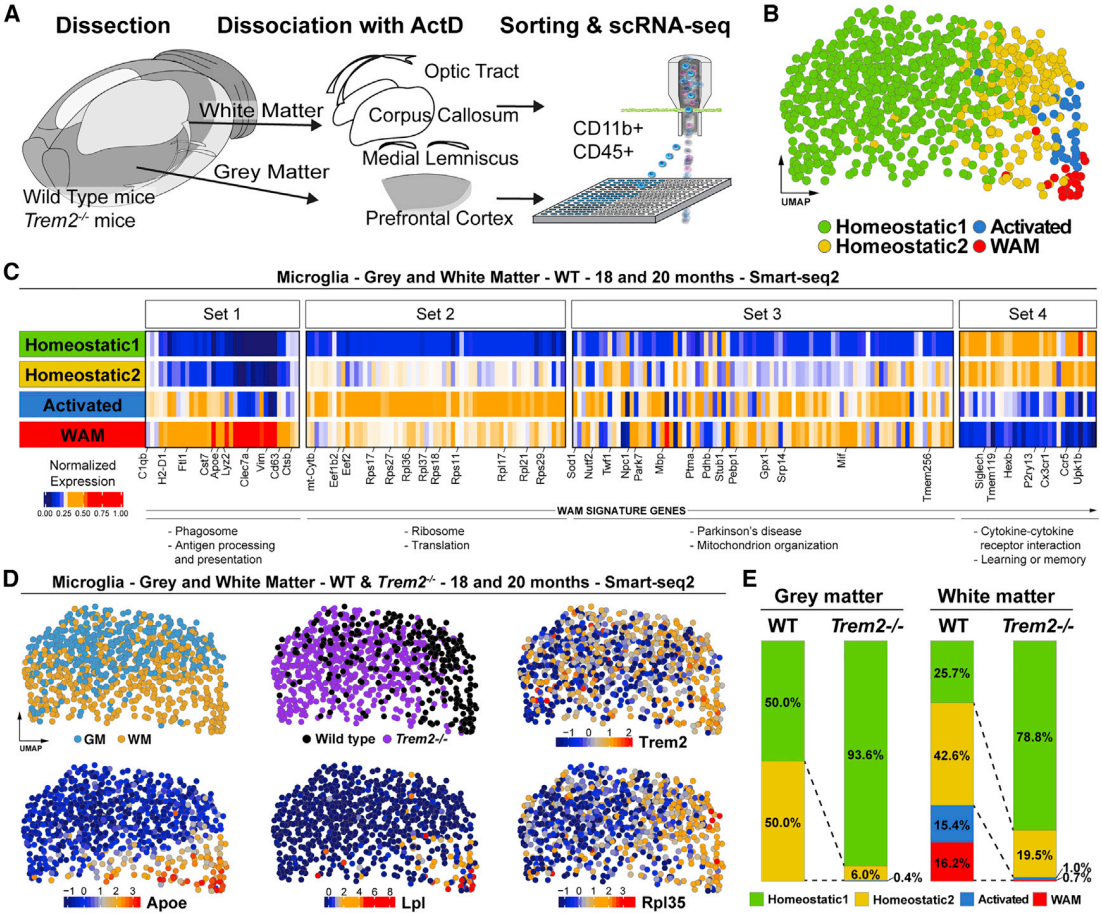

Figure 1. White matter-associated microglia (WAMs) are specific to white matter and exhibit a differential gene expression signature

(A) Experimental design from dissection to cell sorting for the SS2 pipeline (STAR methods).

(B) UMAP of microglia, colored by populations after identification of the white matter activated microglia signature. SS2 dataset, gray matter (GM) and white matter (WM), wild-type (WT), and *Trem2*$^{-/-}$, 18–20 months old (Table S1).

(C) Heatmap of the average expression of differentially expressed genes, comparing the 4 populations of microglia (WAM signature). Values are normalized per gene, showing gene expression across the populations. The gene sets (1–4) were identified by hierarchical clustering of the differentially expressed genes of each population (STAR methods). Gene Ontology analysis pathways are shown below each set of genes. A single-cell version of this heatmap is available in Figure S2A. A list of differentially expressed genes (WAM signature) is shown in Table S2.

(D) UMAP of microglia in WAM signature genes (Table S2). Gene expression is the scaled value.

(E) Bar plot showing the relative distribution of each microglia population in WT GM, *Trem2*$^{-/-}$ GM, WT WM, and *Trem2*$^{-/-}$ WM.

microglia population was enriched in white matter but was also detected in gray matter. The difference in activated microglia distribution in the SS2 and Drop-seq datasets might be due to the different age points analyzed (18–20 versus 24 months) or the higher cell number in the Drop-seq dataset (Figure 2G). Using the Drop-seq dataset, we compared activated microglia with WAMs (Figures 2H and 2I) and identified 428 transcripts that were differentially expressed (Figure 2H). Kyoto Encyclopedia of Genes and Genomes (KEGG) pathway enrichment analysis of the upregulated genes showed that ribosomes were the top enriched pathway in activated microglia. The most enriched pathway in WAMs was hypoxia-inducible factor (HIF-1) signaling, lysosomal, and cholesterol pathways (Figure 2I).

To address whether the WAM signature is aging dependent, we isolated microglia and other myeloid cells from the *corpus callosum* (white matter) and frontal cortex (gray matter) of 4- and 21-month-old wild-type mice using CD11b microbeads and performed bulk RNA-seq analysis. Pathway analysis showed that genes involved in immune cell function were among the most upregulated pathways in aged white matter (Figure S2E). Microglia in aging gray matter did not show these changes in immune cell function but instead exhibited alterations in pathways involved in ion channel activity (Figure S2F). When comparing the genes expressed differentially in aged white matter compared with young white matter or aged gray matter CD11b^{+} cells, 39 transcripts were identified that overlapped with WAM signature genes, such as *Lgals3*, *Spp1*, *Cst7*, *Lpl*, *Clec7a*, *Itgax*, and *ApoE* (Figures S2G and S2H; Table S3), suggesting that WAM marker genes increase with aging in the white matter. Because recent scRNA-seq studies have analyzed microglia during

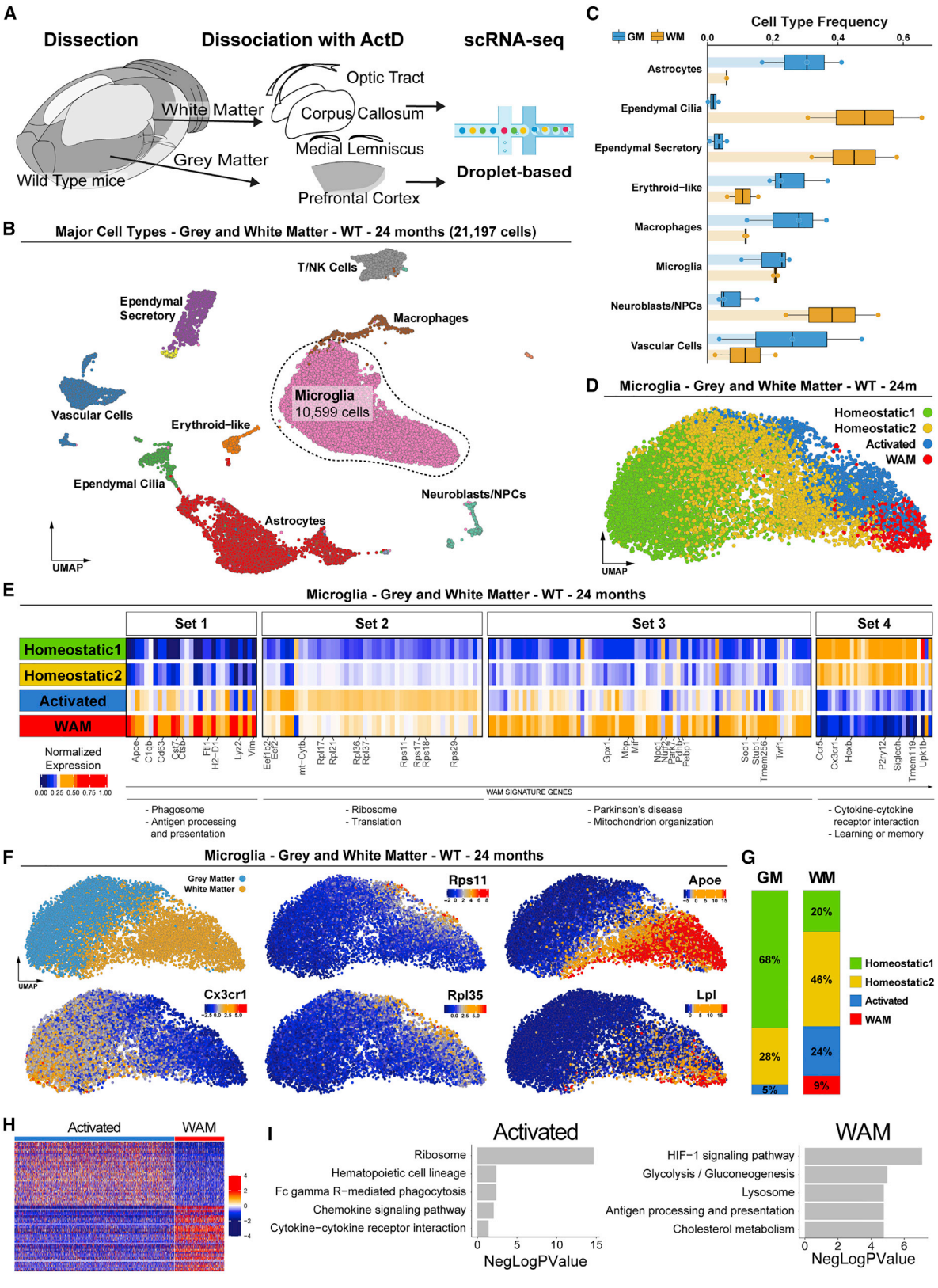

(legend on next page)

normal brain aging without reporting WAMs, we re-analyzed these existing datasets (Hammond et al., 2019; Sala Frigerio et al., 2019). We first analyzed the microglia scRNA-seq by Sala Frigerio et al., 2019, which used cold dissociation to avoid *ex-vivo*-induced transcriptional activity artifacts with the SS2 protocol. We identified microglia with gene expression patterns nearly identical to WAMs (Figure 3A). Already at 3 months of age, microglia with WAM expression patterns could be identified, and the number of these microglia with the WAM gene signature increased with aging (Figure 3B; Figure S3A). Furthermore, when we integrated our dataset with that of Sala Frigerio et al., 2019, we found that the microglial states cluster together (Figure S3B). Similarly, we identified microglia with the WAM gene signature in the Drop-seq dataset from Hammond et al. (2019), which also used cold-dissociated animals to collect cells (Figures 3A–3D; STAR methods). In both datasets, we observed an increase in microglia with the WAM gene signature during aging (Figure 3B). Microglia with the WAM gene signature were characterized by downregulation of homeostatic genes (set 4 genes, *P2ry12*) and upregulation of DAM-associated genes (set 1 genes, *Cd63*). In all three datasets, the activated microglia were marked by upregulation of translation-related gene set 2 (*Rpl37* and *Rpl41*) (Figures 3A, 3C, and 3D). WAMs appear to be present in different datasets with very similar expression profiles.

WAMs cluster in nodules in a TREM2-dependent pathway

To determine the localization of reactive microglia in the brain, we co-stained ionized calsium-binding adaptor 1 (IBA1)$^+$ microglia with activated microglia and WAM markers (Figure S3C) using antibodies against CRYBA4, CLEC7A, AXL, and LGALS3 (Galectin-3) and RNA *in situ* probes against *Itgax* (Figure 4; Figures S4A and S4B). Consistent with the scRNA-seq data, we found that antibodies against the activated microglia marker CRYBA4 (Figure S4B) marked IBA1$^+$ cells in young (2 months old) and old (24 months old) white matter tracts (~15%–20% of IBA1$^+$ cells; Figure S4C). This was in contrast to the WAM markers CLEC7A, AXL, LGALS3 (Galectin-3), and *Itgax*, which labeled IBA1$^+$ cells in old but not young white matter (Figure 4A; Figure S4A). Quantification revealed that ~10%–30% of IBA1$^+$ cells in the *corpus callosum* were positive for the respective WAM markers in 24-month-old mice (20.75% ± 9.67% CLEC7A$^+$IBA1$^+$ cells/area, 14.44% ± 5.05% AXL$^+$IBA1$^+$ cells/area, 31.64% ± 11.68% LGALS3$^+$IBA1$^+$ cells/area, and 9.64% ± 6.46% *Itgax*$^+$IBA1$^+$ cells/area) (Figure 4A). Notably, and in agreement with our RNA-seq data, we found that these cells were almost absent from cortical areas of the aged brain (Figure 4B). Analysis of the localization of double-positive microglia in the white matter showed that they were not distributed evenly but often found in clusters consisting of 3–5 cells with large cell bodies and thick processes (Figure 4C; Figure S4E). Microglia clusters were only found in white matter, where they increased with age (Figure 4C). Such clusters of activated microglia have previously been called microglial "nodules" and are found with a number of different brain diseases, including brain trauma, multiple sclerosis, and viral encephalitis (Rock et al., 2004). To determine the ultrastructure of these nodules, we performed correlated light and electron microscopy using an antibody against IBA1. We found myelin debris in microglia nodules and degenerated myelin in the direct vicinity of the cells, suggesting that microglia nodules are engaged in myelin phagocytosis (Figure 4D; Figure S4F). We performed immunohistochemistry using antibodies against myelin basic protein (MBP), the main structural protein of myelin, to quantify the amount of microglia containing MBP, and found that almost half of the IBA1$^+$ cells with internalized MBP$^+$ particles localized to nodules (Figure 4E; Figure S4G). Microglia in nodules were positive for WAM markers, and we did not detect any activated microglia defined as CRYBA4$^+$/Galectin-3$^-$/IBA1$^+$ cells in nodules (Figure S4D). These data suggest that WAMs actively digest myelin debris in aging white matter, possibly deriving from degenerated myelin sheaths that accumulate over time during aging. If this is the case, then triggering myelin degeneration should induce premature clustering of microglia into nodules. To test this prediction, we used a mouse model for Pelizaeus-Merzbacher disease (PMD mice), a leukodystrophy with extra copies of the proteolipid protein gene (Readhead et al., 1994). These mice initially develop relatively normal myelin, but within weeks, myelin sheaths are broken down gradually (Readhead et al., 1994). We co-stained IBA1$^+$ microglia using antibodies against CLEC7A, AXL, and LGALS3 together with antibodies against MBP to detect myelin particles in microglia. Strikingly, at 2 months of age, when the demyelinating phenotype of these mice starts, microglia nodules appeared in the *corpus callosum* (Figure S5A). These IBA1$^+$ cells in nodules contained MBP$^+$ intracellular particles and increased in number with time (Figures S5B–S5E). Such nodules were not observed in cortical areas. Quantification revealed that ~9%–40% of IBA1$^+$ cells in the *corpus callosum* were already positive for CLEC7A, AXL, or LGALS3 in 2-month-old PMD mice. Similar results were obtained in 7- and 10-month-old PMD mice (Figures S5F–S5H).

These data provide evidence that WAMs in nodules are engaged in clearing degenerated myelin in aging or diseased

Figure 2. Drop-seq validates that WAMs are specific to WM

(A) Experimental design from dissection to cell loading for the Drop-seq pipeline (STAR methods).
(B) UMAP of 21,197 single-cell transcriptomes, colored by major cell type clusters.
(C) GM and WM proportions in major cell type clusters.
(D) UMAP of microglia, colored by populations after identification of the WM microglia signature. Drop-seq dataset, GM and WM, 24 months old (Table S1).
(E) Heatmap of the average expression of differentially expressed genes, comparing the 4 populations of microglia (WAM signature). Values are normalized per gene, showing gene expression across the populations. Gene Ontology analysis pathways are shown below each set of genes.
(F) UMAP colored by tissue annotation and expression of selected marker genes. Gene expression is the scaled value.
(G) Bar plot showing the relative distribution of each microglia population in WT GM and WT WM.
(H) Activated and WAM populations were analyzed separately. Shown is a heatmap with the top 40 differentially expressed genes for activated and WAM populations. Each row represents a gene and each column a single cell.
(I) KEGG pathway enrichment for activated and WAM upregulated differential expression analysis (DEGs).

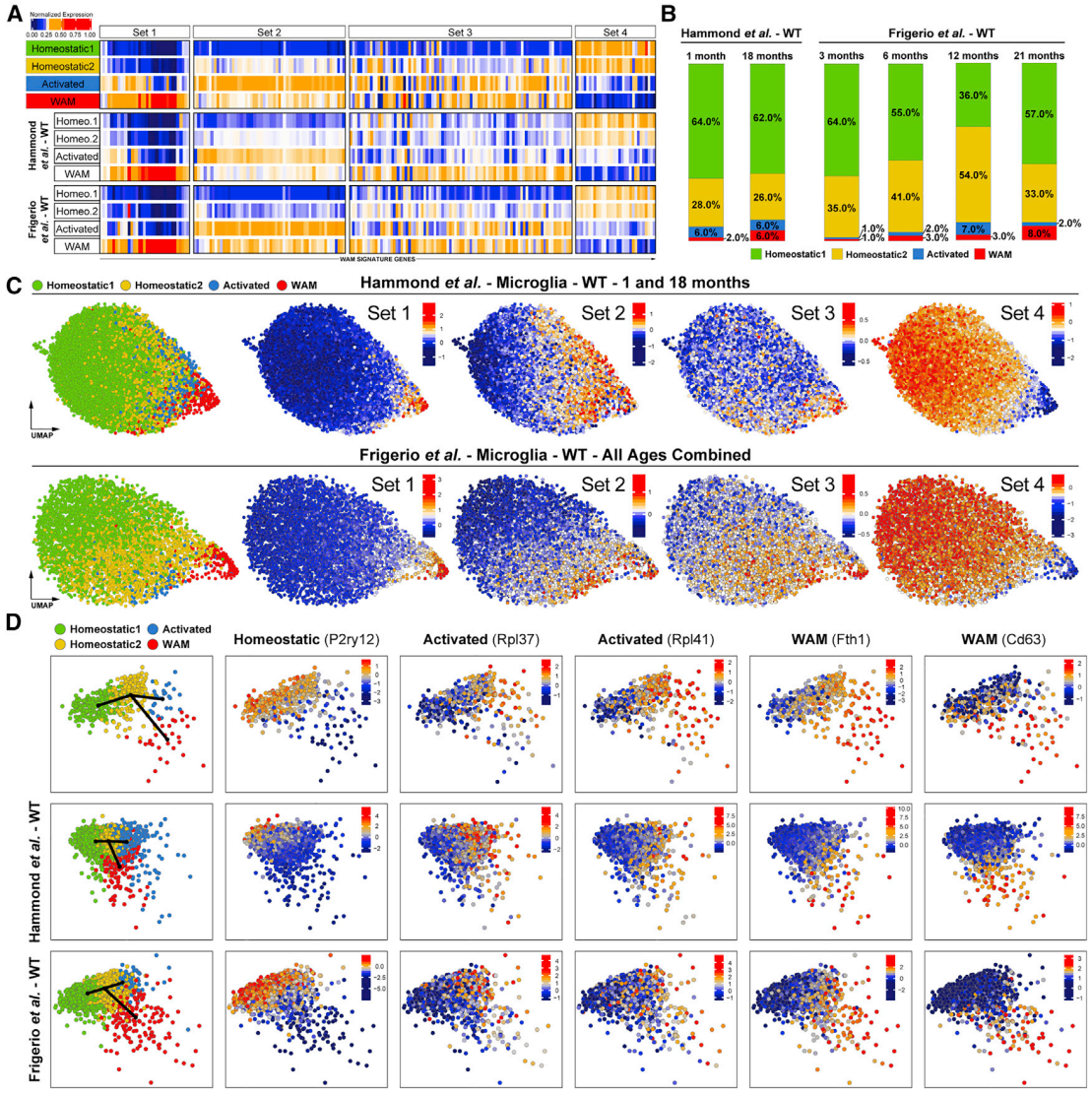

Figure 3. The WAM signature is consistent across multiple datasets

(A) Heatmaps of the average expression of WAM signature gene sets (sets 1–4) for each population, aligned with the four populations identified in data from Hammond et al. (2019) and Sala Frigerio et al. (2019). Values are normalized per gene. The first heatmap is identical to Figure 1C and is reported here for easier comparison. All age groups are pooled within the respective datasets (Table S1).

(B) Cell population ratios by age groups. Shown are data from 1- to 18-month-old WT mice and from 3-, 6-, 12-, and 21-month-old WT mice data from Hammond et al. (2019) and Sala Frigerio et al. (2019), respectively.

(C) UMAPs showing the 4 identified populations and the average scaled expression of each gene set per cell. The first row shows data from Hammond et al. (2019), young and old mouse data combined, 9,558 microglia. The second row shows data from Sala Frigerio et al. (2019), all age groups combined, 5,093 microglia (Table S1).

(D) Principal-component analyses (PCAs) based on the WAM signature genes and overlay with Slingshot plots colored by microglia populations (left), the homeostatic marker *P2ry12*, the activated markers *Rpl37* and *Rpl41* (center), and the WAM markers *Fth1* and *Cd63* (right). Rows 1–3 correspond to data from this study, Hammond et al. (2019), and Sala Frigerio et al. (2019), respectively. Gene expression is the scaled value.

white matter. Because our scRNA-seq data indicated a function of TREM2 in this process, we used antibodies and *in situ* probes to visualize microglia in *Trem2*$^{-/-}$ mice. Consistent with our scRNA-seq data, we failed to detect CLEC7A, AXL, *Itgax*, or LGALS3 (Galectin-3) in the *corpus callosum* of aged *Trem2*$^{-/-}$ mice (Figure 5A). Next we determined the number of homeostatic microglia using antibodies against TMEM119 and P2RY12 and found that the number of TMEM119^{+}IBA1^{+} or P2RY12^{+}IBA1^{+} decreased with age in the white matter of wild-type mice (Figures 5B–5D; Figure S4H). This was in contrast to *Trem2*$^{-/-}$ mice, in which the numbers remained unchanged in 6-, 12-, and 18-month-old mice (Figures 5B–5D; Figure S4H). In addition, and

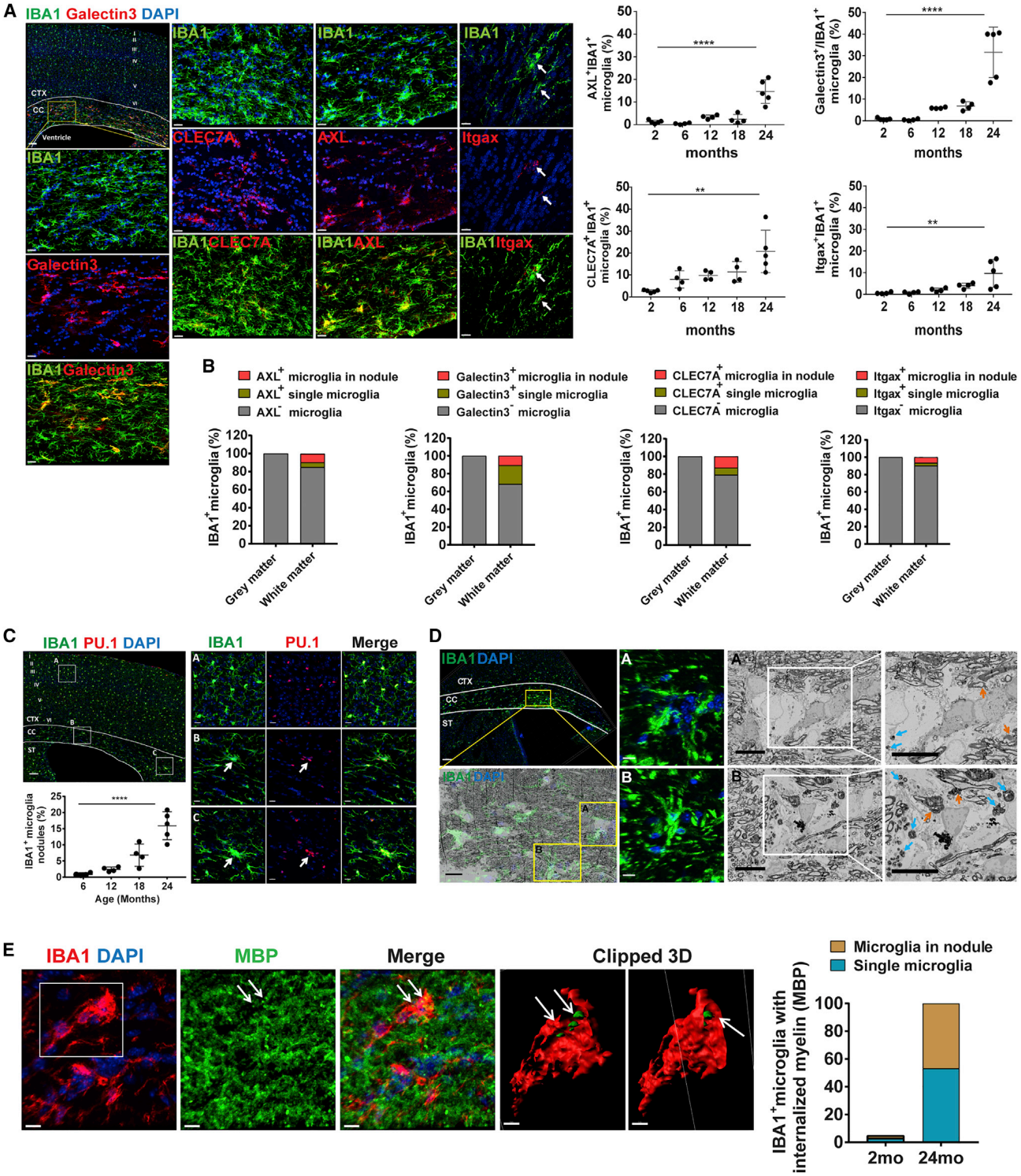

Figure 4. WAM are localized in microglia nodules and contain myelin fragments

(A) Confocal images of CLEC7A, AXL, Galectin-3, and *Itgax* (red) co-localization with IBA1^{+} microglia (green) in 24-month-old mice using immunohistochemistry and RNAScope *in situ* hybridization. Scale bars, 100 μm (overview) and 20 μm (magnification). Also shown is quantification of CLEC7A, AXL, Galectin-3, and *Itgax* expression in 2-, 6-, 12-, 18-, and 24-month-old mice in WM (*corpus callosum*; n = 4–5 mice per group, mean ± SD, one-way ANOVA followed by Bonferroni's post hoc test; AXL, ****p < 0.0001; Galectin-3, ****p < 0.0001; CLEC7A, **p = 0.0013; *Itgax*, **p = 0.0039).

(legend continued on next page)

consistent with previous results (Poliani et al., 2015; Kleinberger et al., 2017), we found that the increase in the number of microglia that occurs during normal aging in wild-type white matter was abolished in *Trem2*$^{-/-}$ mice (Figure S4I). Although nodules increased during aging in white matter of wild-type mice, they were almost undetectable in *Trem2*$^{-/-}$ mice at all time points analyzed (Figure 5E). We also examined microglia in the cortex of *Trem2*$^{-/-}$ and wild-type mice but were unable to detect changes in cell density (Figure S4I) or in the proportion of homeostatic IBA1^{+} cells (Figure 5B–5D; Figure S4H), further suggesting that age-related and DAM-associated changes are mainly confined to the white matter of the brain.

WAMs are engaged in clearing myelin debris

Because the WAM response and generation of nodules is abolished in *Trem2*$^{-/-}$ mice, this mouse model provides a means to investigate the biological function of WAMs. We used electron microscopy to visualize possible differences in the ultrastructure of aged white matter in wild-type and *Trem2*$^{-/-}$ mice. We found enhanced accumulation of myelin whorls (not associated with axons) in the *corpus callosum* of aged *Trem2*$^{-/-}$ compared with wild-type control mice (Figure 5F). In addition, an increased number of cells with electron-dense intracellular inclusions were detected in *Trem2*$^{-/-}$ mice, and, using correlated light-electron microscopy, we found that these cells were microglia (Figure 5G). With light microscopy, MBP^{+}, proteolipid protein (PLP)$^{+}$, and FluoroMyelin^{+} intracellular particles were noticed in microglia of aged *Trem2*$^{-/-}$ in white matter to the same extent as in wild-type mice (Figures S4J–S4L). Furthermore, using light microscopy, microglia with irregular processes were detected, as described previously in the context of human brain aging and particularly in neurodegenerative human diseases (Streit et al., 2004). By double immunostaining, using antibodies against IBA1 and CD68 to visualize microglia process morphology (Tischer et al., 2016), we found a dramatic increase in the number of microglia with irregular processes in the *corpus callosum* of 18-month-old *Trem2*$^{-/-}$ compared with wild-type mice. Strikingly, microglia with irregular processes appeared to be restricted to white matter regions; microglia were of ramified morphology in cortical areas (Figure 5H). Thus, TREM2-dependent WAM activity may be a protective response against damaged myelin, possibly to enhance its uptake and breakdown during white matter aging.

To directly assess whether TREM2 is required for uptake and/or breakdown of myelin debris, we performed *in vitro* experiments with cultured primary microglia. CD11b^{+} cells were prepared from wild-type and *Trem2*$^{-/-}$ mice by magnetic-activated cell sorting (MACS), and myelin debris binding, uptake, and degradation were examined. First, we explored the interaction of myelin debris with the cell surface by performing cell surface binding assays at 4°C, which revealed that similar amounts of myelin debris attached to the surface of wild-type and *Trem2*$^{-/-}$ microglia (Figure 6A). In addition, phagocytic uptake of myelin debris occurred to the same extent in wild-type and *Trem2*$^{-/-}$ microglia (Figure 6B). However, differences were detected when cells were chased for 24 h and immunostained for PLP to determine degradation of the ingested myelin (Figure 6B). These experiments demonstrated that myelin debris degradation occurred less efficiently in *Trem2*$^{-/-}$ microglia compared with the wild type, similar to what occurs when microglia are treated with inhibitors of lysosomal function (leupeptin or bafilomycin A; Figure S6A). We used qRT-PCR to examine whether the impaired degradation was due to an inability to induce expression of lysosomal enzymes and found that expression of *cathepsinL*, *beta-galactosidase1*, and *N-acetylglucosamine-6-sulfatase*, but not *hexoaminidase*, were upregulated upon myelin debris uptake in wild-type but not *Trem2*$^{-/-}$ microglia (Figure 6C). Failure of *Trem2*$^{-/-}$ microglia to upregulate Cathepsin L upon myelin debris treatment was confirmed at the protein level by western blotting (Figure 6D). To determine whether myelin debris degradation was also impaired *in vivo* in *Trem2*$^{-/-}$ mice, we employed a toxin-induced model in which a single injection of lysolecithin was injected into the *corpus callosum* to induce a focal demyelinating lesion in the white matter. Removal of damaged myelin debris occurs mainly by microglia because only relatively few monocyte-derived macrophages enter lesions from the periphery (Lloyd et al., 2019; Plemel et al., 2020). We used fluorescent myelin staining (FluoroMyelin) to determine the amount of myelin debris in LAMP1^{+} degradative compartments in IBA1^{+} cells and found that clearance of internalized myelin debris was delayed in *Trem2*$^{-/-}$ mice (Figure 6E).

Next we established a cell culture-based uptake assay to systematically explore the requirements for myelin debris phagocytosis. We used HeLa cells for this assay because only small amounts of myelin debris are taken up by these cells. This allowed us to transiently express a number of different phagocytic

(B) Bar plots showing the fraction of IBA1^{+} microglia found as single cells or in nodules co-localizing with Galectin-3, CLEC7A, AXL, and *Itgax* in WM (*corpus callosum*) and GM (cortical layers I–V) of 24-month-old WT mice (n = 5 mice per group, each fraction represents the mean value of 5 mice).
(C) Confocal image of IBA1^{+} microglia nodules (green) co-labeled with PU.1 (red) in the *corpus callosum* and cortex of 24-month-old WT mice. Scale bars, 50 μm (overview) and 15 μm (magnification). Also shown is quantification of the number of microglia nodules in 6-, 12-, 18-, and 24-month-old WT male mice (n = 4–5 mice per group, mean ± SD, one-way ANOVA, ****p < 0.0001).
(D) Correlative light and electron microscopy of microglia in the *corpus callosum*. Top left: confocal image of a whole section as a guide map for correlation. Bottom left: scanning electron microscopy (SEM) serial section (100 × 100 × 100 nm) overlaid with a confocal image (transparent, IBA1 in green, and DAPI in blue). Two microglia nodules are relocated on this SEM serial section (yellow boxes, images A and B). Images A and B: confocal and SEM images of microglia nodules. Right column: higher-resolution images (20 × 20 × 100 nm) showing degenerated myelin around microglia nodules (orange arrows) and intracellular myelin fragments (blue arrows). Scale bars, 100 μm (overview, immunohistochemistry [IHC]), 100 μm (correlative light and electron microscopy [CLEM] overlay), and 10 μm (high-magnification IHC and SEM).
(E) Confocal image of co-localization of MBP (green) with IBA1^{+} microglia (red) in nodules in the *corpus callosum* of a 24-month-old WT mouse. Clipped 3D images show MBP^{+} myelin particles (green) in a microglia nodule from different angles. Scale bars, 10 μm. The bar plot shows the fraction of IBA1^{+} single cells and IBA1^{+} cells in nodules with internalized myelin fragments in 2- and 24-month-old WT male mice (n = 5 mice per group, each fraction represents the mean value of 5 mice, 2 brain sections were analyzed per mouse).

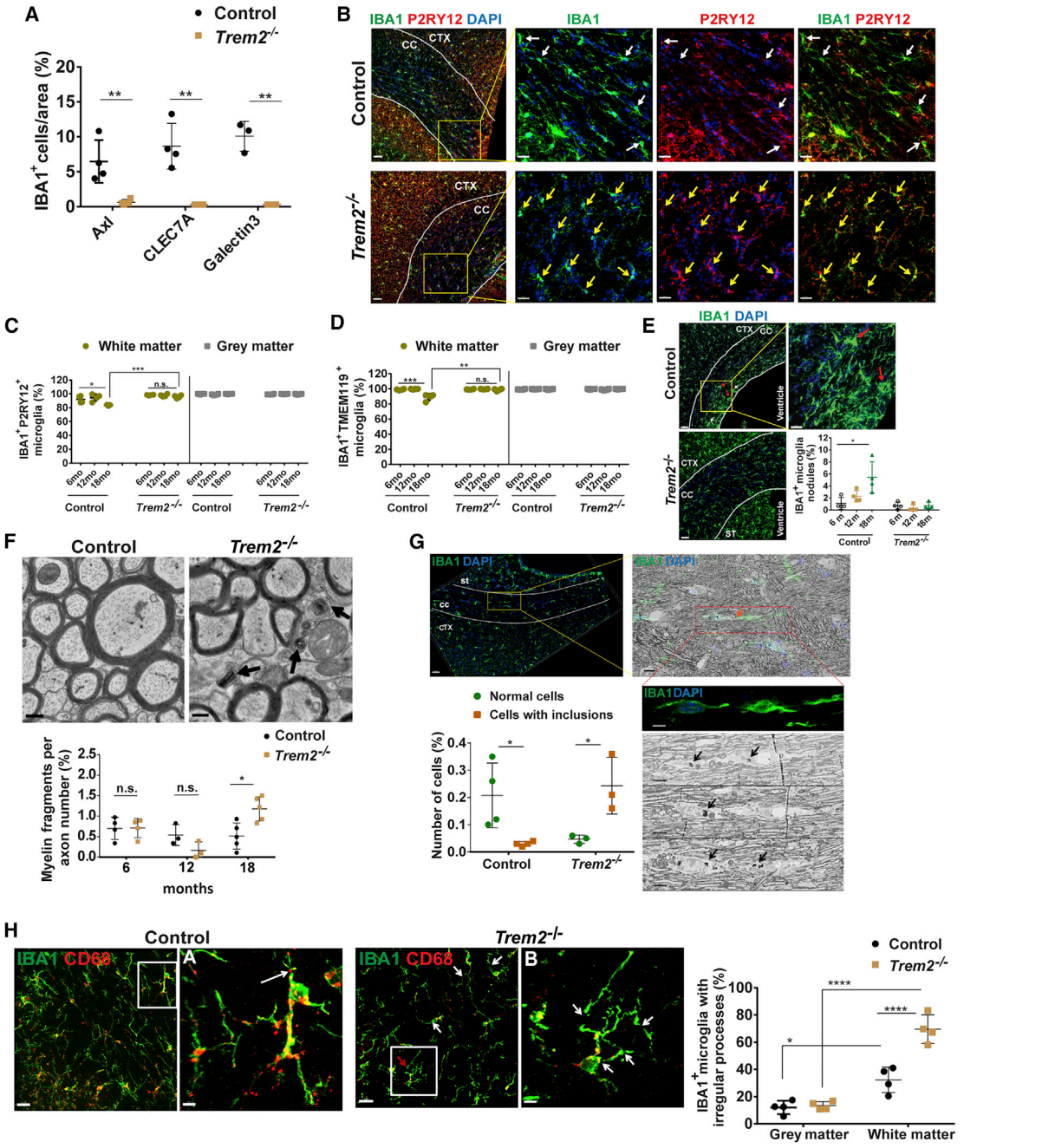

Figure 5. TREM2 is required for WAM states and myelin debris clearance

(A) Quantification of IBA1$^+$ cells also positive for AXL, CLEC7A, and Galectin-3 in the *corpus callosum* of 18-month-old *Trem2*$^{-/-}$ and control mice (n = 4 mice per group, mean ± SD; AXL, **p = 0.009; CLEC7A, **p = 0.0022; Galectin-3, **p = 0.0013; Student's two-tailed t test).

(B) Confocal images showing expression of P2RY12 (red) in IBA1 (green) in 18-month-old *Trem2*$^{-/-}$ and age-matched control mice. The white arrows point to P2RY12$^-$ microglia, and the yellow arrows point to P2RY12$^+$ microglia. Scale bars, 50 μm (overview) and 20 μm (magnification).

(C) Quantification of IBA1$^+$ microglia expressing P2RY12 in WM and GM in 6-, 12-, and 18-month-old *Trem2*$^{-/-}$ and age-matched control mice (n = 4 mice per group, mean ± SD, one-way ANOVA; control, WM, *p = 0.0299; *Trem2*$^{-/-}$, WM, p = 0.1491; 18 months: control versus *Trem2*$^{-/-}$, ***p = 0.0003; Student's two-tailed t test).

(D) Quantification of IBA1$^+$ microglia expressing TMEM119 in WM and GM in 6-, 12-, and 18-month-old *Trem2*$^{-/-}$ and control mice (n = 4 mice, mean ± SD, one way ANOVA; control, WM, ***p = 0.0002; *Trem2*$^{-/-}$, WM, p = 0.1149; 18 months, control versus *Trem2*$^{-/-}$, **p = 0.0058; Student's two-tailed t test).

(E) Confocal image showing abundant microglia nodules in the *corpus callosum* of 18-month-old control compared with age-matched *Trem2*$^{-/-}$ mice. Scale bars, 50 μm (overview) and 20 μm (magnification). Also shown is quantification of the number of microglia nodules in 6-, 12-, and 18-month-old *Trem2*$^{-/-}$ and control male mice (n = 4 mice per group, mean ± SD, one-way ANOVA, *p = 0.0161).

(legend continued on next page)

receptors and to determine their role in mediating myelin debris uptake (Figures S6B and S6C). First we confirmed that expression of TREM2 together with TYROBP (TYRO protein tyrosine kinase-binding protein) induced phagocytosis of myelin debris in HeLa cells (Figure S6D). However, this assay also revealed that a number of different phagocytic receptors were able to mediate myelin debris phagocytosis (Figures S6D–S6F). Notably, all receptors known to depend on direct phosphatidylserine binding or indirect binding using bridging molecules promoted myelin debris uptake. Some of the receptors, such as *Axl*, are part of the WAM response, whereas others, such as *Mertk*, are highly expressed in homeostatic microglia. To confirm that phosphatidylserine is required for myelin debris uptake, we masked phosphatidylserine binding sites by pre-incubating myelin debris with Annexin V, which markedly reduced myelin debris phagocytosis in primary cultures of microglia (Figures S6G and S6H). Thus, binding of myelin debris to multiple receptors that are also expressed in homeostatic microglia suggests that WAMs have an essential function in myelin debris degradation rather than in phagocytotic uptake.

Microglia with WAM and DAM gene signatures co-exist and are generated in an APOE-dependent pathway in models of AD

Next, we explored whether a WAM-like population can be found in mouse models of AD, in which DAMs have been described previously (Keren-Shaul et al., 2017; Krasemann et al., 2017). We generated scRNA-seq data with our optimized protocol from the 6-month-old 5×FAD mouse model of AD. We identified DAM clusters as reported by Keren-Shaul et al. (2017) but also microglia with the WAM gene signature (Figures 7A and 7B). We repeated the same clustering approach on a larger microglial scRNA-seq dataset from Sala Frigerio et al. (2019), which used two mouse models of AD, an *App* knockin mouse model ($App^{NL\text{-}G\text{-}F}$) Masuda et al., 2016; Sasaguri et al., 2017), and transgenic APP/PS1 mice (Borchelt et al., 1997) in combination with an $Apoe^{-/-}$ strain (APP/PS1-$Apoe^{-/-}$) (Sala Frigerio et al., 2019). Our analysis of microglia from AD models distinguishes two microglial subtypes in addition to the four we identified in aged mice. These two additional subtypes match the expression profiles of DAM1 and DAM2 microglia reported previously by Keren-Shaul et al. (2017). In AD models, microglia with the WAM gene expression profile appear very early but with nearly identical signatures compared with the normal aging-induced profiles. DAM1 and DAM2 showed strong gradual upregulation of sets 1–3 and downregulation of the homeostatic genes in set 4 (Figures 1C, 2E, and 7B). Next, we visualized regulation of the DAM program in our aged microglia dataset by plotting the top 500 genes altered in DAMs (Keren-Shaul et al., 2017). Interestingly, we observed that activated microglia and WAMs upregulated distinct parts of the DAM signature (Figure S7A). WAMs appear to represent a microglial state displaying partial activation of the DAM gene signature, suggesting that the DAM program consists of multiple transcriptional modules. WAM and DAM states are likely to be continuous cell identities that can blend with each other. In aging, microglia activation appears to be shifted toward the WAM state, whereas in AD, the shift is toward DAMs.

Thus, in models of AD, microglia with WAM and DAM gene signatures co-exist, raising the question of when and in which temporal sequence they form. In 3-month-old $App^{NL\text{-}G\text{-}F}$ mice, we did not detect DAM2, whereas microglia with the WAM gene signature were present (Figures 7C and 7D). The proportion of cells in DAM and WAM clusters increased with age until 12 months, and then DAMs showed a decrease between 12–21 months.

How do WAM differ from DAM states? To address this question, we took advantage of one main characteristic of WAMs: their involvement in myelin debris clearance in white matter. Although it is well established that activated microglia are distributed throughout the brain and cluster around amyloid plaques (Ulrich et al., 2017), it is not clear whether microglia nodules containing myelin debris are formed. We used immunohistochemistry to determine whether microglia form nodules in white matter of mouse models of AD. We co-stained 6-month-old $App^{NL\text{-}G\text{-}F}$ mice with antibodies against IBA1, MBP, and amyloid and detected nodules with $IBA1^+$ cells containing MBP^+ intracellular particles in the *corpus callosum* that were not associated with amyloid plaques (Figure S7B). Similar findings were obtained in 6-month-old 5×FAD mice, in which nodules containing $IBA1^+$ cells with MBP^+ intracellular particles were detected in the *corpus callosum* (Figures S7C and S7D). A large fraction of $IBA1^+$ cells was also positive for CLEC7A and LGALS3 (Figures S7E and S7F). In 2-month-old 5×FAD mice, only a relatively small number of microglia nodules were detected (Figures S7E and S7F). When $App^{NL\text{-}G\text{-}F}$ mice were crossed with $Trem2^{-/-}$

(F) Representative transmission electron microscopy (TEM) image of the *corpus callosum* in 18-month-old $Trem2^{-/-}$ and control mice, showing myelinated axons and myelin fragments (arrows). Scale bar, 0.2 μm. Also shown is quantification of myelin fragments in 6-, 12-, and 18-month-old $Trem2^{-/-}$ compared with control mice (n = 3–5 mice per group, mean ± SD, two-way ANOVA followed by Bonferroni's post hoc test; 6 months old, $p > 0.9999$; 12 months old, $p > 0.9999$; 18 months old, *$p = 0.0186$).

(G) CLEM of an 18-month-old $Trem2^{-/-}$ *corpus callosum* region. Top left: confocal image as a guide for correlation. Top right: overlaid confocal image (transparent, IBA1 in green, DAPI in blue) onto the SEM serial section and relocation of an $IBA1^+$ cell on the SEM section (red box). Bottom right: confocal and SEM images of an $IBA1^+$ cell. 3 images of SEM serial sections (10 × 10 × 100 nm) reveal intracellular electron-dense inclusions (black arrows). Scale bars, 50 μm (overview, IHC), 20 μm (CLEM overlay), and 10 μm (high-magnification SEM). Also shown is quantification of the number of cells with electron-dense inclusions (n = 3–4 per group, mean ± SD; control, *$p = 0.0245$; $Trem2^{-/-}$; *$p = 0.0371$; Student's two-tailed t test).

(H) Confocal image of microglia co-labeled with IBA1 (green) and CD68 (red), showing microglia with irregular processes in $Trem2^{-/-}$ and microglia in control mice (18 months old). Normal processes are defined by a CD68-positive connection between two IBA1-positive structures (white arrow in image A), whereas fragmented processes have no CD68-positive connection (white arrows in image B). Scale bars, 20 μm (overview) and 5 μm (magnification). Also shown is quantification of the number of microglia with irregular processes in the *corpus callosum* and cortex (layers I–IV) of 18-month-old $Trem2^{-/-}$ and control male mice (n = 4 mice per group, mean ± SD, two-way ANOVA followed by Bonferroni's post hoc test; GM versus WM: control, *$p = 0.0156$; $Trem2^{-/-}$, ****$p < 0.0001$; WM: control versus $Trem2^{-/-}$, ****$p < 0.0001$).

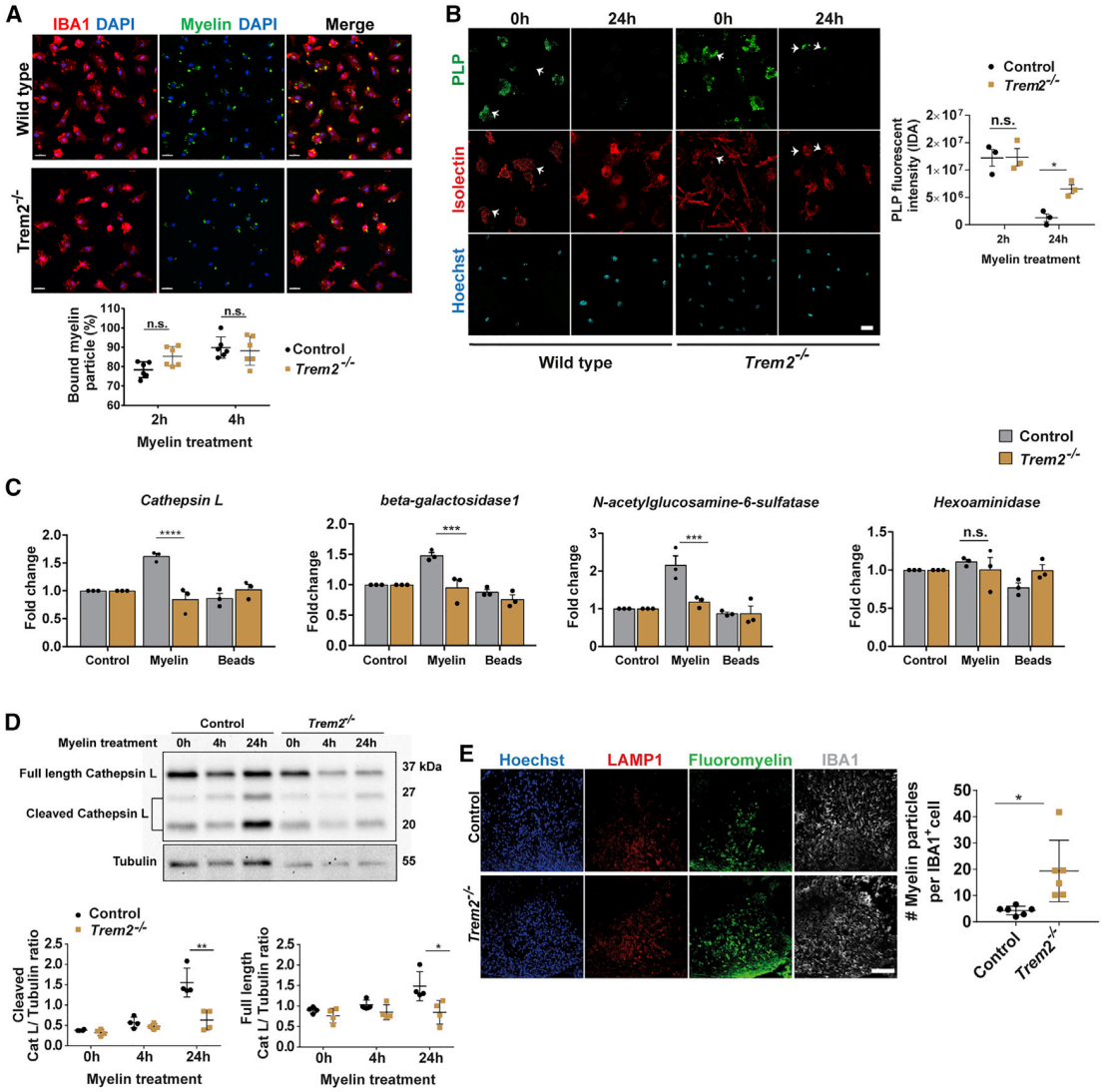

Figure 6. TREM2 is required for lysosomal degradation of internalized myelin debris in microglia

(A) Immunocytochemistry showing PKH67-labeled myelin particles (green) bound to *Trem2*$^{-/-}$ and WT primary microglia (red) in a cell surface binding assay. Scale bar, 20 μm. Also shown is quantification of the number of primary microglia with attached myelin particles 2 and 4 h after myelin treatment (n = 3 independent experiment, mean ± SD; each dot shows the percentage of microglia bound to myelin particles in an area of 0.1 mm^2; two-way ANOVA followed by Bonferroni's post hoc test; control versus *Trem2*$^{-/-}$: 2 h, p = 0.2828; 4 h, p > 0.9999).

(B) Immunocytochemistry showing uptake of PLP-labeled myelin particles (green) by isolectin-labeled microglia (red) isolated from *Trem2*$^{-/-}$ and WT mice. Scale bar, 25 μm. Also shown is quantification of the amount of myelin within microglia cells as measured by the average PLP fluorescence intensity per cell (n = 3 independent experiment, mean ± SD, two-way ANOVA followed by Sidak's post hoc test; control versus *Trem2*$^{-/-}$: 2 h, p = 0.9970; 24 h, *p = 0.0322).

(C) Quantification of expression of the lysosomal enzymes *cathepsinL*, *beta-galactosidase1*, *N-acetylglucosamine-6-sulfatase*, and *hexoaminidase* in *Trem2*$^{-/-}$ and WT microglia treated with myelin or beads (as control) compared with *Trem2*$^{-/-}$ and WT untreated cells. Data are expressed as fold change compared with untreated cells 24 h after myelin debris treatment (two-way ANOVA followed by Sidak's post hoc test; *cathepsinL*, ****p < 0.0001; *beta-galactosidase*, ***p < 0.0004; *acetylglucosamine-6-sulfatase*, ***p = 0.0007; *hexoaminidase*, p = 0.7427).

(D) Western blot analysis of Cathepsin L levels in control and *Trem2*$^{-/-}$ microglia culture lysates 4 and 24 h after myelin treatment. Also shown is quantification of the expression level of full-length and cleaved Cathepsin L compared with tubulin under each condition (mean ± SD, error bar represents 4 independent experiments, Student's two-tailed t test; cleaved CTSL (CatL), **p = 0.0053; full-length CatL, *p = 0.0312).

(E) Confocal images of demyelinating lesions (lysolecithin model) showing myelin debris accumulation (FluoroMyelin in green) in lysosomes (LAMP1 in red) of 3-month-old *Trem2*$^{-/-}$ and control microglia. Scale bar, 100 μm. Also shown is quantification of the number of myelin particles in *Trem2*$^{-/-}$ and control microglia in demyelinating lesions (n = 6 lesion taken from 3 animals per group, mean ± SD, *p = 0.0108, Student's two-tailed t test).

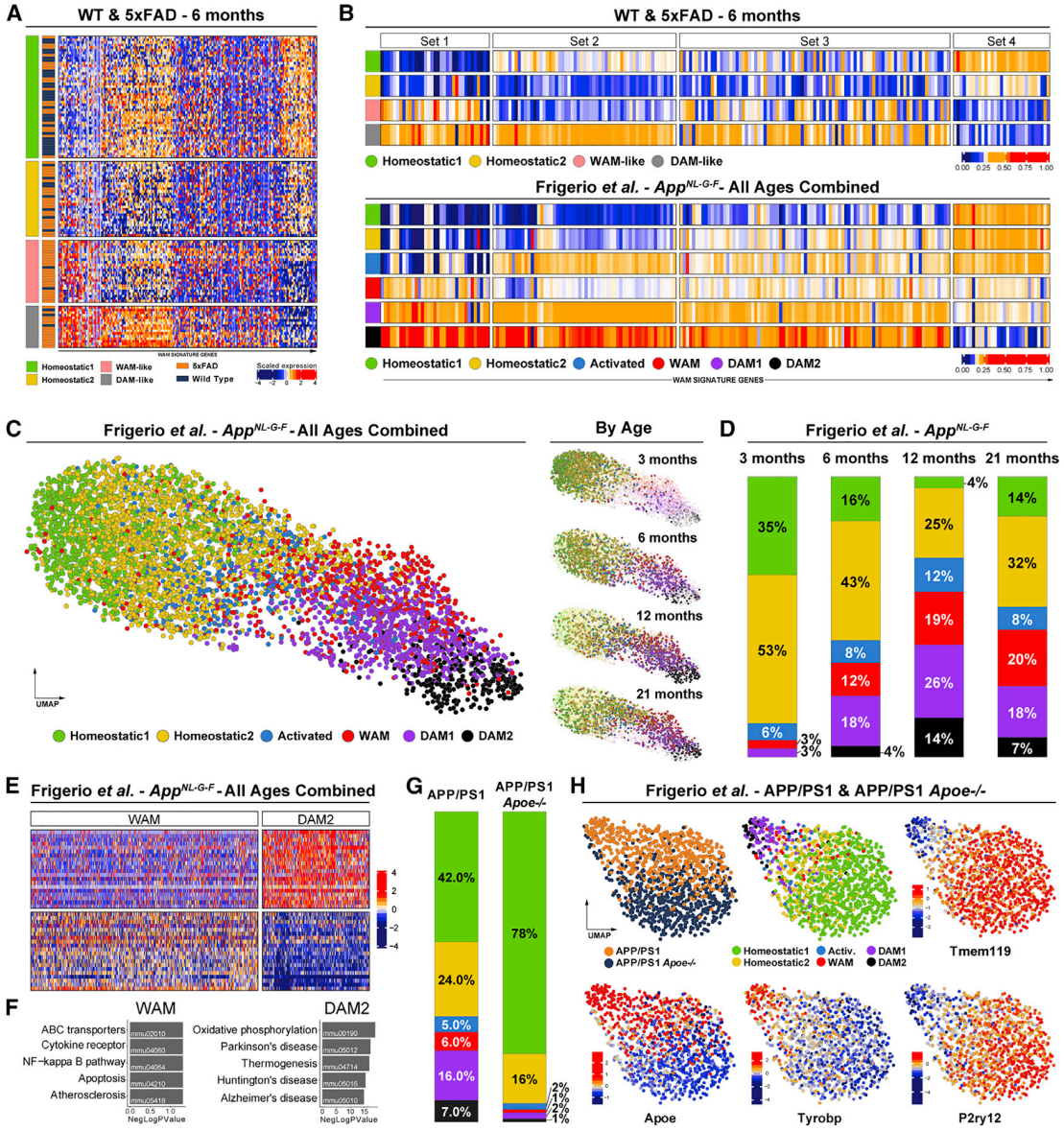

Figure 7. Microglia with a WAM-like signature co-exist with DAMs in AD models

(A) Heatmap of microglia from 5×FAD and wild-type mice, 6 months old. Each row represents a single cell and each column a gene. The bars on the left correspond to the color annotation for population and genotype.

(B) Heatmaps of the average expression of WAM signature gene sets (set 1–4) for each population, along with the six populations of the Sala Frigerio et al., 2019 dataset. Values are normalized per gene.

(C) UMAPs showing the populations identified by the Sala Frigerio et al., 2019 $App^{NL\text{-}G\text{-}F}$ data. Each age group is emphasized separately in the right column.

(D) Cell population ratios by age groups; 3-, 6-, 12-, and 21-month-old $App^{NL\text{-}G\text{-}F}$ mouse data from Sala Frigerio et al., 2019 (Table S1).

(E) WAM and DAM2 populations analyzed separately. Shown is a heatmap with the top 20 DEGs for DAM2 and WAMs. Each row represents a gene and each column a single cell; 947 cells in total, of which 644 are WAMs and 303 DAM2.

(F) KEGG pathway enrichment for WAM and DAM2 upregulated DEGs.

(G) Bar plot showing the relative distribution of each microglia population in APP/PS1 and APP/PS1 $Apoe^{-/-}$.

(H) UMAP of microglia from APP/PS1 and APP/PS1 $Apoe^{-/-}$ combined, using the WAM signature genes.

mice, we found that white matter microglia nodules were completely absent, showing that their formation depends on TREM2 as in normal aging (Figure S7G). These data show that microglia in the white matter of mouse models of AD show a response that is associated with white matter aging, suggesting that myelin degeneration and debris clearance start much earlier in the presence of β-amyloid (Aβ) pathology. To distinguish DAM clustering around amyloid plaques from microglia nodules in

white matter, we determined differentially expressed genes in WAM and DAM2 (Figure 7E). Interestingly, the KEGG pathway enrichment analysis showed that DAM2 upregulated genes involved in multiple disease pathways, including AD, Parkinson's disease, and Huntington's diseases, whereas WAM upregulated genes linked to atherosclerosis, cytokine signaling, and apoptosis (Figure 7F). Next we searched for genes with different expression levels in WAMs compared with DAMs (Figure S7H). *ApoE* and *Tyrobp/Dap12*, which are required for signaling functions in AD (Wang et al., 2015; Krasemann et al., 2017), were found to be upregulated in DAMs. In addition, the inflammatory cytokine macrophage migration inhibitory factor (*Mif*) was expressed at higher levels in DAMs. *Srgap2*, *Cd33*, and *Abca1* are genes that were elevated in WAMs, whereas *Serinc3*, *Lyz2*, and *Clec7a* are examples of genes that were expressed at similar levels in WAMs and DAMs (Figure S7H). Next, we wanted to find out whether we could spatially separate the different microglia states in brain sections of models of AD. We used antibodies against MIF, a gene found to be expressed at higher levels in DAMs compared with WAMs, and found that virtually all microglia associated with amyloid plaques stained positive for MIF, but this was not the case for microglia forming nodules in white matter (Figure S7I). In contrast, antibodies against CLEC7A immunolabeled both populations of microglia (Figure S7J). Next we compared the numbers of CLEC7A and MIF-positive cells in white matter during aging of wild-type mice. We found hardly any MIF-positive cells until 18 months of age; only at 24 months of age were ~4% of IBA^+ cells immunolabeled for MIF. This was in contrast to CLEC7A, which was expressed in cells in white matter earlier and to a much higher extent (20.75% ± 9.67% $CLEC7A^+IBA1^+$ cells/area at 24 months) (Figures S7K and S7L).

Next we determined whether WAM and DAM formation depends on similar signal pathways in the aged brain compared with AD. Because previous work has shown that the APOE-TREM2 pathway triggers DAM conversion in AD models (Krasemann et al., 2017), and because *ApoE* and *Tyrobp/Dap12* were found to be upregulated in DAMs, we tested the requirement of APOE in aging and AD. In the APP/PS1 AD model from Sala Frigerio et al. (2019), we identified an ~8-fold reduction of DAM populations in the $Apoe^{-/-}$ genotype, whereas microglia with the WAM signature were reduced by ~4-fold (Figures 7G and 7H).

To determine whether WAMs are also generated in an APOE-dependent pathway in aged mice, we used droplet-based scRNA-seq on white matter of 18-month-old wild-type and $Apoe^{-/-}$ mice (13,954 high-quality cells from 8 mice used in four independent Drop-seq runs; Figure 8A; Figures S8A–S8C). Tissues were prepared as described above for the Drop-seq dataset, and cells were partitioned into major cell types (Figure 8A). We focused our analysis on microglia using white matter signature genes. These analyses identified a continuous range of microglia that reproduced the four microglial states in the previous scRNA-seq datasets (Figure 8B). Furthermore, wild-type and $Apoe^{-/-}$ mouse white matter had similar ratios of WAMs and activated microglia (Figure 8C). This result suggests that WAM formation is not APOE dependent in aging. To validate the scRNA-seq results, we co-stained $IBA1^+$ microglia with antibodies against CLEC7A, AXL, and LGALS3 in 21-month-old wild-type and $Apoe^{-/-}$ mice. Quantification revealed that similar numbers of $IBA1^+$ cells were positive for CLEC7A, AXL, and LGALS3 (Figure 8D). Notably, nodules containing $IBA1^+$ cells with MBP^+ intracellular particles were observed to the same extent in 21-month-old wild-type and $Apoe^{-/-}$ mice (Figure 8E). Thus, WAMs appear to be generated in an APOE-independent pathway in aged mice, whereas, in models of AD, generation of microglia with the DAM and WAM gene signature require APOE function.

DISCUSSION

In this study, we identified WAMs, which are age dependent, require TREM2 for their formation, and are defined by activation of genes implicated in phagocytic activity and lipid metabolism. WAMs localize in nodules that are engaged in clearing myelin debris in white matter. They display partial activation of the DAM program and form in the absence of APOE in normal aging. WAM identification was possible by performing scRNA-seq on microglia purified from white and gray matter separately and by integrating this spatial information into gene clustering. Using this WAM signature of differentially expressed genes in white and gray matter microglia, we also identified WAMs in previous scRNA-seq datasets (Hammond et al., 2019; Sala Frigerio et al., 2019), providing evidence of the robustness and reproducibility of our findings.

Why does white matter aging specifically shape microglial identity? Although aging is known to result in gray and white matter damage, it is possible that the extent of myelin sheath degeneration and/or the nature of the lipid-rich membrane are responsible for TREM2-dependent microglial responses in white matter. Indeed, when we analyzed microglia in a mouse model for Pelizaeus-Merzbacher disease, in which myelin is gradually broken down because of a mutation in an oligodendrocyte-specific gene, *Plp1*, we observed that microglia nodules containing myelin debris were already formed after a few months in white but not gray matter. Gray matter predominantly consists of neuronal cell bodies and dendrites but is also composed of myelinated axons. It is possible that the extent of myelin degeneration is not sufficient to trigger WAM responses in gray matter. However, our data do not exclude that microglia with the WAM signature can occur outside of white matter; for example, in diseases such as AD, where amyloid plaques trigger cell death in the gray matter. WAM and DAM states are likely to be continuous cell identities that can blend with each other in a continuum. In aging, microglia activation appears to be dominated by the WAM state, whereas it is shifted toward DAMs in AD. Proliferative region-associated microglia (PAM) subsets that share characteristics with DAMs have been identified previously in postnatal white matter at a time point that correlates with oligodendrocyte precursor cell apoptosis (Li et al., 2019). However, in contrast to the cells we identified in this study, PAMs do not require TREM2 for their formation (Li et al., 2019).

TREM2 is a V-type immunoglobulin (Ig) domain-containing receptor that binds to a variety of different ligands, such as various apolipoprotein and anionic lipid species (Ulrich et al., 2017). TREM2 can also function as a receptor for myelin debris uptake (Cantoni et al., 2015; Poliani et al., 2015; Wang et al., 2015), and

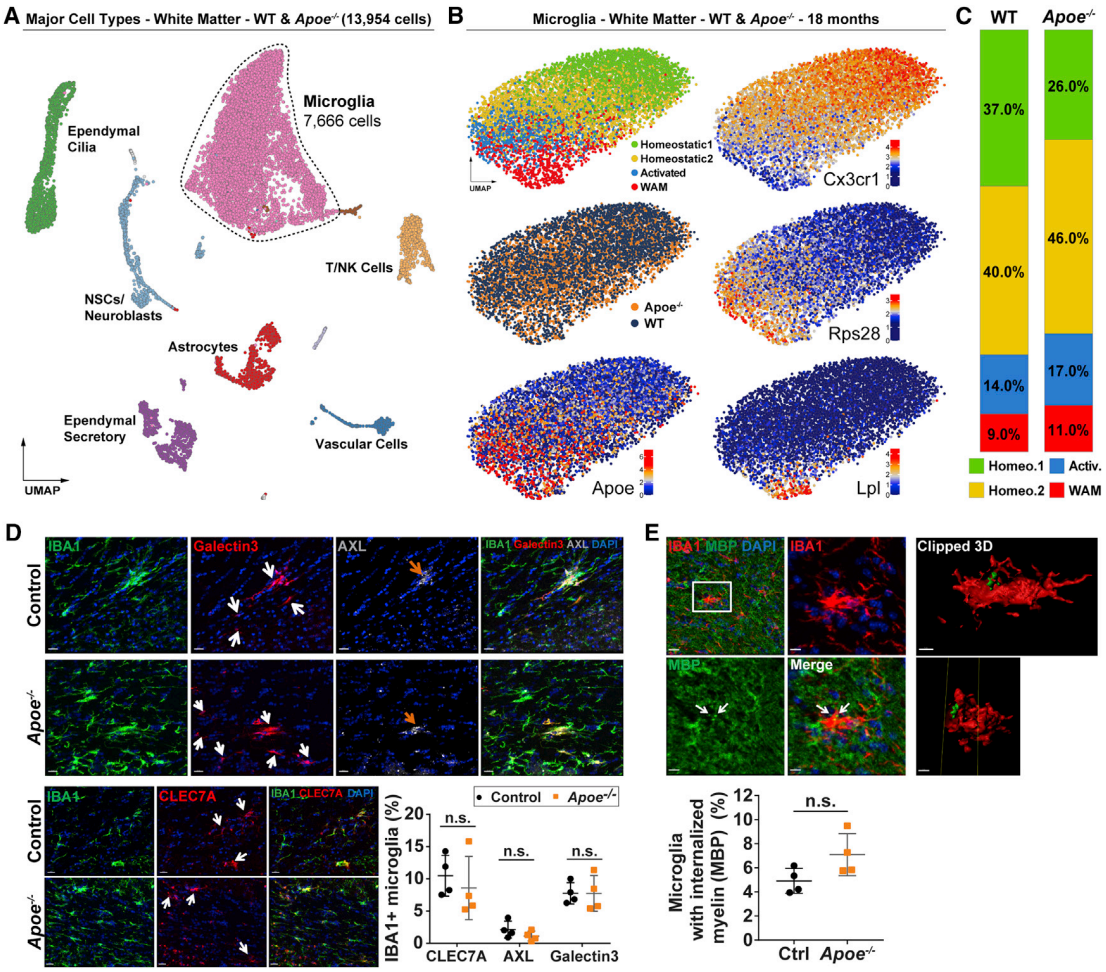

Figure 8. The WAM response is induced in an APOE-independent pathway in aged mice

(A) UMAP of 13,954 single-cell transcriptomes, colored by major cell-type clusters. 18 months old, WM only, WT, and *Apoe*$^{-/-}$.

(B) UMAP of microglia (7,666 cells), depicting the identified populations, genotype annotation, and expression of representative marker genes.

(C) Bar plot showing the relative distribution of each microglia population in WT WM and *Apoe*$^{-/-}$ WM.

(D) Confocal images of CLEC7A, AXL, and Galectin-3 co-localized with IBA1^{+} microglia (green) in the *corpus callosum* in 21-month-old *Apoe*$^{-/-}$ and control mice. Scale bar, 20 μm. Also shown is quantification of the percentage of IBA1^{+} microglia expressing CLEC7A, AXL, and Galectin-3 in 21-month-old *Apoe*$^{-/-}$ and control mice in the WM (*corpus callosum*; n = 4 mice per group, mean ± SD; AXL, p = 0.2348; CLEC7A, p = 0.5373; Galectin-3, p = 0.9962; Student's two-tailed t test).

(E) Confocal images of microglia nodules (red) containing internalized MBP-labeled myelin particles (green) in the *corpus callosum* of a 21-month-old *Apoe*$^{-/-}$ mouse (arrows). The clipped 3D reconstruction shows myelin within microglia. Scale bars, 20 μm (overview), 8 μm (magnification), and 5 μm (clipped 3D). Also shown is quantification of microglia with internalized myelin particles in the *corpus callosum* of 21-month-old *Apoe*$^{-/-}$ and age-matched control mice (*corpus callosum*, n = 4 mice per group, mean ± SD, p = 0.0753, Student's two-tailed t test).

our results concur with these studies but show that TREM2 is dispensable for myelin phagocytosis. We find that myelin debris uptake occurs by a wide range of phosphatidylserine receptors that are most likely able to compensate for the loss of TREM2 receptor activity. Thus, our data provide evidence of an essential function of TREM2 not in phagocytic uptake but in mediating the genetic response required to degrade and metabolize lipid-rich myelin debris when internalization has occurred. For cargos that do not depend on phosphatidylserine interactions, such as beads or bacteria, the function of TREM2 in phagocytosis appears to be more critical (Linnartz-Gerlach et al., 2019).

Complete loss of TREM2 function causes polycystic lipomembranous osteodysplasia with sclerosing leukoencephalopathy (PLOSL or Nasu-Hakola disease), a disease characterized by progressive presenile dementia and bone cysts associated with accumulation of lipomembranous structures in adipose tissue, bone marrow, and the brain (Bianchin et al., 2010). An overarching pathogenic mechanism could be an inability to initiate metabolic pathways required for degradation of lipid-rich membrane structures in tissue-resident macrophages. Loss of TREM2 in mice results in a much more subtle myelin phenotype with only a modest increase in degenerated myelin

profiles in aged mice. It is possible that the short lifespan of mice is not sufficient to induce leukodystrophy as seen in humans. Compensatory functions of astrocytes taking over myelin debris clearance when microglia become dysfunctional is another possible explanation. Rare variants in the *Trem2* gene have also been shown to increase an individual's risk of developing AD, which is associated with misfolded and aggregated proteins (Guerreiro et al., 2013; Jonsson et al., 2013). Several studies have shown that TREM2 is required to induce the DAM program in models of AD (Keren-Shaul et al., 2017; Krasemann et al., 2017; Mathys et al., 2017). DAMs increase with progression of amyloid deposition and accumulate close to amyloid plaques, where they are involved in Aβ phagocytosis and plaque compaction (Condello et al., 2015; Wang et al., 2016; Keren-Shaul et al., 2017). The different functional requirements of microglia in aging and in neurodegenerative diseases raise the question of how these microglial populations differ. In aging, we find that the distinct genetic modules of reactive microglia are segregated in subpopulations, with activated microglia displaying upregulation of translation-associated genes and WAMs exhibiting activation of lysosomal, phagocytic, and lipid metabolism pathways. Although WAMs are the predominant microglial subpopulation induced by aging, our bioinformatics analyses reveal that microglia with WAM and DAM signatures coexist in models of AD. In the context of these disease models, microglia with the WAM signature appear to be generated earlier than DAMs. Interestingly, the proportion of DAMs showed a decrease between 12 and 21 months, possibly because microglial cell death in the DAM populations and repopulation with homeostatic microglia or DAMs returning to the homeostatic state. Previously, we developed methods to distinguish discrete versus continuous heterogeneity in scRNA-seq data (Stanley et al., 2020), and WAM and DAM identities are good examples of continuous cell identities without clear separation. Our data show that microglia in the white matter of mouse models of AD form nodules containing MBP^{+} intracellular particles relatively early in disease, suggesting that myelin degeneration and debris clearance start prematurely in AD. Strikingly, in the Dominantly Inherited Alzheimer's Network (DIAN), white matter alterations were detected by MRI in individuals with autosomal dominant, fully penetrant mutations for AD up to 20 years before the expected onset of symptoms (Lee et al., 2016). The nature of these alterations is not fully resolved but possibly reflects demyelination and axonal damage (Brun and Englund, 1986; Prins and Scheltens, 2015; Nasrabady et al., 2018).

One interesting distinguishing feature of DAM and WAM responses appears to be their differential dependence on APOE. Previous work has shown that the APOE pathway triggers DAM conversion in models of neurodegeneration (Krasemann et al., 2017). Notably, our analyses reveal that, in the absence of APOE, fewer microglia with the WAM gene signature are generated in AD mouse models, whereas microglia with features of WAM are detected in similar numbers in aged white matter of $Apoe^{-/-}$ and wild-type mice, suggesting that the activity of APOE depends on the brain environment. How APOE triggers WAM/DAM conversion in AD models but not in aging is an open question. APOE, which is produced in excess in AD, could act directly on microglia, possibly by binding to TREM2 and activating downstream signaling (Atagi et al., 2015; Bailey et al., 2015; Yeh et al., 2016). Because APOE is critical for Aβ deposition and its subsequent fibrillization into amyloid deposits, amyloid-dependent indirect effects on microglia are another possible explanation for APOE-dependent microglial activation in AD (for a review, see Chen et al., 2021).

It is important to understand the relationship between activated microglia, WAMs, and DAMs. One possibility is that they are generated from homeostatic microglia, but it is also conceivable that they represent progressive activation states. Although such transformations are, in general, regarded as a protective response (Deczkowska et al., 2018), precocious DAM conversion may also cause harm by exhausting DAM function or inducing pro-inflammatory damage. Recently, lipid droplet-accumulating microglia have been identified in the aging brain (Marschallinger et al., 2020). These cells were defective in phagocytosis and produced high levels of reactive oxygen species and pro-inflammatory cytokines, representing a dysfunctional or dystrophic microglial state.

In summary, we identify WAMs as a novel microglial state associated with white matter aging. We propose that WAMs represent a protective metabolic response required to clear the increasing amounts of myelin debris that accumulate during aging. Because the WAM signature is also associated with phagosome as well as antigen processing and presentation, harmful functions, such as immune reactivity, cannot be excluded. In addition, we speculate that attrition of WAM function could contribute to development of neurodegenerative disease by accumulation of toxic protein or lipid species in the brain. If this is the case, then enhancing formation of WAMs could be used therapeutically; for example, to help to combat the age-associated decline of white matter function and possibly also dementia resulting from white matter involvement. Transcriptional signatures differ between mouse and human microglia (Masuda et al., 2019; Zhou et al., 2020), but interesting differences between human gray and white matter microglia have been detected (Sankowski et al., 2019), raising the possibility that WAMs also exist in humans.

STAR★METHODS

Detailed methods are provided in the online version of this paper and include the following:

- KEY RESOURCES TABLE
- RESOURCE AVAILABILITY
  - Lead contact
  - Materials availability
  - Data and code availability
- EXPERIMENTAL MODEL AND SUBJECT DETAILS
  - Mice
- METHOD DETAILS
  - Mice perfusion, cell isolation for Smart-seq2
  - Library preparation for Smart-seq2
  - Processing and analyses of Smart-seq2 data
  - Mice perfusion, cell isolation for Drop-seq
  - Library preparation for Drop-seq
  - Processing and analyses of Drop-seq data

- Processing and analyses of external datasets
- Immunohistochemistry
- RNAscope *in Situ* Hybridization
- Bulk RNA Sequencing
- Transmission Electron Microscopy
- Correlative Light and Scanning Electron Microscopy
- Myelin isolation and purification
- Myelin uptake assay
- Microglia-myelin binding assay
- Myelin clearance assay
- Lysolecithin-induced demyelination
- Gene expression analysis
- Western Blotting
- Image processing and analysis

● QUANTIFICATION AND STATISTICAL ANALYSIS

SUPPLEMENTAL INFORMATION

Supplemental Information can be found online at https://doi.org/10.1016/j.neuron.2021.01.027.

ACKNOWLEDGMENTS

The work was supported by grants from the German Research Foundation (TRR128-2, TRR 274 - ID 408885537, SyNergy Excellence Cluster EXC2145, Projekt ID390857198, and RO 4076/3-2), the ERC (consolidator grant to M.S.), the Dr. Miriam and Sheldon G. Adelson Medical Research Foundation, the Chan Zuckerberg Initiative (CZI), and a NARSAD Young Investigator Award (to O.G.). For the single-cell and sorting studies, we are grateful for support from the Flow Cytometric Cell Sorter Sony SH800 Core Unit run by the Department of Vascular Biology at the Institute for Stroke and Dementia Research (ISD) and SyNergy EXC2145. We thank Christian Haass for providing Trem2 knockout and App^{NL-G-F} transgenic mice and Sabina Tahirovic for providing mouse sections. We thank Jürgen Bernhagen for providing the rabbit anti-MIF antibody. Preclinical PET imaging was supported by the Deutsche Forschungsgemeinschaft (DFG) by dedicated PET imaging grants (BR4580/1-1 and RO5194/1-1). ActiGliA is funded by the DFG under Germany's Excellence Strategy within the framework of the Munich Cluster for Systems Neurology (EXC 2145 SyNergy – ID 390857198, Project D1) and by a Manfred Strohscher Fellowship provided by Hirnliga e.V.

AUTHOR CONTRIBUTIONS

M. Simons and O.G. conceived and supervised the project. S.S., S.B.-G., T.K., M. Schifferer, L.L., N.K., O.G., H.J., F.U., L.C.-C., M.J.R., R.P., G.G., M.B., D.F., and X.X. performed experiments and analyzed the data. S.B.-G. and T.K. developed software and curated and visualized the scRNA-seq data. O.G., M.R., and M. Simons analyzed the data or supervised data acquisition. M. Simons and O.G. wrote the manuscript with input from all authors.

DECLARATION OF INTERESTS

The authors declare no competing interests.

Received: August 31, 2020
Revised: December 8, 2020
Accepted: January 26, 2021
Published: February 18, 2021

REFERENCES

Atagi, Y., Liu, C.C., Painter, M.M., Chen, X.F., Verbeeck, C., Zheng, H., Li, X., Rademakers, R., Kang, S.S., Xu, H., et al. (2015). Apolipoprotein E Is a Ligand for Triggering Receptor Expressed on Myeloid Cells 2 (TREM2). J. Biol. Chem. *290*, 26043–26050.

Ayata, P., Badimon, A., Strasburger, H.J., Duff, M.K., Montgomery, S.E., Loh, Y.E., Ebert, A., Pimenova, A.A., Ramirez, B.R., Chan, A.T., et al. (2018). Epigenetic regulation of brain region-specific microglia clearance activity. Nat. Neurosci. *21*, 1049–1060.

Bailey, C.C., DeVaux, L.B., and Farzan, M. (2015). The Triggering Receptor Expressed on Myeloid Cells 2 Binds Apolipoprotein E. J. Biol. Chem. *290*, 26033–26042.

Bianchin, M.M., Martin, K.C., de Souza, A.C., de Oliveira, M.A., and Rieder, C.R. (2010). Nasu-Hakola disease and primary microglial dysfunction. Nat. Rev. Neurol. *6*, 2 p following 523.

Borchelt, D.R., Ratovitski, T., van Lare, J., Lee, M.K., Gonzales, V., Jenkins, N.A., Copeland, N.G., Price, D.L., and Sisodia, S.S. (1997). Accelerated amyloid deposition in the brains of transgenic mice coexpressing mutant presenilin 1 and amyloid precursor proteins. Neuron *19*, 939–945.

Brun, A., and Englund, E. (1986). A white matter disorder in dementia of the Alzheimer type: a pathoanatomical study. Ann. Neurol. *19*, 253–262.

Butler, A., Hoffman, P., Smibert, P., Papalexi, E., and Satija, R. (2018). Integrating single-cell transcriptomic data across different conditions, technologies, and species. Nat. Biotechnol. *36*, 411–420.

Cantoni, C., Bollman, B., Licastro, D., Xie, M., Mikesell, R., Schmidt, R., Yuede, C.M., Galimberti, D., Olivecrona, G., Klein, R.S., et al. (2015). TREM2 regulates microglial cell activation in response to demyelination in vivo. Acta Neuropathol. *129*, 429–447.

Cantuti-Castelvetri, L., Fitzner, D., Bosch-Queralt, M., Weil, M.T., Su, M., Sen, P., Ruhwedel, T., Mitkovski, M., Trendelenburg, G., Lütjohann, D., et al. (2018). Defective cholesterol clearance limits remyelination in the aged central nervous system. Science *359*, 684–688.

Cardona, A., Saalfeld, S., Schindelin, J., Arganda-Carreras, I., Preibisch, S., Longair, M., Tomancak, P., Hartenstein, V., and Douglas, R.J. (2012). TrakEM2 software for neural circuit reconstruction. PLoS ONE *7*, e38011.

Chen, W.T., Lu, A., Craessaerts, K., Pavie, B., Sala Frigerio, C., Corthout, N., Qian, X., Laláková, J., Kühnemund, M., Voytyuk, I., et al. (2020). Spatial Transcriptomics and In Situ Sequencing to Study Alzheimer's Disease. Cell *182*, 976–991.e19.

Chen, Y., Strickland, M.R., Soranno, A., and Holtzman, D.M. (2021). Apolipoprotein E: Structural Insights and Links to Alzheimer Disease Pathogenesis. Neuron *109*, 205–221.

Condello, C., Yuan, P., Schain, A., and Grutzendler, J. (2015). Microglia constitute a barrier that prevents neurotoxic protofibrillar Aβ42 hotspots around plaques. Nat. Commun. *6*, 6176.

Deczkowska, A., Keren-Shaul, H., Weiner, A., Colonna, M., Schwartz, M., and Amit, I. (2018). Disease-Associated Microglia: A Universal Immune Sensor of Neurodegeneration. Cell *173*, 1073–1081.

Dobin, A., Davis, C.A., Schlesinger, F., Drenkow, J., Zaleski, C., Jha, S., Batut, P., Chaisson, M., and Gingeras, T.R. (2013). STAR: ultrafast universal RNA-seq aligner. Bioinformatics *29*, 15–21.

Fang, T., Lu, X., Berger, D., Gmeiner, C., Cho, J., Schalek, R., Ploegh, H., and Lichtman, J. (2018). Nanobody immunostaining for correlated light and electron microscopy with preservation of ultrastructure. Nat. Methods *15*, 1029–1032.

Finak, G., McDavid, A., Yajima, M., Deng, J., Gersuk, V., Shalek, A.K., Slichter, C.K., Miller, H.W., McElrath, M.J., Prlic, M., et al. (2015). MAST: a flexible statistical framework for assessing transcriptional changes and characterizing heterogeneity in single-cell RNA sequencing data. Genome Biol. *16*, 278.

Friedman, B.A., Srinivasan, K., Ayalon, G., Meilandt, W.J., Lin, H., Huntley, M.A., Cao, Y., Lee, S.H., Haddick, P.C.G., Ngu, H., et al. (2018). Diverse Brain Myeloid Expression Profiles Reveal Distinct Microglial Activation States and Aspects of Alzheimer's Disease Not Evident in Mouse Models. Cell Rep. *22*, 832–847.

Füger, P., Hefendehl, J.K., Veeraraghavalu, K., Wendeln, A.C., Schlosser, C., Obermüller, U., Wegenast-Braun, B.M., Neher, J.J., Martus, P., Kohsaka, S., et al. (2017). Microglia turnover with aging and in an Alzheimer's model via long-term in vivo single-cell imaging. Nat. Neurosci. *20*, 1371–1376.

Gokce, O., Stanley, G.M., Treutlein, B., Neff, N.F., Camp, J.G., Malenka, R.C., Rothwell, P.E., Fuccillo, M.V., Südhof, T.C., and Quake, S.R. (2016). Cellular Taxonomy of the Mouse Striatum as Revealed by Single-Cell RNA-Seq. Cell Rep. *16*, 1126–1137.

Grabert, K., Michoel, T., Karavolos, M.H., Clohisey, S., Baillie, J.K., Stevens, M.P., Freeman, T.C., Summers, K.M., and McColl, B.W. (2016). Microglial brain region-dependent diversity and selective regional sensitivities to aging. Nat. Neurosci. *19*, 504–516.

Guerreiro, R., Wojtas, A., Bras, J., Carrasquillo, M., Rogaeva, E., Majounie, E., Cruchaga, C., Sassi, C., Kauwe, J.S., Younkin, S., et al.; Alzheimer Genetic Analysis Group (2013). TREM2 variants in Alzheimer's disease. N. Engl. J. Med. *368*, 117–127.

Haimon, Z., Volaski, A., Orthgiess, J., Boura-Halfon, S., Varol, D., Shemer, A., Yona, S., Zuckerman, B., David, E., Chappell-Maor, L., et al. (2018). Re-evaluating microglia expression profiles using RiboTag and cell isolation strategies. Nat. Immunol. *19*, 636–644.

Hammond, T.R., Dufort, C., Dissing-Olesen, L., Giera, S., Young, A., Wysoker, A., Walker, A.J., Gergits, F., Segel, M., Nemesh, J., et al. (2019). Single-Cell RNA Sequencing of Microglia throughout the Mouse Lifespan and in the Injured Brain Reveals Complex Cell-State Changes. Immunity *50*, 253–271.e6.

Jonsson, T., Stefansson, H., Steinberg, S., Jonsdottir, I., Jonsson, P.V., Snaedal, J., Bjornsson, S., Huttenlocher, J., Levey, A.I., Lah, J.J., et al. (2013). Variant of TREM2 associated with the risk of Alzheimer's disease. N. Engl. J. Med. *368*, 107–116.

Keren-Shaul, H., Spinrad, A., Weiner, A., Matcovitch-Natan, O., Dvir-Szternfeld, R., Ulland, T.K., David, E., Baruch, K., Lara-Astaiso, D., Toth, B., et al. (2017). A Unique Microglia Type Associated with Restricting Development of Alzheimer's Disease. Cell *169*, 1276–1290.e17.

Kleinberger, G., Brendel, M., Mracsko, E., Wefers, B., Groeneweg, L., Xiang, X., Focke, C., Deußing, M., Suárez-Calvet, M., Mazaheri, F., et al. (2017). The FTD-like syndrome causing TREM2 T66M mutation impairs microglia function, brain perfusion, and glucose metabolism. EMBO J. *36*, 1837–1853.

Krasemann, S., Madore, C., Cialic, R., Baufeld, C., Calcagno, N., El Fatimy, R., Beckers, L., O'Loughlin, E., Xu, Y., Fanek, Z., et al. (2017). The TREM2-APOE Pathway Drives the Transcriptional Phenotype of Dysfunctional Microglia in Neurodegenerative Diseases. Immunity *47*, 566–581.e9.

Kubota, Y., Sohn, J., Hatada, S., Schurr, M., Straehle, J., Gour, A., Neujahr, R., Miki, T., Mikula, S., and Kawaguchi, Y. (2018). A carbon nanotube tape for serial-section electron microscopy of brain ultrastructure. Nat. Commun. *9*, 437.

Lee, S., Viqar, F., Zimmerman, M.E., Narkhede, A., Tosto, G., Benzinger, T.L., Marcus, D.S., Fagan, A.M., Goate, A., Fox, N.C., et al.; Dominantly Inherited Alzheimer Network (2016). White matter hyperintensities are a core feature of Alzheimer's disease: Evidence from the dominantly inherited Alzheimer network. Ann. Neurol. *79*, 929–939.

Leng, L., Metz, C.N., Fang, Y., Xu, J., Donnelly, S., Baugh, J., Delohery, T., Chen, Y., Mitchell, R.A., and Bucala, R. (2003). MIF signal transduction initiated by binding to CD74. J. Exp. Med. *197*, 1467–1476.

Li, Q., Cheng, Z., Zhou, L., Darmanis, S., Neff, N.F., Okamoto, J., Gulati, G., Bennett, M.L., Sun, L.O., Clarke, L.E., et al. (2019). Developmental Heterogeneity of Microglia and Brain Myeloid Cells Revealed by Deep Single-Cell RNA Sequencing. Neuron *101*, 207–223.e10.

Linnartz-Gerlach, B., Bodea, L.G., Klaus, C., Ginolhac, A., Halder, R., Sinkkonen, L., Walter, J., Colonna, M., and Neumann, H. (2019). TREM2 triggers microglial density and age-related neuronal loss. Glia *67*, 539–550.

Lloyd, A.F., Davies, C.L., Holloway, R.K., Labrak, Y., Ireland, G., Carradori, D., Dillenburg, A., Borger, E., Soong, D., Richardson, J.C., et al. (2019). Central nervous system regeneration is driven by microglia necroptosis and repopulation. Nat. Neurosci. *22*, 1046–1052.

Love, M.I., Huber, W., and Anders, S. (2014). Moderated estimation of fold change and dispersion for RNA-seq data with DESeq2. Genome Biol. *15*, 550.

Luckner, M., and Wanner, G. (2018). From Light Microscopy to Analytical Scanning Electron Microscopy (SEM) and Focused Ion Beam (FIB)/SEM in Biology: Fixed Coordinates, Flat Embedding, Absolute References. Microsc. Microanal. *24*, 526–544.

Marschallinger, J., Iram, T., Zardeneta, M., Lee, S.E., Lehallier, B., Haney, M.S., Pluvinage, J.V., Mathur, V., Hahn, O., Morgens, D.W., et al. (2020). Lipid-droplet-accumulating microglia represent a dysfunctional and proinflammatory state in the aging brain. Nat. Neurosci. *23*, 194–208.

Masuda, A., Kobayashi, Y., Kogo, N., Saito, T., Saido, T.C., and Itohara, S. (2016). Cognitive deficits in single App knock-in mouse models. Neurobiol. Learn. Mem. *135*, 73–82.

Masuda, T., Sankowski, R., Staszewski, O., Böttcher, C., Amann, L., Sagar, Scheiwe, C., Nessler, S., Kunz, P., van Loo, G., et al. (2019). Spatial and temporal heterogeneity of mouse and human microglia at single-cell resolution. Nature *566*, 388–392.

Mathys, H., Adaikkan, C., Gao, F., Young, J.Z., Manet, E., Hemberg, M., De Jager, P.L., Ransohoff, R.M., Regev, A., and Tsai, L.H. (2017). Temporal Tracking of Microglia Activation in Neurodegeneration at Single-Cell Resolution. Cell Rep. *21*, 366–380.

Mathys, H., Davila-Velderrain, J., Peng, Z., Gao, F., Mohammadi, S., Young, J.Z., Menon, M., He, L., Abdurrob, F., Jiang, X., et al. (2019). Single-cell transcriptomic analysis of Alzheimer's disease. Nature *570*, 332–337.

McKenzie, I.A., Ohayon, D., Li, H., de Faria, J.P., Emery, B., Tohyama, K., and Richardson, W.D. (2014). Motor skill learning requires active central myelination. Science *346*, 318–322.

Mount, C.W., and Monje, M. (2017). Wrapped to Adapt: Experience-Dependent Myelination. Neuron *95*, 743–756.

Nasrabady, S.E., Rizvi, B., Goldman, J.E., and Brickman, A.M. (2018). White matter changes in Alzheimer's disease: a focus on myelin and oligodendrocytes. Acta Neuropathol. Commun. *6*, 22.

Norton, W.T., and Poduslo, S.E. (1973). Myelination in rat brain: method of myelin isolation. J. Neurochem. *21*, 749–757.

Oakley, H., Cole, S.L., Logan, S., Maus, E., Shao, P., Craft, J., Guillozet-Bongaarts, A., Ohno, M., Disterhoft, J., Van Eldik, L., et al. (2006). Intraneuronal beta-amyloid aggregates, neurodegeneration, and neuron loss in transgenic mice with five familial Alzheimer's disease mutations: potential factors in amyloid plaque formation. J. Neurosci. *26*, 10129–10140.

Pan, S., Mayoral, S.R., Choi, H.S., Chan, J.R., and Kheirbek, M.A. (2020). Preservation of a remote fear memory requires new myelin formation. Nat. Neurosci. *23*, 487–499.

Perry, V.H., and Holmes, C. (2014). Microglial priming in neurodegenerative disease. Nat. Rev. Neurol. *10*, 217–224.

Peters, A. (2002). The effects of normal aging on myelin and nerve fibers: a review. J. Neurocytol. *31*, 581–593.

Picelli, S., Faridani, O.R., Björklund, A.K., Winberg, G., Sagasser, S., and Sandberg, R. (2014). Full-length RNA-seq from single cells using Smart-seq2. Nat. Protoc. *9*, 171–181.

Plemel, J.R., Stratton, J.A., Michaels, N.J., Rawji, K.S., Zhang, E., Sinha, S., Baaklini, C.S., Dong, Y., Ho, M., Thorburn, K., et al. (2020). Microglia response following acute demyelination is heterogeneous and limits infiltrating macrophage dispersion. Sci. Adv. *6*, eaay6324.

Poliani, P.L., Wang, Y., Fontana, E., Robinette, M.L., Yamanishi, Y., Gilfillan, S., and Colonna, M. (2015). TREM2 sustains microglial expansion during aging and response to demyelination. J. Clin. Invest. *125*, 2161–2170.

Prins, N.D., and Scheltens, P. (2015). White matter hyperintensities, cognitive impairment and dementia: an update. Nat. Rev. Neurol. *11*, 157–165.

Prinz, M., Jung, S., and Priller, J. (2019). Microglia Biology: One Century of Evolving Concepts. Cell *179*, 292–311.

Readhead, C., Schneider, A., Griffiths, I., and Nave, K.A. (1994). Premature arrest of myelin formation in transgenic mice with increased proteolipid protein gene dosage. Neuron *12*, 583–595.

Rock, R.B., Gekker, G., Hu, S., Sheng, W.S., Cheeran, M., Lokensgard, J.R., and Peterson, P.K. (2004). Role of microglia in central nervous system infections. Clin. Microbiol. Rev. *17*, 942–964.

Safaiyan, S., Kannaiyan, N., Snaidero, N., Brioschi, S., Biber, K., Yona, S., Edinger, A.L., Jung, S., Rossner, M.J., and Simons, M. (2016). Age-related myelin degradation burdens the clearance function of microglia during aging. Nat. Neurosci. *19*, 995–998.

Sala Frigerio, C., Wolfs, L., Fattorelli, N., Thrupp, N., Voytyuk, I., Schmidt, I., Mancuso, R., Chen, W.T., Woodbury, M.E., Srivastava, G., et al. (2019). The Major Risk Factors for Alzheimer's Disease: Age, Sex, and Genes Modulate the Microglia Response to Aβ Plaques. Cell Rep. *27*, 1293–1306.e6.

Salter, M.W., and Stevens, B. (2017). Microglia emerge as central players in brain disease. Nat. Med. *23*, 1018–1027.

Sankowski, R., Böttcher, C., Masuda, T., Geirsdottir, L., Sagar, Sindram, E., Seredenina, T., Muhs, A., Scheiwe, C., Shah, M.J., et al. (2019). Mapping microglia states in the human brain through the integration of high-dimensional techniques. Nat. Neurosci. *22*, 2098–2110.

Sasaguri, H., Nilsson, P., Hashimoto, S., Nagata, K., Saito, T., De Strooper, B., Hardy, J., Vassar, R., Winblad, B., and Saido, T.C. (2017). APP mouse models for Alzheimer's disease preclinical studies. EMBO J. *36*, 2473–2487.

Sowell, E.R., Peterson, B.S., Thompson, P.M., Welcome, S.E., Henkenius, A.L., and Toga, A.W. (2003). Mapping cortical change across the human life span. Nat. Neurosci. *6*, 309–315.

Stadelmann, C., Timmler, S., Barrantes-Freer, A., and Simons, M. (2019). Myelin in the Central Nervous System: Structure, Function, and Pathology. Physiol. Rev. *99*, 1381–1431.

Stanley, G., Gokce, O., Malenka, R.C., Südhof, T.C., and Quake, S.R. (2020). Continuous and Discrete Neuron Types of the Adult Murine Striatum. Neuron *105*, 688–699.e8.

Steadman, P.E., Xia, F., Ahmed, M., Mocle, A.J., Penning, A.R.A., Geraghty, A.C., Steenland, H.W., Monje, M., Josselyn, S.A., and Frankland, P.W. (2020). Disruption of Oligodendrogenesis Impairs Memory Consolidation in Adult Mice. Neuron *105*, 150–164.e6.

Street, K., Risso, D., Fletcher, R.B., Das, D., Ngai, J., Yosef, N., Purdom, E., and Dudoit, S. (2018). Slingshot: cell lineage and pseudotime inference for single-cell transcriptomics. BMC Genomics *19*, 477.

Streit, W.J., Sammons, N.W., Kuhns, A.J., and Sparks, D.L. (2004). Dystrophic microglia in the aging human brain. Glia *45*, 208–212.

Szklarczyk, D., Gable, A.L., Lyon, D., Junge, A., Wyder, S., Huerta-Cepas, J., Simonovic, M., Doncheva, N.T., Morris, J.H., Bork, P., et al. (2019). STRING v11: protein-protein association networks with increased coverage, supporting functional discovery in genome-wide experimental datasets. Nucleic Acids Res. *47* (D1), D607–D613.

Tapia, J.C., Kasthuri, N., Hayworth, K.J., Schalek, R., Lichtman, J.W., Smith, S.J., and Buchanan, J. (2012). High-contrast en bloc staining of neuronal tissue for field emission scanning electron microscopy. Nat. Protoc. *7*, 193–206.

Tischer, J., Krueger, M., Mueller, W., Staszewski, O., Prinz, M., Streit, W.J., and Bechmann, I. (2016). Inhomogeneous distribution of Iba-1 characterizes microglial pathology in Alzheimer's disease. Glia *64*, 1562–1572.

Turnbull, I.R., Gilfillan, S., Cella, M., Aoshi, T., Miller, M., Piccio, L., Hernandez, M., and Colonna, M. (2006). Cutting edge: TREM-2 attenuates macrophage activation. J. Immunol. *177*, 3520–3524.

Ulrich, J.D., Ulland, T.K., Colonna, M., and Holtzman, D.M. (2017). Elucidating the Role of TREM2 in Alzheimer's Disease. Neuron *94*, 237–248.

Van Hove, H., Martens, L., Scheyltjens, I., De Vlaminck, K., Pombo Antunes, A.R., De Prijck, S., Vandamme, N., De Schepper, S., Van Isterdael, G., Scott, C.L., et al. (2019). A single-cell atlas of mouse brain macrophages reveals unique transcriptional identities shaped by ontogeny and tissue environment. Nat. Neurosci. *22*, 1021–1035.

Wang, Y., Cella, M., Mallinson, K., Ulrich, J.D., Young, K.L., Robinette, M.L., Gilfillan, S., Krishnan, G.M., Sudhakar, S., Zinselmeyer, B.H., et al. (2015). TREM2 lipid sensing sustains the microglial response in an Alzheimer's disease model. Cell *160*, 1061–1071.

Wang, Y., Ulland, T.K., Ulrich, J.D., Song, W., Tzaferis, J.A., Hole, J.T., Yuan, P., Mahan, T.E., Shi, Y., Gilfillan, S., et al. (2016). TREM2-mediated early microglial response limits diffusion and toxicity of amyloid plaques. J. Exp. Med. *213*, 667–675.

Wang, F., Ren, S.Y., Chen, J.F., Liu, K., Li, R.X., Li, Z.F., Hu, B., Niu, J.Q., Xiao, L., Chan, J.R., and Mei, F. (2020). Myelin degeneration and diminished myelin renewal contribute to age-related deficits in memory. Nat. Neurosci. *23*, 481–486.

Wu, Y.E., Pan, L., Zuo, Y., Li, X., and Hong, W. (2017). Detecting Activated Cell Populations Using Single-Cell RNA-Seq. Neuron *96*, 313–329.e6.

Ximerakis, M., Lipnick, S.L., Innes, B.T., Simmons, S.K., Adiconis, X., Dionne, D., Mayweather, B.A., Nguyen, L., Niziolek, Z., Ozek, C., et al. (2019). Single-cell transcriptomic profiling of the aging mouse brain. Nat. Neurosci. *22*, 1696–1708.

Yeh, F.L., Wang, Y., Tom, I., Gonzalez, L.C., and Sheng, M. (2016). TREM2 Binds to Apolipoproteins, Including APOE and CLU/APOJ, and Thereby Facilitates Uptake of Amyloid-Beta by Microglia. Neuron *91*, 328–340.

Zheng, G.X., Terry, J.M., Belgrader, P., Ryvkin, P., Bent, Z.W., Wilson, R., Ziraldo, S.B., Wheeler, T.D., McDermott, G.P., Zhu, J., et al. (2017). Massively parallel digital transcriptional profiling of single cells. Nat. Commun. *8*, 14049.

Zhou, Y., Zhou, B., Pache, L., Chang, M., Khodabakhshi, A.H., Tanaseichuk, O., Benner, C., and Chanda, S.K. (2019). Metascape provides a biologist-oriented resource for the analysis of systems-level datasets. Nat. Commun. *10*, 1523.

Zhou, Y., Song, W.M., Andhey, P.S., Swain, A., Levy, T., Miller, K.R., Poliani, P.L., Cominelli, M., Grover, S., Gilfillan, S., et al. (2020). Human and mouse single-nucleus transcriptomics reveal TREM2-dependent and TREM2-independent cellular responses in Alzheimer's disease. Nat. Med. *26*, 131–142.

STAR★METHODS

KEY RESOURCES TABLE

REAGENT or RESOURCE	SOURCE	IDENTIFIER
Antibodies		
Rabbit anti-IBA1	Wako	Cat#019-19741; RRID: AB_839504
Guinea anti-pig IBA1	Synaptic Systems	Cat#234004; RRID: AB_2493179
Rat anti-MAC2 (Galectin 3)	Biolegend	Cat#125402; RRID: AB_1134238
Rat anti-MBP (Myelin Basic Protein)	Abcam	Cat#ab7349; RRID: AB_305869
Mouse anti-PLP (Proteolipid Protein)	Bio-Rad	Cat#MCA839G; RRID: AB_2237198
Chicken anti-MBP (Myelin Basic Protein)	Thermofisher Scientific	Cat#PA1-10008; RRID: AB_1077024
Rat anti-CD68	Bio Rad	Cat#MCA1957; RRID: AB_322219
Goat anti-AXL (Tyrosine-protein kinase receptor)	R&D Systems	Cat# AF854; RRID: AB_355663
Rat anti CLEC7A (DECTIN1) (Clec7a)	InvivoGen	Cat#mabg-mdect; RRID: AB_2753143
Rabbit anti-TMEM119 (Transmembrane Protein 1119)	Abcam	Cat#ab209064; RRID: AB_2800343
Rat anti-P2RY12 (Purinergic receptor P2Y, G-protein coupled12)	Biolegend	Cat#848002; RRID: AB_2650634
Rat anti-CD45 (eFluor 450, 30-F11)	Thermofisher Scientific	Cat#48-0451-82; RRID: AB_1518806
Rat anti-CD11b (PE/Cy7, M1/70)	Thermofisher Scientific	Cat#25-0112-82; RRID: AB_469588
Mouse anti-PU.1	Santa Cruz	Cat#sc-390405; RRID: N/A
Mouse anti-beta-Amyloid (NAB228)	Santa Cruz	Cat#sc-32277; RRID: AB_626670
Goat anti-Cathepsin L	R&D Systems	Cat#AF1515; RRID: AB_2087690
Rabbit anti-MIF	Prof. Jürgen Bernhagen (Laboratory of Vascular Biology, ISD, Munich).	Leng et al., 2003
Biological samples		
Mouse brain sections: 21 months old ApoE KO	Dr. Dirk Fitzner (Department of Neurology, University of Göttingen)	N/A
Mouse brain sections: 2 and 6 months old 5xFAD	Dr. Sabine Tahirovich (Laboratory of *ex vivo* models, DZNE, Munich	N/A
Mouse brain sections: 6 months old App NL-G-F Knock-in	Dr. Sabine Tahirovich (Laboratory of *ex vivo* models, DZNE, Munich)	N/A
Mouse brain sections: 18 months old *App NL-G-F; Trem2*$^{-/-}$	Prof. Christian Haass (Laboratory of Neurodegenerative Disease Research, DZNE, Munich)	N/A
Chemicals, peptides, and recombinant proteins		
FluoroMyelin, green fluorescent myelin stain	Invitrogen	Cat#F34651
Annexin-V, Alexa Fluor 555 conjugate	Thermofisher Scientific	Cat#A35108
CD11b (Microglia) microbeads, human and mouse	Miltenyi Biotec	Cat#130-093-634
Actinomycin D	Sigma-Aldrich	No. A1410; CAS: 50-76-0
Fc-blocking reagent (CD16/CD32 Monoclonal Antibody (93)	Thermofisher Scientific	Cat#14-0161-82; RRID: AB_467133
Aminoactinomycin D (7AAD)	Thermofisher Scientific	Cat# A1310
Prolong gold antifade reagent	Invitrogen	Cat#P36934
L-α-Lysophosphatidylcholine from egg yolk (L-α-lysolecithin)	Sigma-Aldrich	Cat#L4129; CAS: 9008-30-4
Bafilomycin	InvivoGen	Cat#tlrl-baf1
Leupeptin Hemisulfate	Selleckchem	Cat#S7380; CAS: 103476-89-7
Recombinant ribonuclease inhibitor	Takara Clontech	Cat#2313B
Triton X-100	Sigma-Aldrich	Cat#93443
SMARTScribe Reverse Transcriptase	Takara Clontech	Cat#639538
Betaine solution 5 M, PCR Reagent	Sigma-Aldrich	Cat#B0300

(*Continued on next page*)

Continued

REAGENT or RESOURCE	SOURCE	IDENTIFIER
UltraPure Dithiothreitol	Thermofisher Scientific	Cat#15508013
Magnesium chloride solution for molecular biology, 1.00 M ± 0.01 M	Sigma-Aldrich	Cat#M1028
Lambda Exonuclease	New England Biolabs	Cat#M0262L
AMPure XP Beads	Beckman-Coulter	Cat#A63881
Myelin Removal Beads II	Miltenyi Biotec	Cat#130-096-731
Critical commercial assays		
PKH67 Green Fluorescent Cell Linker Kit for General Cell Membrane Labeling,	Sigma-Aldrich	Cat#PKH67GL-1KT
RNAscope multiplex fluorescent reagent kit v2 assay	Advanced Cell Diagnostics	Cat#323100-USM
Neural Tissue Dissociation Kit (P)	Miltenyi Biotec	Cat#130-092-628
KAPA HiFi HotStart ReadyMix PCR Kit	Roche	Cat#KK2602 07958935001
Agilent High Sensitivity DNA Kit	Agilent	Cat#5067-4626
Qubit dsDNA HS Assay Kit	Thermofisher Scientific	Cat# Q32854
Chromium Next GEM Single Cell 3′ GEM, Library & Gel Bead Kit v3.1	10x Genomics	Cat#1000121
Deposited data		
Raw and analyzed data	This manuscript	SRA/GEO
Experimental models: cell lines		
Human: HeLa cells	ATCC	HeLa (ATCC CCL2)
Experimental models: organisms/strains		
Mouse: C57BL/6J	Janvier Labs	N/A
Mouse: Trem2$^{-/-}$	Prof. Christian Haass (Laboratory of Neurodegenerative Disease Research, DZNE, Munich),	Turnbull et al., 2006
Mouse: B6.129P2-Apoe^{tm1Unc}/J (ApoE KO)	The Jackson Laboratory	Stock#002052
Mouse: B6SJL-Tg (APPSwFILon, PSEN1*M146L*L286V)6799Vas/Mmjax (5xFAD)	The Jackson Laboratory	Stock#034840-JAX; RRID: MMRRC_034840-JAX
Mouse: APP NL-G-F Knock-in	Takaomi Saido	N/A
Mouse: APP NL-G-F; Trem2$^{-/-}$	Prof. Christian Haass (Laboratory of Neurodegenerative Disease Research, DZNE, Munich)	N/A
Mouse: B6.129P-Cx3cr1tm1Litt/J	The JacksonLaboratory	Stock#005582
Oligonucleotides		
qPCR: hexosaminidase (Forward): GCTGCAGAATCCTTTGCTTACGG	This manuscript	N/A
qPCR: hexosaminidase (Reverse): GGGTCACGTGAACGGGAGG	This manuscript	N/A
qPCR: N-acetylglucosamine-6-sulfatase (Forward): GAAAACCAAGGCCCTCATCG	This manuscript	N/A
qPCR: N-acetylglucosamine-6-sulfatase (Reverse): TGTTGTTAACGACGTGGTGG	This manuscript	N/A
qPCR: Galactosidase Beta 1 (Forward): CACTGCCTAACGGAGAGACC	This manuscript	N/A
qPCR: Galactosidase Beta 1 (Reverse): TCCCGAGATGTATCGGAATGG	This manuscript	N/A
qPCR: Cathepsin L (Forward): TCGGATTTCACCTCAGTGTCC	This manuscript	N/A
qPCR: cathepsin L (Reverse): CTTAAAAACTAGTGGGGCTGGC	This manuscript	N/A
ERCC RNA	Ambion – Fisher Scientific	Cat#4456740

(*Continued on next page*)

Continued

REAGENT or RESOURCE	SOURCE	IDENTIFIER
oligo-dT primer (with tag): AAGCAGTGGTATCAACG CAGAGTACTTTTTTTTTTTTTTTTTTTTTTTTTTTTTTVN	Eurogentec	DNA Wobble 200 nmol
dNTP Mix	Thermofisher Scientific	Cat# R0192
Template-switching oligos (TSO): AAGCAGTGGTAT CAACGCAGAGTACrGrG+G	Eurogentec	DNA LNA 200 nmol
ISPCR primers: 5′ AAGCAGTGGTATCAACGCAGAGT-3	Eurogentec	DNA Base 200 nmol scale
qPCR: Ubb77 (Primer1): 5′-GGAGAGTCCATCGTGGTTATTT-3′	This manuscript	N/A
qPCR: Ubb77 (Primer2): 5′-ACCTCTAGGGTGATGGTCTT-3′	This manuscript	N/A
qPCR: Ubb77 (Probe): 5′-/5Cy5/TGCAGATCTTCGTG AAGACCTGAC/3IAbRQSp/-3′	This manuscript	N/A
Recombinant DNA		
Plasmid: Tim4 (Myc-DDK-tagged)	OriGene Technologies	Cat#MR222206; NM_178759
Plasmid: Tim1 (Havcr1) (Myc-DDK-tagged)	OriGene Technologies	Cat#MR227388; NM_134248
Plasmid: Fcgr1 (Myc-DDK-tagged)	OriGene Technologies	Cat#MR225268; NM_010186
Plasmid: Olr1 (Myc-DDK-tagged)	OriGene Technologies	Cat#MR226641; NM_138648
Plasmid: Msr1 (Myc-DDK-tagged)	OriGene Technologies	Cat#MR205384; NM_031195
Plasmid: Siglech (Myc-DDK-tagged)	OriGene Technologies	Cat#MR204374; NM_178706
Plasmid: Cd33 (Myc-DDK-tagged)	OriGene Technologies	Cat#MR219960; NM_021293
Plasmid: Cd68 (Myc-DDK-tagged)	OriGene Technologies	Cat#MR204757; NM_BC021637
Plasmid: Sirpa (Myc-DDK-tagged)	OriGene Technologies	Cat#MR226909; NM_007547
Plasmid: Cd209a (Myc-DDK-tagged)	OriGene Technologies	Cat#MR225861; NM_133238
Plasmid: Cd300a (Myc-DDK-tagged)	OriGene Technologies	Cat#MR224901; NM_170758
Plasmid: Axl (Myc-DDK-tagged)	OriGene Technologies	Cat# MR211073; NM_009465
Plasmid: Jmjd6 (Myc-DDK-tagged)	OriGene Technologies	Cat#MR206341; NM_033398
Plasmid: Itgam (CR3)	Addgene	Cat#8631; RRID:Addgene_8631
Plasmid: Itgav (C-treminal His tag)	Addgene	Cat#27290; RRID:Addgene_27290
Plasmid: Cd36 (EGFP)	Addgene	Cat#21853; RRID: Addgene_21853
Plasmid: Dectin1A (Clec7a, tdTomato tag)	Addgene	Cat#58089; RRID: Addgene_58089
Plasmid: Human Mertk (C-Flag tag)	Sino Biological	Cat., HG10298-CF; NM_006343.2
Plasmid: Trem2-DAP12 (with a HA-tag at N terminus)	Prof. Christian Haass (Laboratory of Neurodegenerative Disease Research, DZNE, Munich)	N/A
Software and algorithms		
ImageJ	https://imagej.net/Welcome	RRID:SCR_003070
Graphpad Prism	https://www.graphpad.com:443/	RRID:SCR_002798
Imaris	Bitplane	RRID:SCR_007370
rnaSTAR	Dobin et al., 2013	https://github.com/alexdobin/STAR
FastQC	Simon Andrews	https://github.com/s-andrews/FastQC
Cutadapt	Marcel Martin	https://github.com/marcelm/cutadapt/
Trimgalore	Felix Krueger	https://github.com/FelixKrueger/TrimGalore
Seurat	Butler et al., 2018	https://github.com/satijalab/seurat
DESeq2	Love et al., 2014	https://github.com/mikelove/DESeq2
MAST	Finak et al., 2015	https://github.com/RGLab/MAST/
Slingshot	Street et al., 2018	https://github.com/kstreet13/slingshot
10x Genomics Cell Ranger	Zheng et al., 2017	https://support.10xgenomics.com/single-cell-gene-expression/software/pipelines/latest/what-is-cell-ranger
Metascape	Zhou et al., 2019	http://metascape.org/
STRING	Szklarczyk et al., 2019	https://string-db.org

(*Continued on next page*)

Continued

REAGENT or RESOURCE	SOURCE	IDENTIFIER
Other		
RNAscope Probe: Mm-ITGAX assigned to channel 1	Advanced Cell Diagnostics	Cat#311501
RNAscope Probe: 3-Plex positive control probe-Mm	Advanced Cell Diagnostics	Cat# 320881
RNAscope Probe: 3-Plex negative control probe (dapB)	Advanced Cell Diagnostics	Cat#320871
RNAscope Probe: Probe diluent	Advanced Cell Diagnostics	Cat#300041

RESOURCE AVAILABILITY

Lead contact

Further information and requests for resources and reagents should be directed to and will be fulfilled by the Lead Contact, Mikael Simons (mikael.simons@dzne.de).

Materials availability

All unique reagents generated in this study are available from the Lead Contact with a completed Material Transfer Agreement.

Data and code availability

Single-cell sequencing data generated during this study are available in the NCBI database through accession number NCBI: GSE166548 and bulk sequencing data generated during this study are available through accession number NCBI: GSE166304. All other data that support findings are available upon request from the authors.

EXPERIMENTAL MODEL AND SUBJECT DETAILS

Mice

All animal experiments were reviewed and overseen by the institutional animal use and care committee in German Center for Neurodegenerative Diseases (DZNE) in Munich. The following mouse lines were used in the study: Wild-type C57BL/6J mice from Janvier Labs; *Trem2*$^{-/-}$ mice in the C57BL/6J background (Turnbull et al., 2006, the mice were provided by Prof. Christian Haass, Laboratory of Neurodegenerative Disease Research, DZNE, Munich), ApoE KO mice (B6.129P2-Apoe^{tm1Unc}/J, Jackson Laboratory, Stock No. 002052, the brain sections were provided by Dr. Dirk Fitzner, Department of Neurology, University of Göttingen); 5xFAD mice (B6SJL-Tg (APPSwFILon, PSEN1*M146L*L286V) 6799 Vas/Mmjax, Jackson Laboratory, stock No. 034840-JAX, the brain sections were provided by Dr. Sabine Tahirovic, Laboratory of *ex vivo* models, DZNE, Munich); APP $^{NL-G-F}$ Knock-in mice (available through Takaomi Saido, Ph.D.Wako-shi, Saitama 351-0198, Japan, the brain sections were provided by Dr. Sabine Tahirovic (Laboratory of *ex vivo* models, DZNE, Munich); APP $^{NL-G-F}$ Trem2$^{-/-}$ mice (the brain sections were provided by Prof. Christian Haass, Laboratory of Neurodegenerative Disease Research, DZNE, Munich); CX3CR1^{GFP} (B6.129P-Cx3cr1^{tm1Litt}/J, Jackson Laboratory, Stock No. 005582). The mice were kept in groups of three in Greenline IVC GM500 plastic cages and were housed in a temperature-controlled environment (21 ± 2°C) on a 12 h light/dark cycle with food and water available *ad libitum* in the animal facility in German Center for Neurodegenerative Diseases (DZNE) in Munich. The ApoE KO mice were kept under the same condition in the animal facility of Max Planck Institute of Experimental Medicine in Göttingen. Pups were bred in-house and kept with the adult female under standard light/dark conditions until P21, then they were weaned. Most of the experiments including immunohistochemistry, scRNA sequencing and electron microscopy were performed on adult mice at the age of 2, 6, 12, 18, 20 and 24 months. The exact age of mice used for each analysis is indicated in the figure legends. Mice were aged either in house or purchased from Janvier Labs. Both males and females were included in all analyses and we did not notice any influence of sex on our analyzed parameters in the study. For microglia isolation, P6-P8 C57BL/6J wild-type or knockout mice and for myelin extraction from brain, 2 months old C57BL/6J wild-type mice were used. lysolecithin injection was done on 9 to 15 weeks old mice. The mice and samples including brain sections were allocated into experimental groups randomly. *Cell line:* HeLa cells were grown in Dulbecco's modified Eagle's medium (DMEM) supplemented by 10% FCS. For maintenance, these cells were re-suspended in the freezing media containing 50% FCS and 10% DMSO at concentration of 5×10^6 to 1×10^7 *cells*/mL. Aliquots in 1.5 mL cryo-tubes were frozen slowly at 1°C/min by placing tubes in a NALGENE cryo freezing container in –80°C freezer, then transferring to liquid nitrogen storage.

METHOD DETAILS

Mice perfusion, cell isolation for Smart-seq2

The mice were deeply anesthetized and perfused with cold HBSS between 9am-11am (to decrease circadian fluctuations). Each brain was removed and under a dissection microscope individually micro-dissected; gray matter was isolated from the frontal cortex and white matter form optic tract, *medial lemniscus* and *corpus callosum* (attached gray matter and choroid plexus were removed

carefully) isolated. We developed and established a microglia isolation protocol that prevents *ex-vivo* transcription and automatizes the mechanical isolation parts using GentleMacs with the Neural Tissue Dissociation Kit (Papain) (Miltenyi Biotec). We added actinomycin D (Act-D, Sigma, No. A1410) to a final concentration of 45 μM into the dissociation solution and enzyme mix to prevent *ex-vivo* transcription. The dissociated cell suspension was passed through a 70 μm cell strainer (Corning, 352350) before labeling. Subsequently, cells were blocked with mouse FcR-blocking reagent (CD16/CD32 Monoclonal Antibody, eBioscience cat:14-0161-82,1100) and then stained for 15 min using 7AAD (Thermo Fisher, A1310, 25 ug/mL) and the antibodies against CD45 (eFluor 450, 30-F11, eBioscience,Cat.:48-0451-82, 1:200) and CD11b (PE/Cy7,M1/70, eBioscience, Cat:48-0451-82,1:200) and after washed with PBS (Sigma, D8537). Viable (7AAD negative) single immune cells (CD45 and CD11b positive cells) were sorted by flow cytometry (SH800; Sony). For GFP positive microglia from CX3CR1$^{GFP/+}$ mice, cells were either dissociated with Act-D or without and labeled with DAPI (4',6-diamidino-2-phenylindole, 1:4000 dilution; Sigma) to label dead cells. After FSC-A/FSC-H selection of single-cells, DAPI negative and GFP positive cells were selected. Single immune cells (CD45 and CD11b positive cells) were sorted by flow cytometry (SH800; Sony). Flow cytometry data were analyzed using FlowJo v10. Single-cells were sorted into 96 well plates filled with 4 μL lysis buffer containing 0.05% Triton X-100 (Sigma) and, ERCC (External RNA Controls Consortium) RNA spike-in Mix (Ambion, Life Technologies) (1:24000000 dilution), 2.5 μM oligo-dT, 2.5 mM dNTP and 2 U/μL of recombinant RNase inhibitor (Clontech) then spun down and frozen at −80°C. Plates were thawed and libraries prepared as described below.

Library preparation for Smart-seq2

The 96-well plates containing the sorted single cells were first thawed and then incubated for 3 min at 72°C and thereafter immediately placed on ice. To perform reverse transcription (RT) we added each well a mix of 0.59 μL H2O, 0.5 μL SMARTScribe Reverse Transcriptase (Clontech), 2 μL 5x First Strand buffer, 0.25 μL Recombinant RNase Inhibitor (Clontech), 2 μL Betaine (5 M Sigma), 0.5 μL DTT (100 mM) 0.06 μL MgCl2 (1 M Sigma), 0.1 μL Template-switching oligos (TSO) (100 μM AAGCAGTGGTATCAAC GCAGAGTACrGrG+G). Next RT reaction mixes were incubated at 42°C for 90 min followed by 70°C for 5 min and 10 cycles of 50°C 2 min, 42°C 2 min; finally ending with 70°C for 5 min for enzyme inactivation. Pre-amplification of cDNA was performed by adding 12.5 μL KAPA HiFi Hotstart 2x (KAPA Biosystems), 2.138 μL H2O, 0.25 μL ISPCR primers (10 μM, 5′ AAGCAGTGGTATCAACG CAGAGT-3), 0.1125 μL Lambda Exonuclease under the following conditions: 37°C for 30 min, 95°C for 3 min, 23 cycles of (98°C for 20 s, 67°C for 15 s, 72°C for 4 min), and a final extension at 72°C for 5 min. Libraries were then cleaned using AMPure bead (Beckman-Coulter) cleanup at a 0.7:1 ratio of beads to PCR product. Libraries were assessed by Bio-analyzer (Agilent 2100), using the High Sensitivity DNA analysis kit, and also fluorometrically using Qubit's DNA HS assay kits and a Qubit 4.0 Fluorometer (Invitrogen, LifeTechnologies) to measure the concentrations. Further selection of samples was performed via qPCR assay against ubiquitin transcripts Ubb77 (primer 1 5′-GGAGAGTCCATCGTGGTTATTT-3′ primer 2 5′-ACCTCTAGGGTGATGGTCTT-3′, probe 5′-/5Cy5/TGCA GATCTTCGTGAAGACCTGAC/3IAbRQSp/-3′) measured on a LightCycler 480 Instrument II (Roche). Samples were normalized to 160 pg/μL. Sequencing libraries were constructed by using in-house produced Tn5 transposase (Picelli et al., 2014). Libraries were barcoded and pooled then underwent three 3 rounds of AMPure bead (Beckman-Coulter) cleanup at a 0.8:1 ratio of beads to library. Libraries were sequenced 2x150 reads base pairs (bp) paired-end on Illumina HiSeq4000 to a depth of $3x10^5$–$6x10^5$ reads/sample.

Processing and analyses of Smart-seq2 data

BCL files were demultiplexed with the bcl2fastq software from Illumina. After quality-control with FastQC, reads were aligned using rnaSTAR (Dobin et al., 2013) to the GRCm38 (mm10) genome with ERCC synthetic RNA added. Read counts were collected using the parameter "quantMode GeneCounts" of rnaSTAR and using the unstranded values. From that point, Seurat R v.2.3.4 package was used (Butler et al., 2018). Low-quality samples were filtered out from the dataset based on a threshold for the number of genes detected (min 1000 unique genes/cell), percentage of mitochondrial genes (max 0.5%), percentage of ERCCs (5% max) and number of reads on a log10 scale (between 4 to 5.5) as shown in Figure S1G and H. 1038 single-cells passed the quality-control. Gene expressions were log normalized to 10,000 using the NormalizeData function of Seurat. Dataset were scaled and depth of sequencing was regressed using ScaleData function and using the percentage of ERCCs. The first 12 principal components were considered for the UMAP of all cell types. Non-microglia cells were removed from analysis using markers and threshold such as performed by Keren-Shaul et al. (2017) and shown in Figures S1I and S1J. The first 8 principal components were used for the UMAP of microglia only. To find the clusters/populations of microglial states, hierarchical clustering (Ward's method) was used on the differentially expressed genes specific to the WAM cluster (FindClusters on first 8 PCs). To refine the WAM signature, differential expression analysis was performed using DESeq2 (Love et al., 2014) using FindAllMarkers. 212 genes were found significant at adjusted p value < 0.05 (Table S2). Gene sets of 1, 2, 3 and 4 were defined using hierarchical clustering (Ward's method) on the genes of the WAM signature. For the DAM signature, the top 500 genes were grouped by set in a similar way as described above. Slingshot analyses are based on the first 2 components of the PCA using the WAM signature genes. The previously described 4 clusters of microglia were used as input for Slingshot (Street et al., 2018). All gene ontology analyses were performed using Metascape (http://metascape.org/).

Mice perfusion, cell isolation for Drop-seq

Briefly, the mice were deeply anesthetized and perfused with cold HBSS between 9am-11am (to decrease circadian fluctuations). Each brain was removed and under a dissection microscope individually micro-dissected and dissociated same as described above.

After dissociation, myelin debris were removed using Myelin Removal Beads II (Miltenyi Biotec). The cells were resuspended in 0.04% BSA+PBS and cells were counted using automated cell counter (TC20 Bio-Rad) before loading to Chromium Controller.

Library preparation for Drop-seq

Single-cell suspensions were loaded onto the Chromium Single Cell Controller using the Chromium Single Cell 3′ Library & Gel Bead Kit v3.1 (10X Genomics) chemistry following the manufacturer's instructions. Sample processing and library preparation was performed according to manufacturer instructions using AMPure beads (Beckman Coulter). Libraries were sequenced on the DNBSEQ Sequencing System (BGI group).

Processing and analyses of Drop-seq data

Fastq files were processed with Cell Ranger v4 and aligned to the mm10 (Ensembl 93) genome. From that point, Seurat R v.3 package was used (Butler et al., 2018). Low-quality samples were filtered out from the dataset based on a threshold for the number of genes detected (min 200 unique genes/cell), percentage of mitochondrial genes (max 10%). 21197 out of 25719 and 13954 out of 17263 single-cells passed the quality-control for the aging and Apoe-KO datasets, respectively. Gene expressions were normalized using SCTransform function of Seurat. The first 30 principal components were considered for the UMAP of all cell types. Non-microglia cells were removed from analysis using markers genes as shown in Figures S2C and S2D. The first 15 principal components were used for the UMAP of microglia only. WAM populations were identified using the WAM signature gene set via hierarchical clustering (Ward's method). All gene ontology analyses were performed using Metascape (http://metascape.org/) and STRING (Szklarczyk et al., 2019). After identification of the novel microglial populations, WAM signature was used for generating the UMAPs, as described previously. For the *Apoe*$^{-/-}$ dataset, Apoe was omitted from the WAM signature while generating the UMAPs.

Processing and analyses of external datasets

External datasets from Hammond et al. and Frigerio et al. were analyzed with the same Seurat pipeline using Seurat 3 and MAST (Finak et al., 2015) for differential gene expression. For Hammond et al. (2019) datasets, raw data was downloaded from GSE121654. 4 samples for wild-type data; two replicates of each 1 month old (GSM3442024, GSM3442025) and 18 months old (GSM3442036, GSM3442037) were quality-controlled and processed as described above. After the QC steps, 9558 cells were kept for downstream analyses (Table S2). For Sala Frigerio et al. (2019) datasets, normalized datasets were available. Wild-Type and *App*$^{NL\text{-}G\text{-}F}$ data were downloaded from GSE127892 and analyzed separately. After filtering, 4856 and 5093 microglia were included in the downstream analyses for *App*$^{NL\text{-}G\text{-}F}$ dataset and WT dataset, respectively. The whole dataset acquired from GSE127892, consists of 32 experimental conditions, 2 mice per conditions as reported by the authors. Data for each condition were pooled (Table S1). Merging the current study and Sala Frigerio et al. (2019) wild-type data (Figure S3B) was established by using the Seurat 3 data integration functions. APP/PS1 and APP/PS1-*Apoe*$^{-/-}$ data were downloaded from GSE127884. After filtering, 1143 microglia were kept for downstream analyses. For the average heatmap (Figure S7A) from Keren-Shaul et al. (2017) data, their Table S2 was used to plot the average gene expression per microglial population for the 500 DAM signature genes.

Immunohistochemistry

Animals were anesthetized by intraperitoneal injection of 14% chloral hydrate, perfused transcardially with 4% paraformaldehyde. Post fixation of brain tissue was done in 4% PFA overnight. Then the brain tissue was further cryo-protected in 30% sucrose in PBS for 24 h. After freezing the tissue on dry ice using Tissue-Tek O.C.T, 30 μm coronal sections were cut by cryostat Leica CM 1900. Free-floating sections were collected in a solution containing 25% glycerol and 25% ethylenglycol in PBS. The sections were rinsed with 1x PBS containing 0.2% Tween-20 and permeabilized in 0.5% Triton X-100 for 10 to 30 min depending on primary antibody. Fab fragment goat anti mouse IgG (1:100) (Dianova) was added for 1 h at room temperature to block endogenous mouse tissue immunoglobulins. After a brief wash the sections were blocked for 1 h at room temperature in a solution containing 2.5% FCS, 2.5% BSA and 2.5% fish gelatin in PBS. Primary antibodies, diluted in 10% blocking solution, were added and incubated overnight at 4°C. On the following day sections were incubated with secondary antibodies, diluted in 10% blocking solution, for 1 h at room temperature. The sections were washed with PBS followed by distilled H_2O and mounted using fluorescence mounting medium (Dako) over superfrost plus slides. For AXL and CLEC7A staining, antigen retrieval protocol using citrate buffer (10 mM, pH 6) was performed on free-floating sections followed by staining protocol as mentioned above. The immunostaining of PU.1 was done as following. The free floating sections were permeabilized with 0.5% Triton X-100 for 30 min at room temperature. Then sections were treated with blocking solution containing 0.3% Triton X-100 for 24 hours at 4C. The primary antibody in blocking solution without Triton X-100 was incubated for 65 hours at 4C. the sections were incubated with secondary antibody in blocking solution at 4C over night.

RNAscope *in Situ* Hybridization

RNAscope *in situ* hybridization assay was applied to detect mRNA of *Itgax* in the brain cryosections prepared from aged and young wild-type mice. The assay was performed using a commercially available kit, RNAscope Multiplex Fluorescent Detection Reagents v2 (Advanced Cell Diagnostics, ACD) and the manufacturer instruction was followed. Briefly, 30 μm cryosections were fixed on superfrost plus slides; they were pretreated with hydrogenproxide for 10 min at room temperature and then with antigen retrieval reagent (5min boiling) to unmask the target RNA. After applying Protease III on the sections for 30 min at 40°C, probe hybridization was done

by incubating sections in mouse *Itgax* probe assigned to channel 1 (Cat. 311501), diluted 1:50 in probe diluent, for 2 h at 40°C. Positive control probes targeting housekeeping genes including *Polr2a*, *Ppib* and *Ubc*. (Advanced Cell Diagnostics, Hayward, CA) and 3-Plex negative control probes targeting the bacterial *DapB* gene (Advanced Cell Diagnostics, Hayward, CA) were used to test mRNA integrity in the tissue. Afterward, signal amplification and detection were performed according to the instruction of the kit. Signal detection was done using Opal dyes (Opal520-green) diluted 1:3000 in TSA buffer. To visualize microglia, after *in situ* hybridization, immunohistochemistry assay was performed using Iba1 antibody (Wako, 1:1000). The nuclei of cells were counterstained with DAPI (4',6-diamidino-2-phenylindole) and then the slides were mounted over superfrost plus slides using prolong gold antifade reagent (Invitrogen).

Bulk RNA Sequencing

The isolated microglia were homogenized in RLT buffer using QIAShredder (QIAGEN) and the total RNA was extracted using RNeasy Micro Kit (QIAGEN) and cDNA was synthesized using Ovation RNA-Seq System V2 (NuGEN). 1 μg of cDNA was used as input for Ion Xpress Plus Fragment Library Kit (ThermoFisher Scientific) to generate barcoded libraries. Barcoded libraries were then quantified using qRT-PCR (KAPA Library Quantification Kit). Barcoded libraries were then pooled and clonally amplified on Ion Spheres (Ion One Touch 200 Template Kit v2, ThermoFisher Scientific) and were sequenced on an Ion Proton sequencer (ThermoFisher Scientific). Raw reads were sorted based on barcodes and were subjected to quality analysis using FASTQC. The sequences were subsequently aligned to the genome of *Mus musculus* (GRCm38/Mm10) using the TMAP aligner with default parameters. The reads mapping to unique locations were quantified using RefSeq Gene Annotations(v73) into genes. Differential gene expression analysis and hypergeometric pathway analysis using KEGG genesets was performed using a commercial platform (Partek). Genes with fold change greater than 2 and p values less than 0.05 were considered for further hypergeometric pathway enrichment analysis.

Transmission Electron Microscopy

Mice brains were fixed in 2.5% glutaraldehyde and 4% paraformaldehyde in 0.1 M sodium cacodylate buffer at pH 7.4 after deep anesthesia (isoflurane) perfusion. Brains were vibratome sectioned and immersion fixed in the same buffer for 24 h at 4°C. After tissue trimming and washes in 0.1 M sodium cacodylate buffer, postfixation in reduced Osmium (2% Osmium, 2.5% potassium ferrocyanide in 0.1 M cacodylate buffer) was followed by en bloc uranyl acetate (1% aqueous uranylacetate) contrasting, graded dehydration in ethanol and embedding in epon resin (Serva). After ultrathin sectioning the grids (Leica UC7 ultramicrotome) were contrasted by 1% uranyl acetate and lead citrate (Ultrostain, Leica). Images were acquired with a JEOL JEM1400 plus TEM equipped with a Ruby 8Mpx CCD camera. For each analysis, randomly selected regions in three to five different animals were imaged. Data analysis was carried out using ImageJ 1.41.

Correlative Light and Scanning Electron Microscopy

The correlated workflow was adapted from Fang et al. (2018). Mice were perfused and brains fixed for 24 h in 4% paraformaldehyde and 3% w/v sucrose in 0.1 M PBS (pH 7.4). The brain tissue was sectioned into 100μm thick vibrotome sections. After 24 h incubation in fixative, smaller regions containing the corpus callosum were trimmed to restrict the correlation area and prevent tissue curving during the en bloc staining. The immunostaining was performed as mentioned before with a slight change. The sections were incubated with Iba1 antibody (Wako, 1:1000) for 48 h and with secondary antibody (Alexa Fluor 488, Invitrogen) overnight. Sections were stained with DAPI (1:2000 in PBS) for 5 min, washed in PBS and mounted on glass slides using secure-seal spacer (13 mm, 0.12 mm thickness, Invitrogen). Tile scans of the whole section with a 20x air objective and regions of interest with a 63x oil objective were acquired on a Leica TCS SP5 confocal microscope. After careful unmounting, sections were post-fixed (2.5% glutaraldehyde in 0.1 M sodium cacodylate buffer) for 24 h. In order to keep a flat orientation corresponding to the confocal imaging plane, the sections were glued onto of Aclar spears (Science Services) using Cell-Tak adhesive (Corning) (Luckner and Wanner, 2018). We applied a rOTO (reduced osmium-thiocarbohydrazide-somium) staining procedure adopted from Tapia et al. (2012). Briefly, the tissue was initially postfixed in 2% osmium tetroxide (EMS), 2% potassium ferricyanide (Sigma) in 0.1 M sodium cacodylate (Science Services) buffer (pH 7.4). After three washing steps in buffer and water the staining was enhanced by reaction with 1% thiocarbohydrazide (Sigma) for 45 min at 50°C. The tissue was washed in water and incubated in 2% aqueous osmium tetroxide. All osmium incubation steps were carried out over 90 min with substitution by fresh reagents after 45 min, respectively. To further intensify the staining, 2% aqueous uranyl acetate was applied overnight at 4°C and subsequently warmed to 50°C for 2 h. The samples were dehydrated in an ascending ethanol series and infiltrated with LX112 (LADD). The sample were flat embedded into gelatin capsules (Science Services) and cured for 48h. For SEM experiments without correlation samples were fixed as mentioned in the TEM protocol and subjected to the rOTO protocol described above. The block was trimmed by 200 μm at a 90° angle on each side using a TRIM90 diamond knife (Diatome) on an ATUMtome (Powertome, RMC). The front face was carefully trimmed to collect all sections beginning at the very surface areas that correspond to the confocal images (depth of 15-20 μm). Consecutive sections were taken with a 35° ultra-diamond knife (Diatome) at a nominal cutting thickness of 100nm and collected on freshly plasma-treated (custom-built, based on Pelco easiGlow, adopted from Mark Terasaki) CNT tape (Kubota et al., 2018). Starting from the block face with the complete tissue exposed we collected 300 ultrathin sections, covering a thickness of 30 μm in depth. Tape strips were mounted with adhesive carbon tape (Science Services) onto 4-inch silicon wafers (Siegert Wafer) and grounded by additional adhesive carbon tape strips (Science Services). EM micrographs were acquired on a Crossbeam Gemini 340 SEM (Zeiss) with a four-quadrant backscatter detector at 8 kV. In

ATLAS5 Array Tomography (Fibics), the whole wafer area was scanned at 2000-4000 nm/pixel to generate an overview map. For correlation, sections were selected and the entire corpus callosum region (1356 × 491 μm^2) of 177 sections (one wafer, 17.7 μm in z) scanned at 200 × 200 nm^2. The images were aligned by a sequence of automatic and manual processing steps in Fiji TrakEM2 (Cardona et al., 2012). The correlation was achieved by using nuclei and further anatomical landmarks (section border morphology, myelinated areas). Based on this correlation we selected an area in xy (544 × 324 × 13.9 μm^3) and the respective sections (corresponding to the ROI in z) for high resolution acquisition at 20 × 20 nm^2. After correlation of this dataset we imaged single images containing IBA1 positive cells at 4 × 4 nm^2.

Myelin isolation and purification

Myelin was isolated from 8-week-old C57BL/6 mice brains by sequential centrifugation on discontinuous sucrose gradient according to a protocol previously described (Norton and Poduslo, 1973) with some modifications. The ultracentrifugation was done using SW41 Ti rotor. The brain tissues were homogenized with a Dounce homogenizer in a solution containing 10 mM HEPES, 5mM EDTA, and 0.32 M sucrose. The homogenized tissue was layered on HEPES/EDTA buffer containing 0.85 M sucrose, centrifuged at 24600 rpm for 30 min with low deceleration and acceleration. The crude myelin fraction was removed from interface, resuspended in ice-cold distilled water, and centrifuged at 9500 rpm for 15 min. The hypo-osmotic shock was applied to the pellet two more times. The pellet from the last step was dissolved in HEPES/EDTA buffer containing 0.3 M sucrose, and placed over the 0.85 M sucrose; all the centrifugation steps and hypo-osmotic shocks were repeated as before. Eventually, the purified myelin pellet was resuspended in 1 mL PBS and stored at −20°C.

Myelin uptake assay

18 mm coverslips were coated with fibronectin in PBS (20 μg/mL) in the 24-well plates for 1 h in the incubator (37C, 5% CO_2). After changing PBS with the culture medium (DMEM plus 10% fetal calf serum, 1% Glutamax, and 0.5% antibiotics) HeLa Cells were seeded at 4 × 10^4 cells/mL and cultured with 5% CO_2 at 37°C for 18-24 h before transfection. 1 μg of expression plasmids were introduced into HeLa cells by the calcium phosphate precipitation method. The level of gene expression was tested 24-48 h after incubation. Next, transfected cells were treated with myelin as following. Purified myelin isolated from 2-month-old wild-type mouse brains was labeled with PKH67 (Sigma), and then washed in PBS by centrifugation at 15000 g. The final pellet was resuspended in culture medium and sonicated for 20 min in an ultrasound water bath. Transfected HeLa cells were treated with 4 μg PKH76-labeled myelin and incubated at 37°C in the presence of 5% CO_2 for 2 to 5 h. The cells were fixed in 4% PFA for 15 min and myelin uptake was assessed by immunocytochemistry.

Microglia-myelin binding assay

Microglia were isolated from C57BL/6, P6-P8 wild-type mice by MACS Technology. Brain tissue was dissociated using a Neural Tissue Dissociation Kit (Papain) (Miltenyi Biotec). Briefly, brain tissue was removed, cut into small pieces and dissociated by enzymatic digestion provided in the kit. The tissue suspension was applied to a 40 μm cell strainer, and washed twice with DMEM containing 1 mM sodium pyruvate. The final palette was resuspended in 10 volume of DMEM containing 10% FCS, 1 mM sodium pyruvate, 1% antibiotics (DMEM/FCS) plus 1 volume of CD11b microbeads (Miltenyi Biotec) and incubated at 4°C for 15 min. After washing with DMEM/FCS, the pellet was resuspended in 500 μL of the same medium, applied in a MACS column in the magnetic field, following three times wash, CD11b positive cells (microglia) were flushed out of the column, centrifuged at 400 x g for 10 min at 4°C. Isolated microglia were plated over 12 mm coverslips at 7 × 10^4 cell/mL, and incubated for 48-72 h. PKH67-labeled myelin was sonicated in an ultrasound water bath for 20 min. Primary microglia cultures were treated with 4 μg myelin and incubated on the ice for 2-4 h. Purified myelin was conjugated with Annexin V Alexa Fluor 555 (Thermo Fisher) as following. 4 μg of sonicated myelin was incubated with different concentration of Annexin V (13.5 M, 18 M and 22.5 M) in the binding buffer (10 mM HEPES, 140 mM NaCl, 2.5 mM CaCl2, pH 7.4) for 1 h at room temperature.

Myelin clearance assay

To analyze the rate of clearance of myelin debris, microglia cultures were pretreated with serum free DMEM, supplemented with 2 ng/mL TGF-β2 (Peprotech, 100-35B), 20 ng/mL CSF1 (M-CSF, Peprotech, 315-02) and 1.5 μg/mL cholesterol (Avanti Polar Lipids (Otto Nordwald), 700000P) (TCC medium). The cells were treated with 10 μg/mL myelin (or HEPES control) in the TCC medium for 2 h. After treatment, the cells were washed three times, and incubated with the TCC medium for 2 or 24 h. For the experiment with the inhibitors of lysosomal degradation, 100 nM Bafilomycin (Invivogen) or 10 μM leupeptin (Selleckchem) were administered 30 minutes before myelin administration and kept in the media until the end of the experiment. After fixation, the myelin in cells was stained using anti-PLP antibody; the cells were stained using DyLight 694 labeled tomato lectin (Vector Laboratories, DL-1178) and 2 μg/mL Hoechst 33342. The cells were imaged on a Leica SP5 confocal microscope with a 63x objective. For the quantification, the intensity of the PLP staining contained within the cell membrane was measured per cell.

Lysolecithin-induced demyelination

Stereotactic injection of lysolecithin in the spinal cord was performed in wt C57BL/6J and *Trem2*$^{-/-}$ mice that were 9 to 15 weeks old. 1% lysolecithin was prepared by dissolving L-α-Lysophosphatidylcholine from egg yolk (Sigma, L4129) in PBS, pH 7.4 (GIBCO,

10010056). 3% Monastral blue was prepared by dissolving Copper(II) phthalocyanine-tetrasulfonic acid tetrasodium salt (Aldrich, 274011) in milliq water, and the solution was sterilized by filtration through a 0.45-μm filter and autoclaving. Prior to injection, 1μl of 3% Monastral blue was mixed with 25μl of 1% lysolecithin. Glass Capillaries for Nanoliter 2010 (World Precision Instruments, 504949 or 4878) were pulled using the P-1000 Next Generation Micropipette Puller (Sutter Instrument). The program had the following parameters: Heat 530, Pull 0, Vel 60, Time 250, Pressure 500, Ramp 520, Microinjection – BF100.50.10, Tip < 1 μm, Taper 6-8 mm. R ~40-80 Meg, Heat = Ramp, FB255B, 2.5mm Box. Before surgery, the animals were anesthetized by intraperitoneal injection of 0.5 mg/kg body weight medetomidine, 5.0 mg/kg midazolam and 0.05 mg/kg fentanyl (MMF). The anesthetized animals were kept on a heating pad at 37°C, and the anesthetic depth was monitored by checking the reflex between the toes and the corneal reflex. The surgery and intraspinal injection of lysolecithin was conducted using the digital mouse stereotaxic frame and Nanoliter 2010 Injector with MICRO4 controller (World Precision Instruments) as previously described (Cantuti-Castelvetri et al., 2018). After the spinal cord was exposed, the capillary was positioned 0.55 mm lateral to the dorsal artery, and lowered 1.15 mm into the tissue. At each injection site, 1 μl of 1% lysolecithin containing 0.12% monastral blue was injected at a speed of 350 nl/min. 1 minute after the end of the delivery, the capillary was retracted. After injection, the skin was sutured, and the wound was sutured. After the operation, the animals were injected with 250 μl of 0.9% NaCl (normal saline solution) to compensate for the loss of blood and with the analgesic buprenorphine at a dose of 0.1 mg/kg. When MMF was used for anesthesia, 2.5 mg/kg atipamezole, 0.5 mg/kg flumazenil and 1.2 mg/kg naloxone (AFN) was injected IP for the animals to antagonize the anesthesia and awaken the animal. The animals were injected SC with buprenorphine for two days after surgery.

Gene expression analysis

For the preparation of RNA from cell, primary microglia was treated with myelin or fluoresbright beads. At the end of the treatment, the cells were collected in RLT buffer and the RNA was isolated with the RNAeasy isolation kit (QIAGEN, 74104). The RNA was retrotranscribed to cDNA with the Superscript III kit (Thermo Fisher Scientific, 18080051). For the quantitative PCR, the cDNA was quantified with the Power SYBR green PCR Master mix (4367659 Thermo Fisher Scientific) on a Applied Biosystem 7500 Fast Cycler, according to the PCR mix data sheet. The relative quantification of each gene was performed with the ΔΔCt method: each gene was quantified and its expression was normalized to the house keeper gene (Cytochrome C1, cyc1). The primers used for the analysis were:

hexosaminidase forward 5'-GCTGCAGAATCCTTTGCTTACGG-3′;
hexosaminidase reverse 5'-GGGTCACGTGAACGGGAGG-3′;
N-acetylglucosamine-6-sulfatase forward 5'-GAAAACCAAGGCCCTCATCG-3′;
N-acetylglucosamine-6-sulfatase reverse 5'-TGTTGTTAACGACGTGGTGG-3′;
Galactosidase Beta 1 forward 5'-CACTGCCTAACGGAGAGACC-3′;
Galactosidase Beta 1 reverse 5'-TCCCGAGATGTATCGGAATGG-3′;
Cathepsin L forward 5'-TCGGATTTCACCTCAGTGTCC-3′;
cathepsin L reverse 5'-CTTAAAAACTAGTGGGGCTGGC-3′.

Western Blotting

Following separation with SDS-PAGE, the proteins were transferred from the gel onto the nitrocellulose membrane using the mini Trans-Blot Module. The gel sandwich in blotting cassette was placed in the tank of the module containing transfer buffer (0.25 M Tris base, 1.92 M glycine, 20% methanol) with 100 V for 1 hour. The membrane was washed in PBST (0.1% Tween 20 in PBS) for 10 min, immersed in 4% skim milk powder in PBST as a blocking solution for 30 min at room temperature and then incubated with primary antibody in PBST at 4°C overnight. After washing, it was incubated with horse radish peroxidase (HRP)-conjugated secondary antibody in PBST for one hour at room temperature. Then targeted protein was detected with enhanced chemiluminescence method using Luminol enhancer and peroxide solutions (Pierce/Thermo Scientific) and was visualized with an Odyssey Fc imager from LI-COR.

Image processing and analysis

Images were acquired via a Leica TCS SP5 confocal microscope and were processed and analyzed with Imaris (64x version 9.2.0) and ImageJ 1.41 image processing software. For quantification of microglia nodules, a cluster of three or more cells that were identified by their nuclei labeled with DAPI or PU.1 antibody.

QUANTIFICATION AND STATISTICAL ANALYSIS

To compare more than two groups, one-way analysis of variance (ANOVA) followed by Bonferroni post hoc test was applied. A two-tailed Student's t test was performed for comparison of two groups. Two-way ANOVA followed by Bonferroni post hoc test was used for analyzing the interaction of age and brain region or age and genotype. In all tests a p value of < 0.05 was considered as significant. Statistical analyses were done using GraphPad Prism (GraphPad Software, Inc.). The type of statistical test and the exact p value for each experiment are included in the figure legends. All cell culture experiments using cell lines and primary cells were done at least

three times independently to ensure reproducibility. Technical and biological replicates were included. The average of at least 3 technical replicates was counted as one biological replicate which was then used for statistical analysis and comparison within the biological replicates. For all mouse experiments, 4 to 5 mice per genotype were analyzed. For histological analysis, 3 to 4 random region of interest (ROIs) per brain section were taken and three random brain sections per animal were quantified to account for variability within the biological sample. All values obtained from *in vivo* experiments were represented as mean ± sd of 3 brain sections per mouse for immunohistochemistry and 2 brain sections per mouse for RNAScope *in situ* hybridization. The values from *in vitro* experiments were reported as mean ± sd of the number of independent experiments. No power analyses were used to predetermine sample sizes. However, sample sizes were chosen based on prior literature using similar experimental paradigms. The value of n per group and what n represents in each experiment can be found in the figure legends. All data acquisition and analysis for wild-type and knockout samples were done in a blinded manner and no data were excluded from any analysis. For the scRNA-seq statistical data analysis, the n represents a sequencing lane, containing then a defined tissue (GM or WM) for a defined mouse (SS2) or a pool of mice (Drop-seq). Differential expression analysis was performed with DESeq2 (Love et al., 2014) and MAST (Finak et al., 2015) with adjusted p value below 0.05 considered as significant. For pathway enrichment analysis, Metascape (Zhou et al., 2019) and STRING (Szklarczyk et al., 2019) were used with default parameters.

4

CD8+ T CELLS INDUCE INTERFERON-RESPONSIVE OLIGODENDROCYTES AND MICROGLIA IN WHITE MATTER AGING

This article was published in Nature Neuroscience on 24 October, 2022.

In this article, we continued the study of white-matter aging, especially we wanted to adress the white-matter loss observed in aging for which mechanisms were still unknown. We focused mainly on oligodendrocytes which generate the myelin that wraps around axons. We used two methods of single-cell transcriptomics that converged to the same result. We identified a population of oligodendrocytes that presented genes typical of a response to interferon (IFN). We named this population IFN-responsive oligodendrocytes (IRO). We then demonstrated that they are localised in proximity to CD8 T cells. We further tested the hypothesis that IRO were induced by T cells by using three methods. First, a Rag1-KO aged mouse line was used, affecting all lymphocytes (CD4 and CD8 T cells, B cells). We saw a reduction of the amount of IRO and a rescue of the oligodendrocyte loss. Second, a treatment with checkpoint inhibitors increased the number of CD8 T cells present in the white-matter while the number of oligodendrocytes increased. Finally, using mouse line with non-functional CD8 T cells reduced the oligodendrocyte response to interferon and increased their number, thereby demonstrating the role of CD8 T cells in inducing an interferon response and loss of white-matter volume. We then focused on microglia, and identified a population that was also responsive to interferon, that we called IRM. These IRM were also present in proximity of CD8 T cells and gene enrichment analysis were significant for antigen presentation and upregulation of T-cell-mediated toxicity pathways. Altogether, this study provided evidence that CD8 T cells induce an interferon response in microglia and oligodendrocytes that contributes to white-matter loss in aging.

Individual contributions: M. Simons and O.G. conceived and supervised the project. T.K., N.M., L.L., **S.B.-G.**, H.J., S.K., O.G., J.W., L.C. and M. Schifferer performed experiments and analyzed the data. M. Simons and O.G. analyzed the data or supervised data acquisition. A.L. and J.G. provided essential reagents. M. Simons and O.G. wrote the manuscript with input from all authors.

In more details, I developped and maintained the infrastructure (storage and process) necessary for the laboratory to generate the single-cell and computational data. I established and optimised the single-cell library generation pipeline and the bionformatics data analysis pipeline that were used to generate the single-cell data in this publication. For the library generation, I contributed to the development of our protocol that includes actinomycin-D to prevent handling artefacts during the library generation. I performed the oligodendrocytes transcriptomics library processing and analysis. I provided continuous assistance to writing the manuscript.

nature neuroscience

Article

https://doi.org/10.1038/s41593-022-01183-6

CD8$^+$ T cells induce interferon-responsive oligodendrocytes and microglia in white matter aging

Received: 8 November 2021

Accepted: 14 September 2022

Published online: 24 October 2022

Check for updates

Tuğberk Kaya[1,2,3,4,7], Nicola Mattugini[2,3,7], Lu Liu[1,7], Hao Ji[1], Ludovico Cantuti-Castelvetri[2,3], Jianping Wu[2,3,4], Martina Schifferer[3,5], Janos Groh[6], Rudolf Martini[6], Simon Besson-Girard[1,4], Seiji Kaji[2,3], Arthur Liesz[1], Ozgun Gokce[1,5,8] ✉ and Mikael Simons[1,2,3,5,8] ✉

A hallmark of nervous system aging is a decline of white matter volume and function, but the underlying mechanisms leading to white matter pathology are unknown. In the present study, we found age-related alterations of oligodendrocyte cell state with a reduction in total oligodendrocyte density in aging murine white matter. Using single-cell RNA-sequencing, we identified interferon (IFN)-responsive oligodendrocytes, which localize in proximity to CD8$^+$ T cells in aging white matter. Absence of functional lymphocytes decreased the number of IFN-responsive oligodendrocytes and rescued oligodendrocyte loss, whereas T-cell checkpoint inhibition worsened the aging response. In addition, we identified a subpopulation of lymphocyte-dependent, IFN-responsive microglia in the vicinity of the CD8$^+$ T cells in aging white matter. In summary, we provide evidence that CD8$^+$ T-cell-induced, IFN-responsive oligodendrocytes and microglia are important modifiers of white matter aging.

Age is the major risk factor for the most prevalent neurodegenerative diseases[1]. A better understanding of age-related alterations is therefore of overarching importance, but relatively little is known about the pathology occurring in the white matter, which is to a large extent composed of myelin, a lipid-rich membrane wrapped around axons by oligodendrocytes[2]. Myelination is not limited to early development but extends into adult life and contributes to brain plasticity. Regulated by neuronal stimuli and various environmental factors, there is a substantial fraction of adult-born oligodendrocytes that is actively engaged in forming new myelin sheaths, a process that declines in aging[3–5]. In humans, white matter volume starts to decline already in mid-life and these global alterations are often associated with focal lesions that appear hyperintense on magnetic resonance images[6–9]. Focal white matter degeneration is related to an increased risk of stroke and dementia[6] and contributes to cognitive decline possibly by disrupting connective pathways in the brain[10–12]. In nonhuman primates and rodents, ultrastructural analyses of aging white matter show pathology of myelinated fibers, consisting of focal areas of degenerated myelin and axonal damage[13,14]. We have previously shown that such age-related myelin pathology results in a distinct white matter-associated microglia state, in which the disease-associated microglia (DAM) or microglia-neurodegenerative phenotype (MGnD) program is partially activated to clear myelin debris in groups of a few closely connected microglia[15–18]. Whereas the microglial responses to

[1]Institute for Stroke and Dementia Research, University Hospital of Munich, Ludwig Maximilian University (LMU) of Munich, Munich, Germany. [2]Institute of Neuronal Cell Biology, Technical University Munich, Munich, Germany. [3]German Center for Neurodegenerative Diseases, Munich, Germany. [4]Graduate School of Systemic Neurosciences, LMU Munich, Munich, Germany. [5]Munich Cluster of Systems Neurology, Munich, Germany. [6]Department of Neurology, Section of Developmental Neurobiology, University Hospital Würzburg, Würzburg, Germany. [7]These authors contributed equally: Tuğberk Kaya, Nicola Mattugini, Lu Liu. [8]These authors jointly supervised this work: Ozgun Gokce, Mikael Simons. ✉e-mail: oezguen.goekce@med.uni-muenchen.de; mikael.simons@dzne.de

aging and disease are more intensely studied[15,17,19–21], less is known about aging-related oligodendrocyte reactions related to myelin pathology. In the present study, we studied aging-induced glial reactivity and identified IFN-responsive oligodendrocyte and microglia in the white matter. We observed that CD8$^+$ T cells increase in aging white matter and localize in close proximity to IFN-responsive cells. Genetic ablation of functional lymphocytes by using *Rag1*$^{-/-}$ mice[22] or *CD8*$^{-/-}$ mice[23] prevented aging-induced oligodendrocyte loss and IFN-responsive oligodendrocyte and microglia formation. Inversely, T-cell-checkpoint inhibition worsened the aging effect. These perturbation experiments support a role of CD8$^+$ T cells in driving white matter aging.

Results

Transcriptomic aging responses of oligodendrocytes

To characterize the oligodendrocyte aging effect at single-cell resolution, we used two different single-cell RNA-sequencing (scRNA-seq) methods. For plate-based scRNA-seq (Smart-seq2), we dissociated gray matter from the frontal cortex and white matter tracts from the corpus callosum as well as the optical tracts, and the medial lemniscus from young (3-month-old) and aged (24-month-old), wild-type male mice (Fig. 1a). The scRNA-seq experimental details and animal information are reported according to guidelines[24,25] (Methods and Supplementary Tables 1 and 2). To avoid isolation artifacts, we used our previously established automated dissociation protocol that inhibits ex vivo transcription[18]. We sorted live nonmyeloid (CD11b$^-$ and SYTOX BLUE$^-$) cells (Extended Data Fig. 1a). Each single-cell library passed through strict quality thresholds filtering out 112 single cells due to low quality and 2,538 single cells from 8 mice remained (Extended Data Fig. 1b). The cell-type composition of these cells was analyzed by unsupervised Uniform Manifold Approximation and Projection (UMAP) analysis (Fig. 1b, Extended Data Fig. 1c,d and Supplementary Table 1). Oligodendrocytes were separated into four different subclusters, of which the most abundant two clusters represent the heterogeneity of oligodendrocytes previously identified in juvenile and adult mouse by Marques et al.[26]. In our analysis, two additional oligodendrocyte clusters appeared in aged mice, which were enriched in white matter. One was characterized by a high expression of the serine (or cysteine) peptidase inhibitor, member 3N (Serpina3n) and the complement component C4b, previously associated with injury responses[27–32]. As this cluster was highly enriched in the aged white matter, we named it aging-related oligodendrocytes (Fig. 1b,c,e). We uncovered a smaller IFN-responsive oligodendrocyte subpopulation (IRO), which was characterized by the expression of genes commonly associated with an IFN response, such as *Stat1*, *Ifi27l2a* and major histocompatibility complex (MHC) class I-related genes (*H2-K1 and H2-D1)* (Fig. 1b,c,f). A related gene expression profile has been detected in oligodendrocyte progenitor cells (OPCs) in the context of multiple sclerosis[28,30]. To validate our results, we performed scRNA-seq using the 10× platform with cells from gray and white matter of 24-month-old mice (8,726 high-quality cells from 8 mice: Fig. 1b and Extended Data Fig. 1e). Tissues were prepared as described for Smart-seq2 and enriched for live cells using flow cytometry (Extended Data Fig. 1a). Major cell types were annotated based on canonical markers upon clustering (Extended Data Fig. 1e–g). We again identified a continuous range of oligodendrocytes that reproduced the major oligodendrocyte clusters of the Smart-seq2 scRNA-seq dataset (Fig. 1b,g). The higher number of oligodendrocytes allowed us to resolve Oligo1 and Oligo2 into five subclusters, but the identity and ratios of all four major clusters remained similar in both aged scRNA-seq datasets (Fig. 1g,h and Extended Data Fig. 1h). Using 20 independent scRNA-seq experiments, we compared changes in ratios of IROs and age-related oligodendrocytes by using the single-cell differential composition analysis (scCODA), which takes account of the compositionality of the scRNA-seq data and reliably controls for false discoveries[33]. Both age-related oligodendrocyte and IRO cluster proportions were significantly increased in the aged white matter samples (Fig. 1e,f). These increases were accompanied by a significant decrease in aged white matter Oligo1 but not in Oligo2 (Extended Data Fig. 2a).

CD8$^+$ T cells induce reactivity and loss of oligodendrocytes

To validate the changes in scRNA-seq cluster ratios and to determine the localization of the age-related and the IFN-responsive oligodendrocytes, we costained anti-adenomatous polyposis coli (APC) clone CC1 (CC1$^+$) oligodendrocytes by using antibodies against C4b, Serpina3n, B2M and STAT1. Consistent with the scRNA-seq data, we found that antibodies against C4b, Serpina3n, B2M and STAT1 labeled oligodendrocytes in the white matter, and only rarely in the gray matter (cortical areas of the brain) of aged (24-month-old) mice (Fig. 2a and Extended Data Fig. 2b,c). Colabeling against STAT1 and Serpina3n did not detect double-positive cells, in agreement with our scRNA-seq data that STAT1$^+$ oligodendrocytes are distinct from Serpina3n$^+$ oligodendrocytes (Extended Data Fig. 2e). Next, we compared the labeling in young (3-month) and old (24-month) gray and white matter and found that CC1$^+$ oligodendrocytes, also immunoreactive for C4b, Serpina3n, STAT1 or B2M, are restricted to the aged brains mostly in the white matter (Fig. 2a and Extended Data Fig. 2b,c). Quantification revealed that about 3–5% of the CC1$^+$ cells within the corpus callosum of 24-month-old mice were positive for the markers STAT1 and B2M. We found that C4b$^+$/Serpina3n$^+$ oligodendrocytes were more abundant (41% of CC1$^+$ cells were Serpina3n$^+$/CC1$^+$ and 30% C4b$^+$/CC1$^+$ in 24-month-old white matter) and also more evenly distributed compared with B2M$^+$/STAT1$^+$ oligodendrocytes (Fig. 2a and Extended Data Fig. 2d,f). Our subregional localization analysis revealed that STAT1$^+$ oligodendrocytes were localized significantly closer to the medial white matter bordering the lateral ventricles compared with the frontal white matter (Extended Data Fig. 3a,b). Previous work has identified infiltrating T cells in the aged brain, close to neurogenic niches and within the optic nerve[34,35]. As T cells are a major source of IFNs, we analyzed T-cell proportions in the mouse aging single-cell transcriptomic atlas[35] and found that the T cells significantly increased in 24-month-old mice compared with 18- and 3-month-old mice (Extended Data Fig. 3f). Using immunohistochemistry, we analyzed the CD3$^+$ T cells in the white and gray matter of the aged brain and observed that the T cells, which were mostly CD8$^+$ T cells, were almost exclusively found in the white matter, where they were enriched in areas close to the lateral ventricles (Fig. 2b and Extended Data Figs. 2d and 3a,b,d). Next, we studied the spatial relationship between the IFN-responsive oligodendrocytes (STAT1$^+$CC1$^+$) and CD8$^+$ T cells in aging white matter. Strikingly, STAT1$^+$CC1$^+$ cells are more frequently localized in close proximity to CD8$^+$ T and vice versa (<20 µm) (Fig. 2c). Moreover, STAT1$^+$CC1$^+$ oligodendrocytes are found significantly more often in close proximity to CD8$^+$ T cells than randomly chosen DAPI$^+$ cells (Fig. 2d), which was not the case for Serpin3n$^+$CC1$^+$ oligodendrocytes (Extended Data Fig. 3e).

To characterize the CD8$^+$ T cells in the aging brain, we analyzed the mouse aging single-cell transcriptomic atlas[36] and the CD8$^+$ T-cell dataset from Groh et al.[34]. Our analysis, which included samples from 4 different organs of 21- and 24-month-old mice, showed that brain-associated CD8$^+$ T cells segregated away from CD8$^+$ T cells from the spleen, kidney and lung in the UMAP presentation (Extended Data Fig. 4a). Genes differentially upregulated in the brain CD8$^+$ T cells were enriched in tissue-resident memory T-cell markers (*Cxcr6*, *Cd69*, *Junb*, *Bhlhe40*), checkpoint molecules (*Pdcd1*) and effector function-associated genes (*Gzmb*, *Ccl4*, *Ccl5*, *Ifng*), but low in genes associated with central memory T cells (*Sell*, *Ccr7*) compared with CD8$^+$ T cells from the spleen, kidney and lung (Extended Data Fig. 4a–d).

Next, we performed immunofluorescence staining for the tissue-resident memory T-cell marker, CD69, which showed that almost all the CD8$^+$ T cells were also positive for CD69 (Extended Data Fig. 5a). We analyzed the expression of the checkpoint molecules, programmed cell death protein 1 (PD-1) and the lymphocyte-activation

https://doi.org/10.1038/s41593-022-01183-6

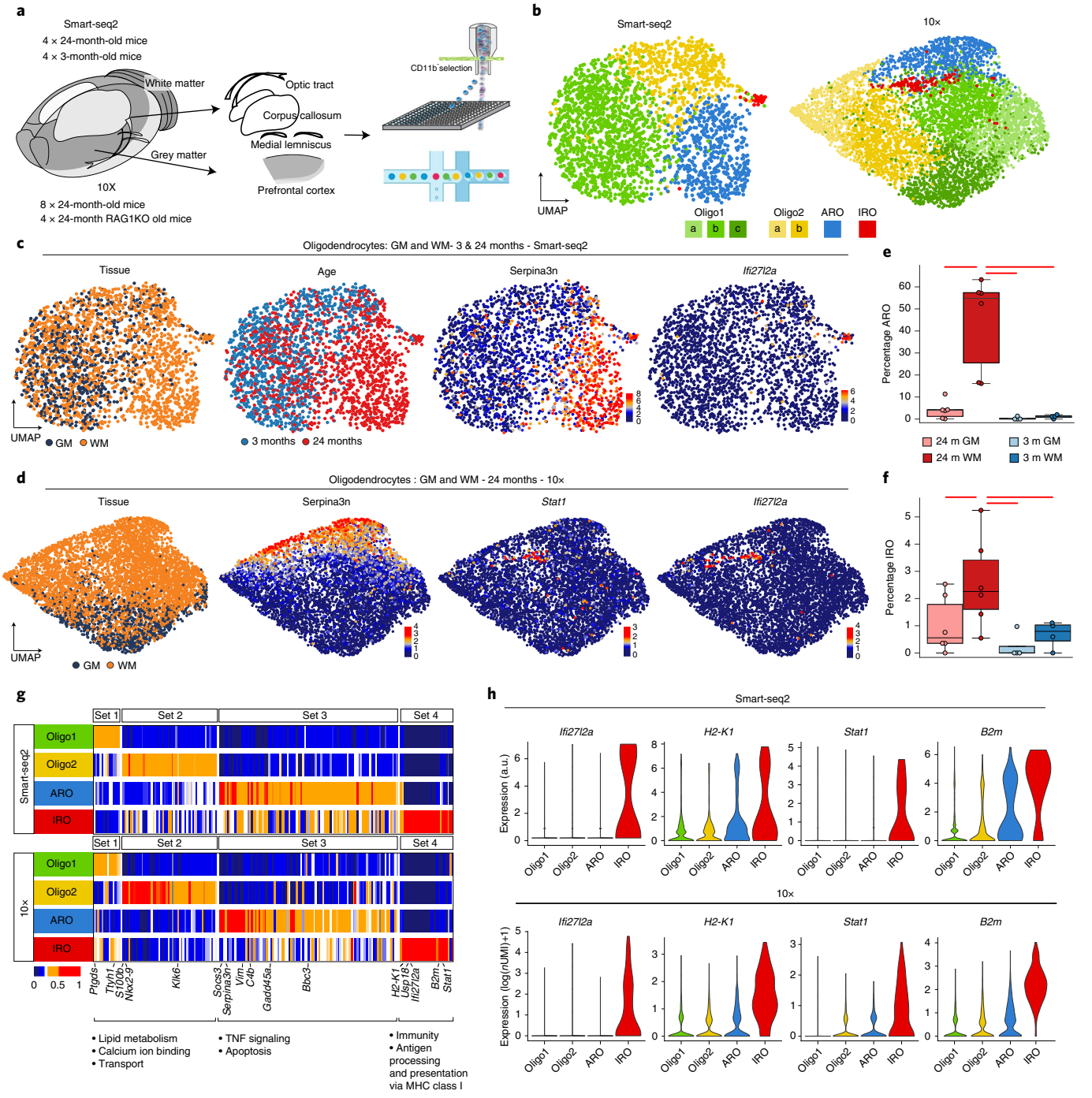

Fig. 1 | Identification of age-related gene expression signatures in oligodendrocytes. a, Experimental design from dissection to cell sorting and cell loading for the plate-based (Smart-seq2 (SS2)) and 10× pipelines, respectively. **b**, UMAP plots of oligodendrocytes in the SS2 and 10× datasets, colored by identified populations. **c**, UMAP plots of oligodendrocytes in the SS2 dataset, colored by tissue, age and expression of selected marker genes. **d**, The 10× dataset oligodendrocyte UMAP plots colored by tissue and expression of selected marker genes. **e**–**f**, Boxplots of the age-related oligodendrocytes (ARO) (**e**) and interferon-responsive oligodendrocytes (IRO) (**f**) cluster proportions per sample, respectively. The central line denotes the median, boxes represent the IQR and whiskers show the distribution except for outliers. Outliers are all points outside 1.5× the IQR. Each dot represents a sample ($n = 20$ independent experiments) and significant results (scCODA model) are indicated with red bars. 24 m, 24-month-old; 3 m, 3-month-old. **g**, Heatmaps of average expression of differentially expressed genes, comparing the four oligodendrocyte populations. Gene sets were identified as differentially expressed markers for each population using the SS2 dataset. Values are normalized per gene, showing the gene expression across populations. Each column represents a gene. GO terms are shown below each set of genes (Supplementary Table 3). TNF, tumor necrosis factor. **h**, Violin plots showing selected IRO-enriched marker genes across SS2 and 10× datasets. a.u., arbitrary units representing the corrected log(1*P*) (counts) value.

gene 3 (*LAG-3*) and found that 40% of $CD8^+$ T cells were immunolabeled by antibodies against PD-1 and 32% of $CD8^+$ T cells by antibodies against *LAG-3* (Extended Data Fig. 5b,c).

As checkpoint molecules are known to control the function of T cells, we treated 18-month-old mice with antibodies against the coinhibitory receptors such as cytotoxic T-lymphocyte-associated protein

https://doi.org/10.1038/s41593-022-01183-6

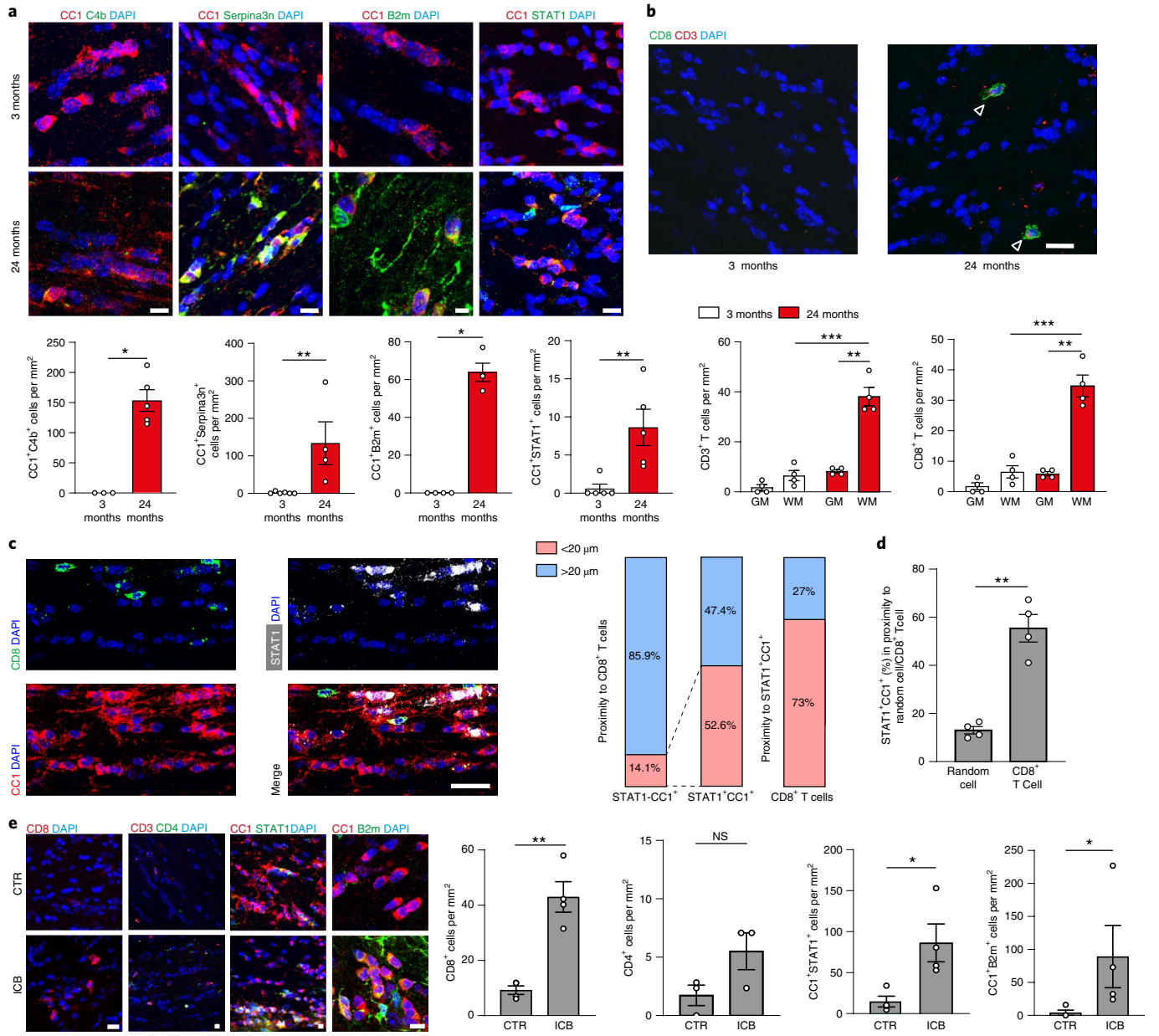

Fig. 2 | IFN-responsive oligodendrocytes localize to aged white matter close to CD8$^+$ T cells. a, Immunofluorescence staining and quantification of C4b, Serpina3n, B2m and STAT1 in CC1$^+$ oligodendrocytes in the white matter of 3- and 24-month-old mice (C4b$^+$CC1$^+$, 3-month, $n = 3$, 24-month, $n = 5$, $^*P = 0.0357$; Serpina3n$^+$CC1$^+$, 3-month, $n = 6$, 24-month, $n = 4$, $^{**}P = 0.0095$; B2m$^+$CC1$^+$, 3-month, $n = 4$, 24-month, $n = 4$, $^*P = 0.0286$; STAT1$^+$CC1$^+$, 3-month, $n = 5$, 24-month, $n = 5$, $^{**}P = 0.0079$; data are mean ± s.e.m.; *P* values are from a two-tailed Mann–Whitney *U*-test). Scale bar, 20 µm; for B2m, 10 µm. **b**, Immunofluorescence showing CD3$^+$CD8$^+$ T cells (indicated by arrowheads). Scale bar, 20 µm. Quantification of CD3$^+$ T cells and CD8$^+$ T cells in the gray (GM) and white (WM) matter of 3- and 24-month-old mice ($n = 4$ mice per group, 3-month WM versus 24-month WM, CD3$^+$, $^{***}P = 0.0003$, CD8$^+$, $^{***}P = 0.0005$; 24-month GM versus 24-month WM, CD3$^+$, $^{**}P = 0.0050$, CD8$^+$, $^{**}P = 0.0032$; data are mean ± s.e.m.; *P* values represent a two-sided Student's *t*-test). **c**, Immunofluorescence of CD8$^+$ T cells and STAT1$^+$CC1$^+$ oligodendrocytes in proximity in the white matter of 24-month-old mice. Scale bars, 20 µm. Bar plots show quantification of STAT1$^+$ and STAT1$^-$CC1$^+$ proximity to CD8$^+$ T cells and vice versa (3 sections per mouse were selected; a total of 134 CD8$^+$ T cells and 272 STAT1$^+$CC1$^+$ oligodendrocytes from 4 mice were analyzed). **d**, Quantification of the percentage of STAT1$^+$CC1$^+$ oligodendrocytes found in proximity to random cells compared with CD8$^+$ T cells ($n = 4$ mice per group, $^{**}P = 0.0052$; data are mean ± s.e.m; *P* value represents a two-sided paried Student's *t*-test). **e**, Immunofluorescence staining and quantification of CD8$^+$ T cells, CD4$^+$ T cells, B2m$^+$ and STAT1$^+$CC1$^+$ oligodendrocytes in the white matter of mice treated with anti-PD-1 and CTLA-4 (ICB) and isotype control antibodies (CTR) for 6 weeks starting at an age of 18 months (CD8$^+$, $n = 4$, $^{**}P = 0.0011$; CD4$^+$, $n = 3$; STAT1$^+$CC1$^+$, $n = 4$, $^*P = 0.0244$; B2m$^+$CC1$^+$, $n = 4$, $^*P = 0.0286$; data are mean ± s.e.m.; *P* values represent a two-sided Student's *t*-test (CD8$^+$, STAT1$^+$CC1$^+$) or two-tailed Mann–Whitney *U*-test (CD4$^+$, B2m$^+$CC1$^+$)). Scale bar, 20 µm. NS, not significant.

4 (CTLA-4) and PD-1 to determine the effect on oligodendrocytes. Immune checkpoint blockage therapy is used to dampen coinhibitory molecules to achieve robust anti-tumor immune response[37]. Treatment of mice with twice-weekly intraperitoneal injections with anti-PD-1 and anti-CTLA-4 antibodies for 6 weeks resulted in an increased number of CD8$^+$ T cells, but not CD4$^+$ T cells, in the white matter (Fig. 2e). In addition, the number of STAT1$^+$CC1$^+$ and B2M$^+$CC1$^+$ oligodendrocytes increased within the corpus callosum by checkpoint blockage

therapy (Fig. 2e). The formation of Serpina3n$^+$ oligodendrocytes was not induced by anti-PD-1/anti-CTLA-4 antibody treatment (Extended Data Fig. 6c).

To continue exploring the link between T cells and white matter aging, we performed three independent scRNA-seq experiments using the 10× platform on 24-month-old *Rag1*$^{-/-}$ mice, which lack functional lymphocytes. The *Rag1*$^{-/-}$ dataset integrated well with our 24-month-old wild-type 10× datasets, showing good batch mixing while still preserving biological variance (Fig. 3a and Extended Data Fig. 6a–c). The unsupervised clustering of T/natural killer (NK) cells showed that the number of *Cd3d*- and *Trbc2*-expressing T cells are significantly higher in the white matter of aged wild-type mice (Fig. 3b,c and Extended Data Fig. 6d). Unsupervised clustering of oligodendrocytes from the combined datasets showed again the same transcriptional clusters with *Stat1* and *H2-D1* expressing IROs and Serpina3n expressing age-related oligodendrocytes (Fig. 3d). The scCODA analysis showed a marked reduction of IROs in *Rag1*$^{-/-}$ mice (Fig. 3e). This finding was consistent with our immunolabeling experiments, which showed a reduction of IROs in *Rag1*$^{-/-}$ mice (Fig. 3f). Together, these data provide evidence that the adaptive immune system promotes IFN responses in oligodendrocytes in the aging white matter, but to what extent these changes contribute to white matter degeneration is unclear.

Next, we used correlated light and electron microscopy to detect areas of high IBA1$^+$ cell density by immunohistochemistry, followed by scanning electron microscopy to determine the ultrastructure of myelinated axons. This analysis uncovered focal areas of hypomyelination in the corpus callosum of 24-month-old mice close to the ventricular area (Extended Data Fig. 6e). To quantify the age-related decay, we determined the number of oligodendrocytes in the aging brain. First, we analyzed oligodendrocyte proportions by using the mouse aging single-cell transcriptomic atlas[36] and found that the oligodendrocyte significantly decreased in 24-month-old compared with 18- and 3-month-old mice (Extended Data Fig. 7d). Next, we used immunohistochemistry to quantify oligodendrocyte cell numbers in 12-, 18- and 24-month-old mice (Fig. 3g). We observed that the density of CC1$^+$ oligodendrocytes declined in the 24-month-old compared with the 12-month-old white matter, whereas no changes were observed in the aged gray matter (Fig. 3g). Similar results were obtained when glutathione *S*-transferase (GST-π) was used as an additional marker to stain for mature oligodendrocytes (Extended Data Fig. 7a,b). In addition, there was a decrease in Olig2$^+$ oligodendroglial cells, but not of Pdgfra$^+$ OPCs (Extended Data Fig. 7c). Next, we analyzed oligodendrocytes in *Rag1*$^{-/-}$ mice and found no differences in oligodendrocyte density compared with controls at 6 months in both gray and white matter (Extended Data Fig. 7e,f). However, when 24-month-old mice were analyzed, we detected a higher density of oligodendrocytes in the white matter of 24-month-old *Rag1*$^{-/-}$ compared with wild-type control mice (Fig. 3g).

As *Rag1*$^{-/-}$ mice lack various populations of mature adaptive immune cells, including CD4, CD8, gamma–delta and B cells, we used mice homozygous for the Cd8a^{tm1Mak}-targeted mutation (CD8$^{-/-}$) that specifically lacks functional CD8$^+$ T cells[23]. When we analyzed 24-month-old CD8$^{-/-}$ mice, we found a reduction of the number of STAT1$^+$CC1$^+$ oligodendrocytes compared with control wild-type mice (Fig. 3h). Next, we determined the density of CC1$^+$ oligodendrocytes and detected higher numbers of oligodendrocytes in 24-month-old CD8$^{-/-}$ mice compared with controls (Fig. 3i), confirming that CD8$^+$ T cells induce IFN responses and loss of oligodendrocytes.

CD8$^+$ T cells induce IFN-responsive microglia

As previous studies have identified IFN-responsive microglia in various models of neurodegenerative disease and during aging[15], we asked whether the adaptive immune system mediates IFN-responsive microglia conversion. Unsupervised clustering of 15,601 microglia from the aged white and gray matter of *Rag1*$^{-/-}$ and wild-type mice revealed distinct populations, including previously described homeostatic microglia, activated microglia, white matter-associated microglia and, in addition, a smaller population of IFN-responsive microglia (Fig. 4a). The IFN-responsive microglia subset was significantly enriched in aged white compared with gray matter and was reduced in aged *Rag1*$^{-/-}$ mice (Fig. 4a,b). INF-responsive microglia are characterized by the upregulation of IFN-stimulated genes *Stat1* and *Ifit3* (Fig. 4c,d). Gene ontology (GO) enrichment analysis showed that IFN-responsive microglia and oligodendrocytes share a transcriptional signature of IFN-induced genes including *Stat1*, *Ifit3*, *Usp18* and *Ifit27l2a* (Fig. 4e). GO enrichment analysis also detected differences with upregulated genes involved in antigen processing and positive regulation of T-cell-mediated cytotoxicity for IFN-responsive oligodendrocytes, lymphocyte chemotaxis and immune responses for IFN-responsive microglia.

To validate the presence of IFN-responsive microglia in the aged white matter, we costained IBA1$^+$ microglia by using antibodies against STAT1 and, in agreement with our scRNA-seq data, we detected STAT1$^+$IBA1$^+$ microglia in the white matter of 24-month-old mice (Fig. 4f). Notably, these cells were almost absent from the white matter of 3-month-old mice. Next, we studied the spatial relationship between STAT1$^+$IBA1$^+$ microglia and CD8$^+$ T cells in aging white matter and found that they were frequently in close proximity (<20 µm) (Fig. 5a). Our analysis showed that STAT1$^+$IBA1$^+$ microglia are significantly more often found in close proximity to CD8$^+$ T cells than randomly chosen DAPI$^+$ cells (Fig. 5b). To determine whether the formation of STAT1$^+$IBA1$^+$ microglia depends on the function of adaptive immune cells, we first analyzed the effect of the treatment of 18-month-old mice with antibodies against the coinhibitory receptors CTLA-4 and PD-1. The number of STAT1$^+$IBA1$^+$ microglia increased within the corpus callosum by checkpoint blockage therapy (Fig. 5c). Next, we analyzed the number of STAT1$^+$IBA1$^+$ microglia in the white matter of 24-month-old *Rag1*$^{-/-}$ mice, which revealed a reduction of STAT1$^+$IBA1$^+$

Fig. 3 | Absence of functional lymphocytes reduces IFN-responsive oligodendrocyte numbers and increases oligodendrocyte cell density in the aged white matter. a, UMAP plot of 44,983 single-cell transcriptomes, colored by major cell types. **b**, UMAP of T cells and NK cells, colored by T-cell identity, genotype and T-cell marker genes. **c**, Bar plot showing the relative distribution of each genotype-tissue experimental group within the T/NK cell population. **d**, UMAP plots of oligodendrocytes in the *Rag1*$^{-/-}$ and wild-type integrated dataset, colored by identified clusters, genotype and tissue annotation, as well as selected marker genes. **e**, Boxplot of the IRO cluster proportion per sample. The central line denotes the median, boxes represent the IQR and whiskers show the distribution except for outliers. Outliers are all points outside 1.5× the IQR. Each dot represents a sample ($n = 8$ independent experiments) and significant results (scCODA model) are indicated with red bars. **f**, Immunofluorescence staining and quantification of STAT1$^+$CC1$^+$ oligodendrocytes in the white matter of 24-month-old wild-type and 24-month-old *Rag1*$^{-/-}$ mice ($n = 5$ mice per group, $^*P = 0.0466$; data are mean ± s.e.m.; *P* values represent a two-sided Student's *t*-test). Scale bar, 20 µm. **g**, Immunofluorescence staining and quantification of CC1$^+$ oligodendrocyte density in the gray (GM) and white matter (WM) of 12-, 18- and 24-month-old wild-type and *Rag1*$^{-/-}$ mice (GM, $n = 3, 3, 5, 4$; WM, $n = 3, 3, 5, 4$; 12 months versus 24 months, $^*P = 0.0185$, 24-month versus 24-month *Rag1*$^{-/-}$, $^{**}P = 0.0083$; data are mean ± s.e.m.; *P* values represent two-sided, one-way ANOVA with post hoc Tukey's test). Scale bar, 20 µm. **h**, Immunofluorescence staining and quantification of CC1$^+$STAT1$^+$ oligodendrocytes in the white matter of 24-month-old wild-type and *CD8*$^{-/-}$ mice ($n = 4$ mice per group, $^{**}P = 0.0035$; data are mean ± s.e.m.; *P* value represents a two-sided Student's *t*-test). Scale bar, 20 µm. **i**, Immunofluorescence staining and quantification of CC1$^+$ oligodendrocyte density (red) in the white matter of 24-month-old wild-type and CD8$^{-/-}$ mice ($n = 4$ mice per group, $^*P = 0.0176$; data are mean ± s.e.m.; *P* value represents a two-sided Student's *t*-test). Scale bar, 20 µm.

https://doi.org/10.1038/s41593-022-01183-6

microglia number compared with control wild-type mice (Fig. 4f). Finally, we stained for STAT1^{+}IBA1^{+} microglia in aged CD8$^{-/-}$ mice. Again, 24-month-old mice deficient in functional CD8^{+} T cells had markedly lower numbers of STAT1^{+}IBA1^{+} microglia compared with control wild-type mice (Fig. 5d). Together, these data show that CD8^{+} T cells not only induce an IFN-responsive oligodendrocyte but also microglia state in the aged white matter.

As our previous work identified the age-dependent formation of white matter-associated microglia, engaged in clearing myelin debris[18], we asked whether these cells are required for lymphocyte-dependent

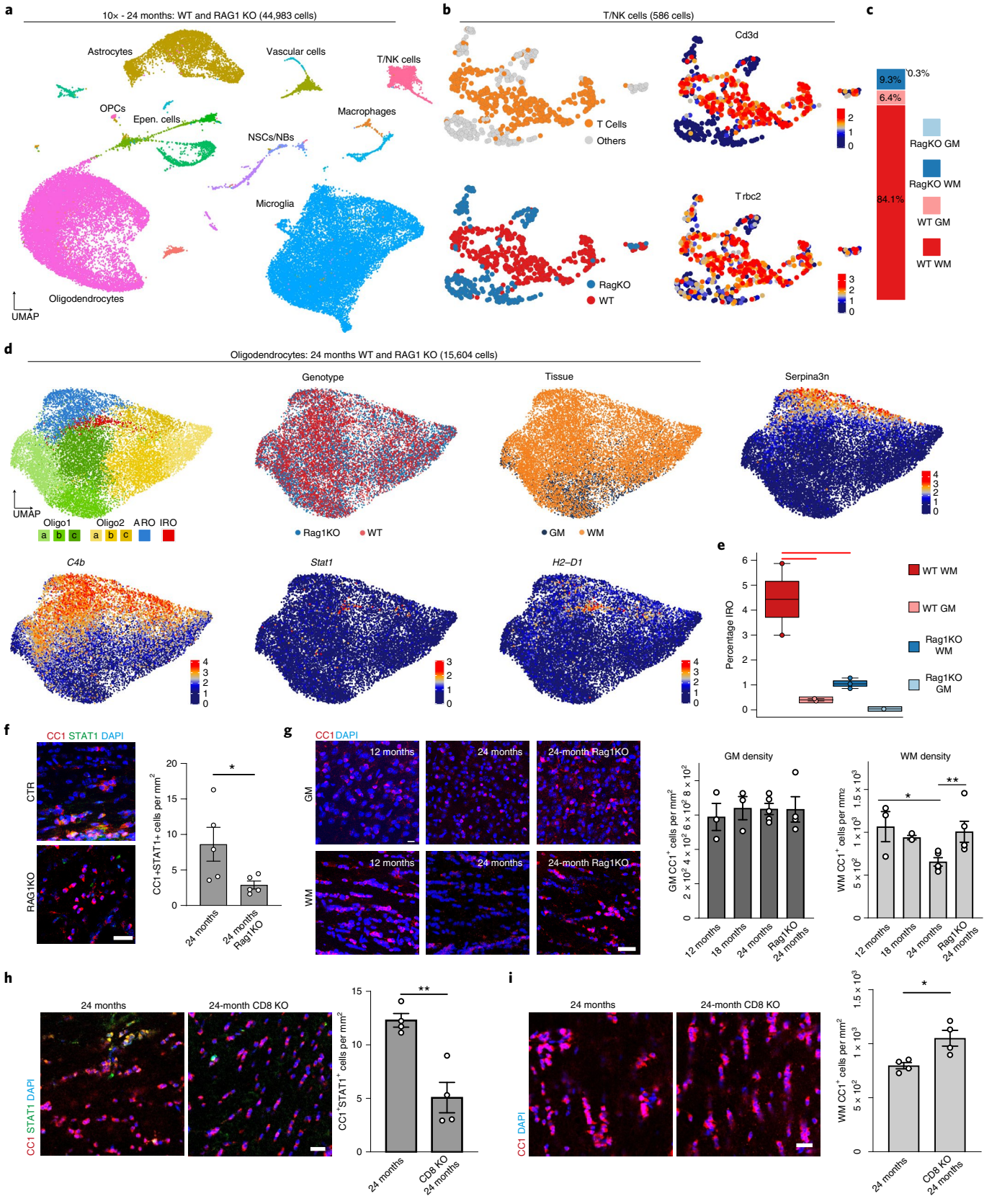

https://doi.org/10.1038/s41593-022-01183-6

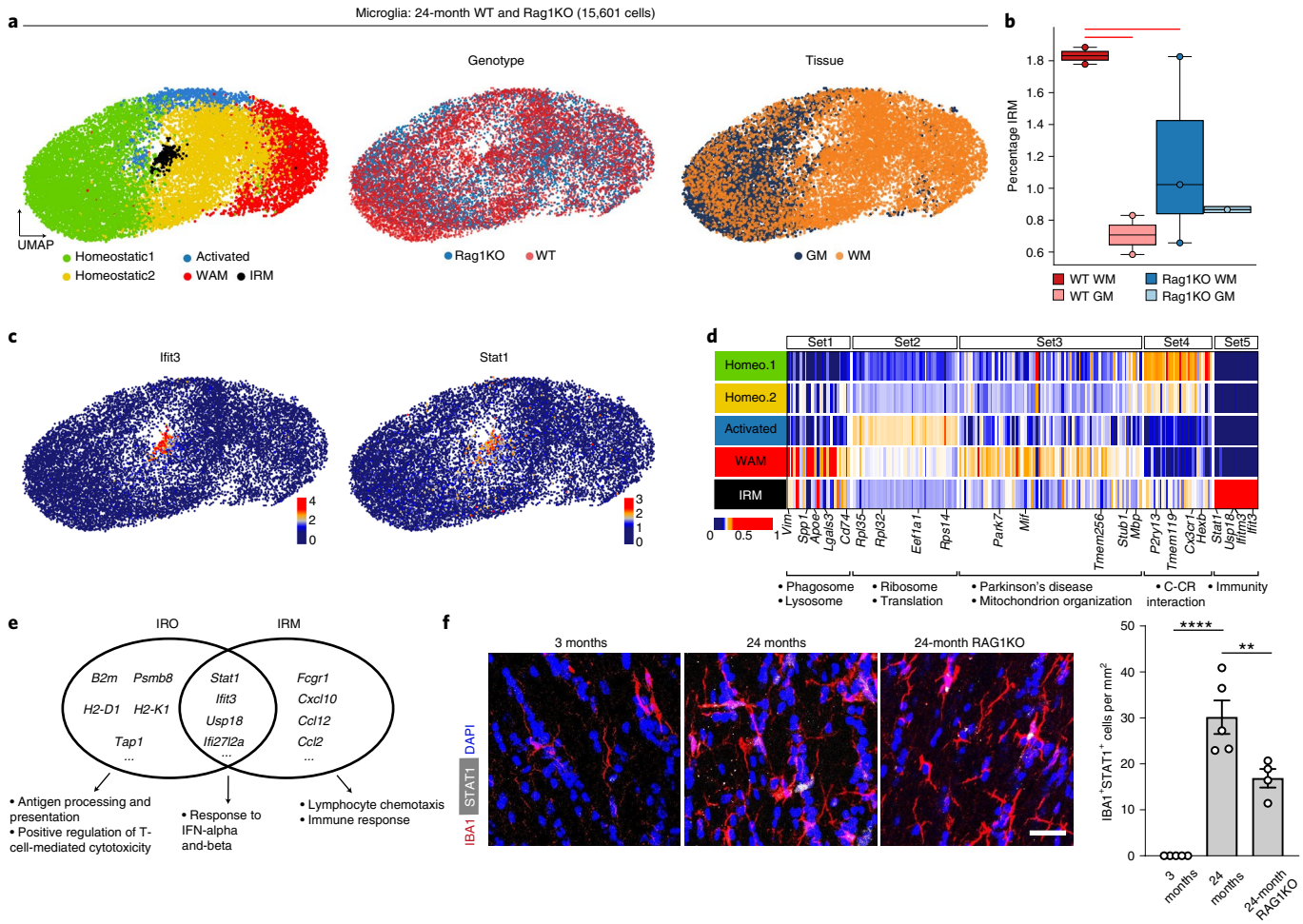

Fig. 4 | Identification of IFN-responsive microglia in aged white matter. a, UMAP plots of microglia colored by identified clusters, genotype and tissue annotation. **b**, Boxplot of the IRM cluster proportion per sample, respectively. WAM, White matter associated microglia; WT, Wild-type. The central line denotes the median, boxes represent the IQR and whiskers show the distribution except for outliers. Outliers are all points outside 1.5× the IQR. Each dot represents a sample ($n = 8$ independent experiments) and significant results (scCODA model) are indicated with red bars. **c**, UMAP plots of selected IRM marker genes. **d**, Heatmaps of average expression of differentially expressed genes, comparing the five microglia populations. Gene sets 1–4 were identified in Safaiyan et al.[18] and set 5 was identified by differential expression analysis of the IRM cluster. Values are normalized per gene, showing the gene expression across populations. Each column represents a gene. GO terms are shown below each set of genes. **e**, Venn diagram of top 50 differentially expressed genes of IRO and IRM clusters with an intersection set of 16 genes. Gene lists are found in Supplementary Table 3. **f**, Immunofluorescence staining and quantification of STAT1$^+$IBA1$^+$ microglia in the white matter of 3- and 24-month-old wild-type and 24-month-old *Rag1*$^{-/-}$ mice (IBA1$^+$STAT1$^+$, $n = 5,5,4$; 3 months versus 24 months, $^{***}P = 0.000002$; 24-month versus 24-month *Rag1*$^{-/-}$, $^{**}P = 0.0087$; data are mean ± s.e.m.; *P* value represents two-sided, one-way ANOVA with post hoc Tukey's test). Scale bar, 20 µm.

IFN responses in aged white matter. This seemed plausible because white matter-associated microglia are defined by the activation of genes implicated in phagocytic activity, antigen processing and presentation, and they also express MHC-I (Extended Data Fig. 8a,b) and are enriched in *Mbp* transcripts (Extended Data Fig. 8c,d), reminiscent of microglia containing myelin transcripts previously detected in the brains of patients with multiple sclerosis[38]. As the triggering receptor expressed on myeloid cell 2 (TREM2) is required for the formation of white matter-associated microglia[18], we analyzed *Trem2*$^{-/-}$ mice to determine possible differences in the formation of IFN-responsive oligodendrocytes and microglia.

However, when aged *Trem2*$^{-/-}$ mice were analyzed, we did not detect any significant differences in the number of STAT1$^+$CC1$^+$ oligodendrocytes or STAT1$^+$IBA1$^+$ microglia and also not in the proximity of STAT1$^+$IBA1$^+$ microglia to CD8$^+$ T cells, even if there was a lower number of CD8$^+$ T cells (Extended Data Fig. 8e–h), pointing to TREM2-independent mechanisms in the formation of IFN-responsive oligodendrocytes and microglia in aged white matter. However, aged *Trem2*$^{-/-}$ mice suffer from slightly degenerating white matter and seizures[18], which can cause innate immune reactions[39], making the interpretation of the data more difficult.

IFN-γ injection induces oligodendrocyte loss

Next, we performed experiments to determine the functional consequences of IFN on oligodendrocytes. Previous work has shown that CD8$^+$ cytotoxic T lymphocytes in the aged brain produce IFN-γ[35]. To assess the impact of IFN-γ on oligodendrocytes, we stereotactically injected 10 ng of IFN-γ into the white matter of 4- and 18-month-old mice, which was sufficient to induce STAT1$^+$CC1$^+$ oligodendrocytes (Extended Data Fig. 9a). Strikingly, when lesions were analyzed 48 h postinjection in 4- and 18-month-old mice, we found that the aged mice contained more MAC2$^+$ phagocytes loaded with myelin debris, displayed stronger reduction of CC1$^+$ oligodendrocytes and showed more pronounced demyelination with loss of myelin basic protein (MBP) and a reduction of neurofilament labeling (Fig. 6a–e and Extended Data Fig. 9c). Control vehicle injections in 18-month-old mice did not

https://doi.org/10.1038/s41593-022-01183-6

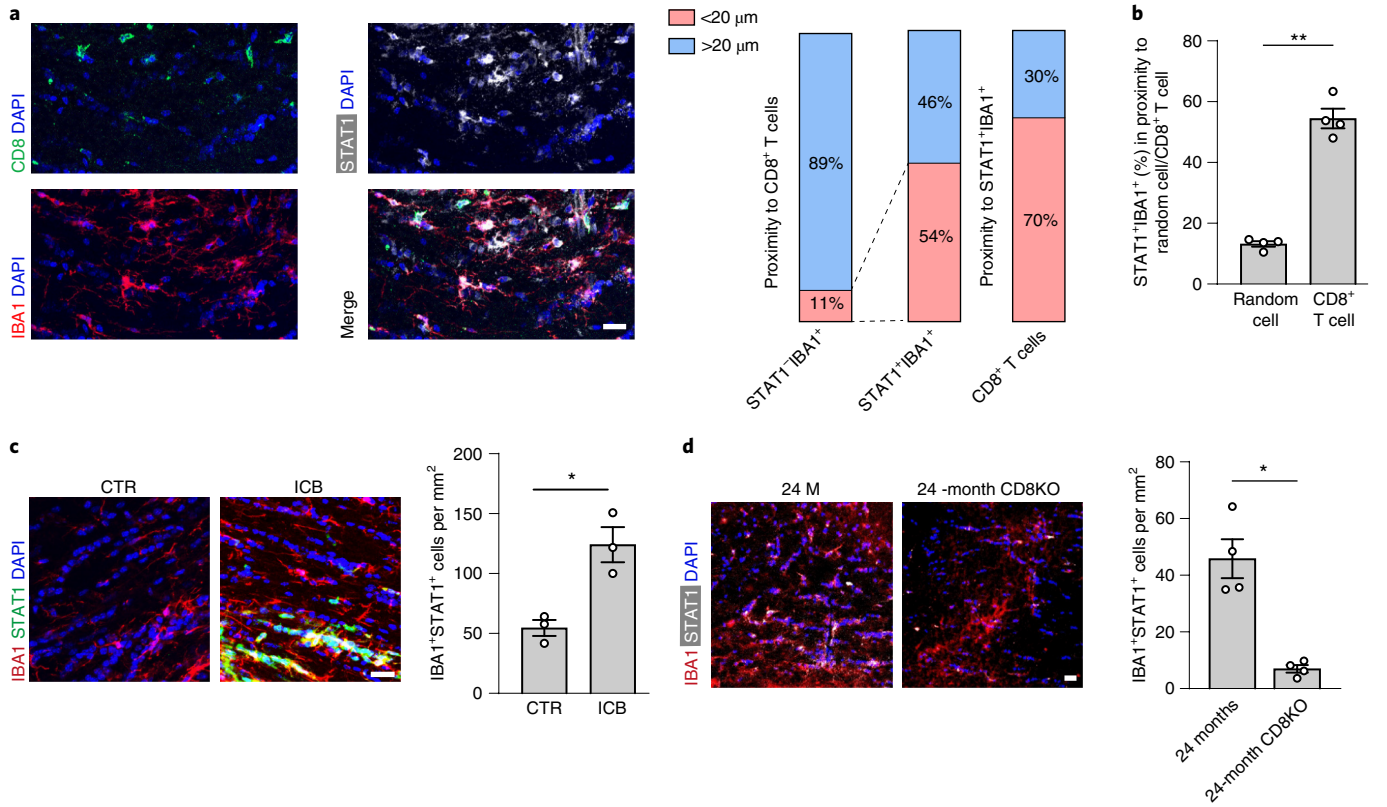

Fig. 5 | CD8$^+$ T cells induce an IFN-responsive microglia state in the aged white matter. a, Immunofluorescence staining and quantification of CD8$^+$ T cells (green) and STAT1$^+$IBA1$^+$ microglia proximity in the white matter of 24-month-old mice. Scale bars, 20 µm. Bar plots show quantification of STAT1$^+$ and STAT1$^-$IBA1$^+$ in proximity to CD8$^+$ T cells and vice versa (3 sections per mouse were selected, and a total of 117 CD8$^+$ T cells and 203 STAT1$^+$IBA1$^+$ microglia from 4 mice were analyzed). **b**, Quantification of the percentage of STAT1$^+$IBA1$^+$ microglia found in proximity to random cells compared with CD8$^+$ T cells ($n = 4$ mice per group, $^{**}P = 0.0052$; data are mean ± s.e.m.; P value represents a two-sided paired Student's t-test). **c**, Immunofluorescence staining and quantification of STAT1$^+$IBA1$^+$ microglia in the white matter of mice treated with anti-PD-1 and CTLA-4 (ICB) and isotype control antibodies (CTR) for 6 weeks starting at the age of 18 months ($n = 3$ mice per group, $^{*}P = 0.0125$; data are mean ± s.e.m.; P value represents a two-sided Student's t-test). Scale bar, 20 µm. **d**, Immunofluorescence staining and quantification of STAT1$^+$IBA1$^+$ microglia in the white matter of 24-month-old wild-type and 24-month-old *CD8*$^{-/-}$ mice ($n = 4$ mice per group, $^{*}P = 0.0223$; data are mean ± s.e.m.; P value represents a two-sided Student's t-test).

induce such lesions (Fig. 6f–h and Extended Data Fig. 9b). Previous studies have shown that IFN-γ can induce oligodendrocyte cell death in vitro and in vivo[40–42]. To directly determine the response of IFN-γ on oligodendrocytes, we treated primary cultures of mouse oligodendrocytes with IFN-γ. We used IFN-γ in concentrations that triggered STAT1 expression, to determine whether the induction was sufficient to induce cell death. Immunofluorescence analysis indicated that the STAT1$^+$ oligodendrocyte state did not affect cell viability in culture at this concentration (Fig. 6i). As IFN-γ is an important activator of microglia, we asked whether the cytotoxic effects of IFN-γ toward oligodendrocytes is mediated by microglia. Indeed, when oligodendrocytes were cocultured with microglia, a marked reduction of oligodendrocyte cell number was observed in the presence. but not in the absence, of IFN-γ (Fig. 6j). Thus, microglia can induce IFN-γ-mediated oligodendrocyte injury in vitro; however, other cells and mechanisms, such as direct CD8$^+$ T-lymphocyte-mediated cytotoxicity, might contribute to oligodendrocyte reactions during aging in vivo.

Discussion

White matter aging causes myelin degeneration, but how oligodendrocytes respond to aging is poorly defined. In the present study, we found that aging was associated with distinct oligodendrocyte responses, shown by the generation of a subpopulations of STAT1$^+$/B2M$^+$ and Serpina3n$^+$/C4b$^+$ oligodendrocytes and a reduction of oligodendrocyte density in aged white matter. We provided evidence that adaptive immune cells contributed to the cellular alterations that were associated with white matter aging. In both *Rag1*$^{-/-}$ and *CD8*$^{-/-}$ aged mice, the number of STAT1$^+$ oligodendrocytes decreased and the total density of oligodendrocytes increased to a similar extent, providing evidence that functional CD8$^+$ T cells are an important modifier of white matter aging. In addition, we identified a subpopulation of lymphocyte-dependent IFN-responsive microglia in aging white matter. These results show that adaptive immunity drives IFN-responsive cell states in aging white matter, but the exact link of CD8$^+$ T cells, microglia and oligodendrocytes remains to be established. Previous work has shown that CD8$^+$ T cells invading the aging brain exhibit high levels of IFN-γ, which drive IFN signaling within the neurogenic niche of the subventricular zone[35]. CD8$^+$ T-cell-derived IFN-γ may also induce IFN responses in oligodendrocytes and microglia, but the contribution of other IFNs cannot be excluded[43]. One possible scenario is the secretion of IFN-γ by CD8$^+$ T cells, which, in turn, polarizes microglia into an injurious phenotype. It is interesting to compare our results with a previous study using a viral model of encephalitis in mice, in which CD8$^+$ T-cell-derived IFN-γ triggers acute loss of axosomatic connections[44]. In this model, phagocytes activated by neurons, which have been stimulated by CD8$^+$ T-cell-derived IFN-γ triggers synapse loss[44]. Accordingly, it is conceivable that IFN-responsive oligodendrocytes actively recruit proinflammatory microglia as effector cells in aged white matter. Alternatively, CD8$^+$ T-lymphocyte cytotoxicity occurs in a cognate T-cell receptor- and granzyme B-dependent manner, as

https://doi.org/10.1038/s41593-022-01183-6

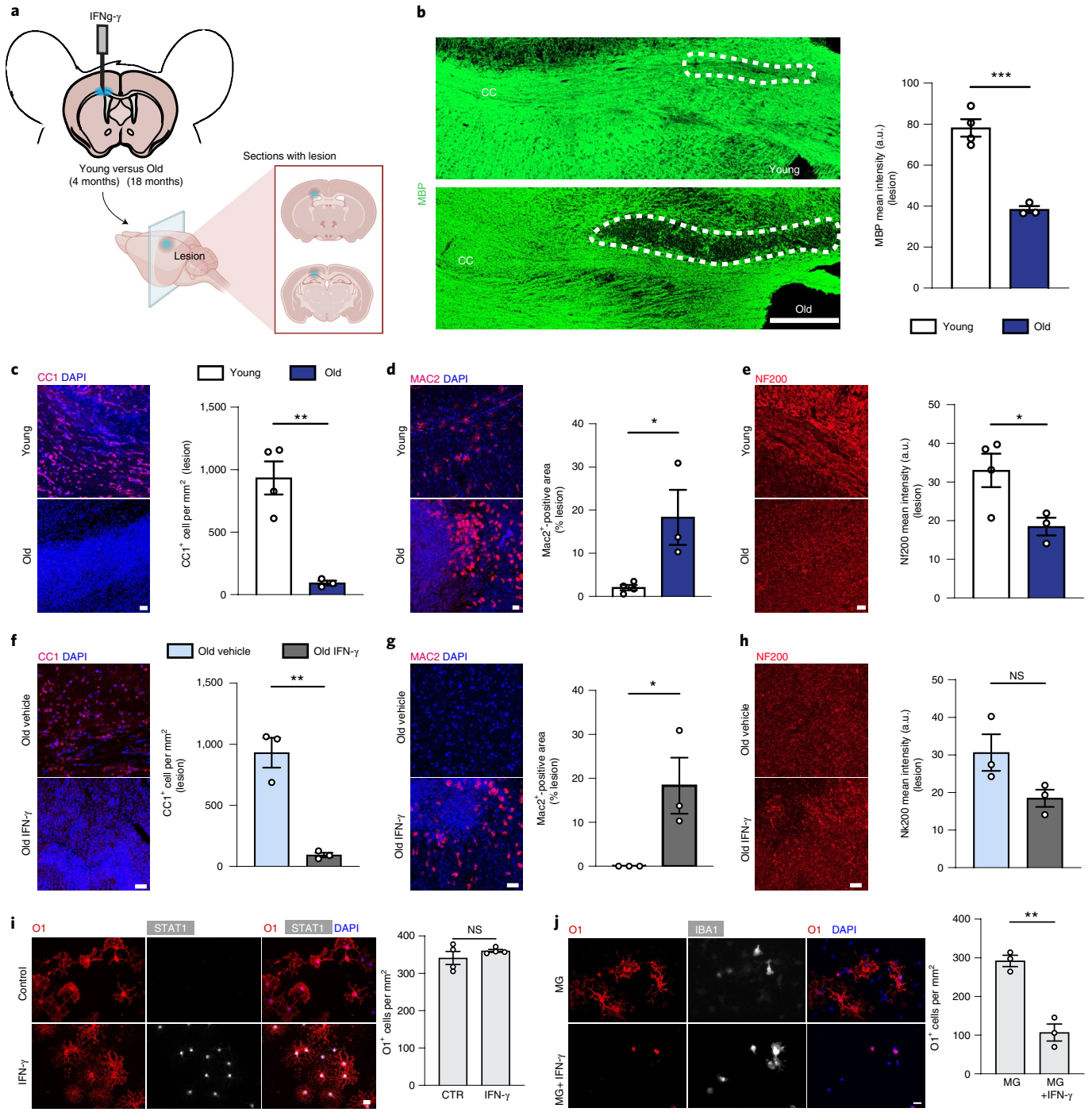

Fig. 6 | IFN-γ injections induce myelin and oligodendrocyte loss in aged mice. **a**, Diagram showing the model of IFN-γ injection in the corpus callosum (CC). The lesion area was identified by the positivity for monastral blue. **b**, Representative pictures of the CC after injection of 1 µl of a solution of 10 ng µl^{-1} of IFN-γ, 48 h postinjection. The intensity of the staining for MBP (green) was used to quantify the extent of demyelination (young, $n = 4$; old, $n = 3$; $^{***}P = 0.0006$; data are mean ± s.e.m.; P value represents a two-sided Student's t-test). a.u., arbitrary units. **c**–**e**, Representative confocal images and quantifications of IFN-γ-mediated lesions in young and old mice, showing CC1$^+$ oligodendrocytes (**c**), MAC2$^+$ microglia (**d**) and NF200$^+$ axons (**e**). The number of oligodendrocytes was expressed as number of cells per mm^2; the amount of phagocytes was expressed as percentage area of the lesion occupied by MAC2$^+$ cells; the extent of axonal damage was expressed as staining intensity of NF200 (young, $n = 4$; old, $n = 3$; CC1$^+$, $^{**}P = 0.0031$; MAC2$^+$, $^{*}P = 0.0291$; NF200$^+$, $^{*}P = 0.0451$; data are mean ± s.e.m.; P values represent a two-sided Student's t-test). Scale bar, 20 µm. **f**–**h**, Representative confocal images and quantifications of IFN-γ-mediated lesions in old mice and of the vehicle control showing CC1$^+$ oligodendrocytes (**f**), MAC2$^+$ cells (**g**) and NF200$^+$ axons (**h**) ($n = 3$ mice per group, CC1$^+$, $^{**}P = 0.0025$; MAC2$^+$, $^{*}P = 0.0451$; data are mean ± s.e.m.; P values represent a two-sided Student's t-test). **i**, Representative images of cultured oligodendrocytes (labeled for O1 in red and STAT1 in white) after treatment with IFN-γ for 24 h compared with control. Quantification of the number of oligodendrocytes after IFN-γ or vehicle treatment, expressed as number of O1$^+$ cells per mm^2 ($n = 4$ biological replicates per group, $^{**}P = 0.0022$; data are mean ± s.e.m.; P values represent a two-sided Student's t-test). **j**, Representative images of oligodendrocytes cultured with microglia alone (MG) or microglia together with IFN-γ (MG+IFN-γ) and stained for O1 (oligodendrocytes) and IBA1 (microglia). Quantification of the number of oligodendrocytes, expressed as number of O1$^+$ cells per mm^2 ($n = 4$ biological replicates per group, $^{**}P = 0.0022$; data are mean ± s.e.m.; P values represent a two-sided Student's t-test).

shown for axons in the optic nerve[34]. In this context, the age-related induction of Serpina3n$^+$ oligodendrocytes is of interest, because Serpina3n is an inhibitor of granzyme B that can dampen axon and myelin damage in autoimmune conditions[45]. Several studies have identified distinct populations of clonally expanded CD8$^+$ T cells expressing the checkpoint inhibitor PD-1 in aged mice and humans[35,46]. We found that treatment of mice with antibodies against the checkpoint receptors, CTLA-4 and PD-1, resulted in an increase in the number of CD8$^+$ T cells and IFN-responsive oligodendrocytes and microglia. These data could possibly explain why immune checkpoint inhibition in cancer causes behavioral and cognitive changes in some patients[47].

The temporal sequence and causality of pathological processes contributing to white matter aging need to be established. As the deep white matter areas lie at the ends of the arterial circulation, they are particularly susceptible to decreases in blood flow and oxygenation, possibly contributing to increased vulnerability of aged white matter to hypoperfusion and aging-induced leaky blood–brain barrier[48,49]. Progressive vascular damage, induced by injury to myelinated fibers, may promote the infiltration of CD8$^+$ T cells, thereby triggering harmful immune reactivity toward microglia and oligodendrocytes. A key question that remains to be established is how CD8$^+$ T cells enter the brain and whether antigen recognition is necessary for this process. The clonal expansion of CD8$^+$ T cells in aging provides evidence that they actively recognize antigen(s)[34,35]. It is unclear why CD8$^+$ T cells migrate specifically to the central nervous system white matter. It is possible that they are attracted by myelin self-antigens, reminiscent of the T cells found in multiple sclerosis. The long-lived myelin proteins and lipids may accumulate oxidation and posttranslational modifications during aging that lead to their recognition as neoantigens when presented to T cells. Proof of principle that oligodendrocyte pathology can trigger adaptive autoimmune responses against myelin has been provided in a model of oligodendrocyte ablation[50]. However, passive mechanisms such as age-related changes in the migration of CD8$^+$ T across a leaky blood–brain barrier, dural sinuses or choroid plexus are also conceivable. In addition, it remains to be clarified whether CD8$^+$ T cells produce IFN-γ in the aging white matter, as has been shown for the stem cell niches of aging mice[35].

Previous work has shown that oligodendrocytes are particularly sensitive to IFN-γ, because it can trigger oligodendroglial cell death and demyelination[40–42]. Strikingly, we find that this effect is highly pronounced in the aged brain, in which IFN-γ potently induces loss of oligodendrocytes and demyelinating injury. Possibly, the aging brain is primed toward IFN-γ due to age-associated, chronic, low-grade inflammation, so-called 'inflammaging'[51]. Notably, OPCs respond to IFN-γ by inducing the antigen presentation pathway to activate T cells, which in turn can kill the OPCs as their target cells[28,30]. Immune responses in the aging brain are not limited to oligodendrocyte-lineage cells and myelinated axons. Previous work has shown T-cell infiltration in the aged brain, where the T cells impair the function of neuronal stem cells within the neurogenic niche[35,52,53]. Intriguingly, proliferation of neural stem cells was inhibited by IFN-γ, which was secreted from CD8$^+$ T cells[35]. This mechanism is likely to be of functional relevance for the oligodendroglial lineage, because aging is not only associated with myelin degeneration but also with insufficient myelin renewal, a result of reduced capacity of OPCs to proliferate and differentiate[3,4,10,54,55]. Indeed, we found that myelin degeneration was not associated with an increase in OPC numbers in the aging brain.

As aging is the biggest factor for the most prevalent neurodegenerative diseases, it will be interesting to understand how the cellular alterations that occur in the white matter intermix with the pathology of these disorders. White matter changes and myelin alterations have been detected in Alzheimer's disease and its mouse models[18,56,57], which may contribute to disease pathology, including TREM2-dependent DAM signaling[16,17]; however, TREM2-independent glial responses have also been described[27,58]. As our previous work identified TREM2- and age-dependent, white matter-associated microglial responses, we analyzed the TREM2 dependence of IFN-responsive microglia but found instead a role of CD8$^+$ T cells.

Our data emphasize the contribution of CD8$^+$ T cells in triggering IFN-responsive cell states in the aging white matter, but it is likely that additional mechanisms contribute. In particular, prolonged exposure of nucleic acids to pattern-recognition, immune-sensing receptors can lead to inappropriate type I IFN release[59]. It is interesting that Aicardi–Goutieres syndrome, a prototype of an inherited disease with abnormal nucleic acid sensing and IFN induction, is associated with white matter pathology[59]. Likewise, deletion of ubiquitin-specific protease 18, a protein that negatively regulates STAT1 signaling, causes fatal activation of white matter microglia and myelin pathology[60,61]. Due to the extensive crosstalk between type 1 and type 2 IFN signaling pathways, future studies need to address their specific contribution within the different cell types during white matter aging.

Although the exact communication across CD8$^+$ T cells, microglia and oligodendrocytes and the link to IFN signaling remain to be established, these results support the hypothesis that cytotoxic CD8$^+$ T cells contribute to age-associated white matter decay.

Online content

Any methods, additional references, Nature Research reporting summaries, source data, extended data, supplementary information, acknowledgements, peer review information; details of author contributions and competing interests; and statements of data and code availability are available at https://doi.org/10.1038/s41593-022-01183-6.

References

1. Hou, Y. et al. Ageing as a risk factor for neurodegenerative disease. *Nat. Rev. Neurol.* **15**, 565–581 (2019).
2. Stadelmann, C., Timmler, S., Barrantes-Freer, A. & Simons, M. Myelin in the central nervous system: structure, function, and pathology. *Physiol. Rev.* **99**, 1381–1431 (2019).
3. Hughes, E. G., Orthmann-Murphy, J. L., Langseth, A. J. & Bergles, D. E. Myelin remodeling through experience-dependent oligodendrogenesis in the adult somatosensory cortex. *Nat. Neurosci.* https://doi.org/10.1038/s41593-018-0121-5 (2018).
4. Hill, R. A., Li, A. M. & Grutzendler, J. Lifelong cortical myelin plasticity and age-related degeneration in the live mammalian brain. *Nat. Neurosci.* https://doi.org/10.1038/s41593-018-0120-6 (2018).
5. Fard, M. K. et al. BCAS1 expression defines a population of early myelinating oligodendrocytes in multiple sclerosis lesions. *Sci. Transl. Med.* https://doi.org/10.1126/scitranslmed.aam7816 (2017).
6. Prins, N. D. & Scheltens, P. White matter hyperintensities, cognitive impairment and dementia: an update. *Nat. Rev. Neurol.* **11**, 157–165 (2015).
7. Sowell, E. R. et al. Mapping cortical change across the human life span. *Nat. Neurosci.* **6**, 309–315 (2003).
8. Bethlehem, R. A. I. et al. Brain charts for the human lifespan. *Nature* **604**, 525–533 (2022).
9. Brouwer, R. M. et al. Genetic variants associated with longitudinal changes in brain structure across the lifespan. *Nat. Neurosci.* **25**, 421–432 (2022).
10. Wang, F. et al. Myelin degeneration and diminished myelin renewal contribute to age-related deficits in memory. *Nat. Neurosci.* https://doi.org/10.1038/s41593-020-0588-8 (2020).
11. Pan, S., Mayoral, S. R., Choi, H. S., Chan, J. R. & Kheirbek, M. A. Preservation of a remote fear memory requires new myelin formation. *Nat. Neurosci.* https://doi.org/10.1038/s41593-019-0582-1 (2020).
12. Steadman, P. E. et al. Disruption of oligodendrogenesis impairs memory consolidation in adult mice. *Neuron* **105**, 150–164.e156 (2020).

13. Safaiyan, S. et al. Age-related myelin degradation burdens the clearance function of microglia during aging. *Nat. Neurosci.* **19**, 995–998 (2016).
14. Peters, A. The effects of normal aging on myelin and nerve fibers: a review. *J. Neurocytol.* **31**, 581–593 (2002).
15. Sala Frigerio, C. et al. The major risk factors for Alzheimer's disease: age, sex, and genes modulate the microglia response to abeta plaques. *Cell Rep.* **27**, 1293–1306.e1296 (2019).
16. Krasemann, S. et al. The TREM2-APOE pathway drives the transcriptional phenotype of dysfunctional microglia in neurodegenerative diseases. *Immunity* **47**, 566–581.e569 (2017).
17. Keren-Shaul, H. et al. A unique microglia type associated with restricting development of Alzheimer's disease. *Cell* **169**, 1276–1290.e1217 (2017).
18. Safaiyan, S. et al. White matter aging drives microglial diversity. *Neuron* **109**, 1100–1117.e1110 (2021).
19. Ximerakis, M. et al. Single-cell transcriptomic profiling of the aging mouse brain. *Nat. Neurosci.* **22**, 1696–1708 (2019).
20. Hammond, T. R. et al. Single-cell RNA sequencing of microglia throughout the mouse lifespan and in the injured brain reveals complex cell-state changes. *Immunity* **50**, 253–271.e256 (2019).
21. Friedman, B. A. et al. Diverse brain myeloid expression profiles reveal distinct microglial activation states and aspects of Alzheimer's disease not evident in mouse models. *Cell Rep.* **22**, 832–847 (2018).
22. Mombaerts, P. et al. RAG-1-deficient mice have no mature B and T lymphocytes. *Cell* **68**, 869–877 (1992).
23. Fung-Leung, W. P. et al. CD8 is needed for development of cytotoxic T cells but not helper T cells. *Cell* **65**, 443–449 (1991).
24. Fullgrabe, A. et al. Guidelines for reporting single-cell RNA-seq experiments. *Nat. Biotechnol.* **38**, 1384–1386 (2020).
25. Percie du Sert, N. et al. The ARRIVE guidelines 2.0: updated guidelines for reporting animal research. *PLoS Biol.* **18**, e3000410 (2020).
26. Marques, S. et al. Oligodendrocyte heterogeneity in the mouse juvenile and adult central nervous system. *Science* **352**, 1326–1329 (2016).
27. Zhou, Y. et al. Human and mouse single-nucleus transcriptomics reveal TREM2-dependent and TREM2-independent cellular responses in Alzheimer's disease. *Nat. Med.* **26**, 131–142 (2020).
28. Kirby, L. et al. Oligodendrocyte precursor cells present antigen and are cytotoxic targets in inflammatory demyelination. *Nat. Commun.* **10**, 3887 (2019).
29. Jakel, S. et al. Altered human oligodendrocyte heterogeneity in multiple sclerosis. *Nature* **566**, 543–547 (2019).
30. Falcao, A. M. et al. Disease-specific oligodendrocyte lineage cells arise in multiple sclerosis. *Nat. Med.* **24**, 1837–1844 (2018).
31. Mathys, H. et al. Single-cell transcriptomic analysis of Alzheimer's disease. *Nature* **570**, 332–337 (2019).
32. Kenigsbuch et al. A shared disease-associated oligodendrocyte signature among multiple CNS pathologies. *Nat. Neurosci.* https://doi.org/10.1038/s41593-022-01104-7 (2022).
33. Buttner, M., Ostner, J., Muller, C. L., Theis, F. J. & Schubert, B. scCODA is a Bayesian model for compositional single-cell data analysis. *Nat. Commun.* **12**, 6876 (2021).
34. Groh, J. et al. Accumulation of cytotoxic T cells in the aged CNS leads to axon degeneration and contributes to cognitive and motor decline. *Nat. Aging* **1**, 357–367 (2021).
35. Dulken, B. W. et al. Single-cell analysis reveals T cell infiltration in old neurogenic niches. *Nature* **571**, 205–210 (2019).
36. Tabula Muris, C. A single-cell transcriptomic atlas characterizes ageing tissues in the mouse. *Nature* **583**, 590–595 (2020).
37. Wei, S. C., Duffy, C. R. & Allison, J. P. Fundamental mechanisms of immune checkpoint blockade therapy. *Cancer Discov.* **8**, 1069–1086 (2018).
38. Schirmer, L. et al. Neuronal vulnerability and multilineage diversity in multiple sclerosis. *Nature* **573**, 75–82 (2019).
39. Turrin, N. P. & Rivest, S. Innate immune reaction in response to seizures: implications for the neuropathology associated with epilepsy. *Neurobiol. Dis.* **16**, 321–334 (2004).
40. Horwitz, M. S., Evans, C. F., McGavern, D. B., Rodriguez, M. & Oldstone, M. B. A. Primary demyelination in transgenic mice expressing interferon-γ. *Nat. Med.* **3**, 1037–1041 (1997).
41. Corbin, J. G. et al. Targeted CNS expression of interferon-gamma in transgenic mice leads to hypomyelination, reactive gliosis, and abnormal cerebellar development. *Mol. Cell Neurosci.* **7**, 354–370 (1996).
42. Vartanian, T., Li, Y., Zhao, M. & Stefansson, K. Interferon-gamma-induced oligodendrocyte cell death: implications for the pathogenesis of multiple sclerosis. *Mol. Med.* **1**, 732–743 (1995).
43. Baruch, K. et al. Aging. Aging-induced type I interferon response at the choroid plexus negatively affects brain function. *Science* **346**, 89–93 (2014).
44. Di Liberto, G. et al. Neurons under t cell attack coordinate phagocyte-mediated synaptic stripping. *Cell* **175**, 458–471.e419 (2018).
45. Haile, Y. et al. Granzyme B-inhibitor serpina3n induces neuroprotection in vitro and in vivo. *J. Neuroinflammation* **12**, 157 (2015).
46. Gate, D. et al. Clonally expanded CD8 T cells patrol the cerebrospinal fluid in Alzheimer's disease. *Nature* **577**, 399–404 (2020).
47. Hottinger, A. F. Neurologic complications of immune checkpoint inhibitors. *Curr. Opin. Neurol.* **29**, 806–812 (2016).
48. Joutel, A. Prospects for diminishing the impact of nonamyloid small-vessel diseases of the brain. *Annu. Rev. Pharmacol. Toxicol.* **60**, 437–456 (2020).
49. Montagne, A. et al. Blood–brain barrier breakdown in the aging human hippocampus. *Neuron* **85**, 296–302 (2015).
50. Traka, M., Podojil, J. R., McCarthy, D. P., Miller, S. D. & Popko, B. Oligodendrocyte death results in immune-mediated CNS demyelination. *Nat. Neurosci.* **19**, 65–74 (2016).
51. Franceschi, C., Garagnani, P., Parini, P., Giuliani, C. & Santoro, A. Inflammaging: a new immune–metabolic viewpoint for age-related diseases. *Nat. Rev. Endocrinol.* **14**, 576–590 (2018).
52. Kalamakis, G. et al. Quiescence modulates stem cell maintenance and regenerative capacity in the aging brain. *Cell* **176**, 1407–1419.e1414 (2019).
53. Buckley, M. T. et al. Cell type-specific aging clocks to quantify aging and rejuvenation in regenerative regions of the brain. Preprint at *bioRxiv* https://doi.org/10.1101/2022.01.10.475747 (2022).
54. Neumann, B. et al. Metformin restores CNS remyelination capacity by rejuvenating aged stem cells. *Cell Stem Cell* **25**, 473–485.e478 (2019).
55. Young, K. M. et al. Oligodendrocyte dynamics in the healthy adult CNS: evidence for myelin remodeling. *Neuron* **77**, 873–885 (2013).
56. Chen, J. F. et al. Enhancing myelin renewal reverses cognitive dysfunction in a murine model of Alzheimer's disease. *Neuron* **109**, 2292–2307.e2295 (2021).
57. Nasrabady, S. E., Rizvi, B., Goldman, J. E. & Brickman, A. M. White matter changes in Alzheimer's disease: a focus on myelin and oligodendrocytes. *Acta Neuropathol. Commun.* **6**, 22 (2018).
58. Lee, S. H. et al. TREM2-independent oligodendrocyte, astrocyte, and T cell responses to tau and amyloid pathology in mouse models of Alzheimer disease. *Cell Rep.* **37**, 110158 (2021).
59. Crow, Y. J. & Manel, N. Aicardi–Goutieres syndrome and the type I interferonopathies. *Nat. Rev. Immunol.* **15**, 429–440 (2015).

60. Goldmann, T. et al. USP18 lack in microglia causes destructive interferonopathy of the mouse brain. *EMBO J.* **34**, 1612–1629 (2015).
61. Schwabenland, M. et al. Loss of USP18 in microglia induces white matter pathology. *Acta Neuropathol. Commun.* **7**, 106 (2019).

Methods

Animals

The mouse lines used in the present study are the following: wild-type C57BL/6J mice were from Janvier Labs; *Trem2*$^{-/-}$ mice[62] on the C57BL/6J background were kindly provided by C. Haass, Laboratory of Neurodegenerative Disease Research, German Center for Neurodegenerative Diseases (DZNE), Munich; *Rag1*$^{-/-}$ (B6.129S7-Rag1tm1Mom/J)[22] and *Cd8*$^{-/-}$ mice (B6.129S2-Cd8atm1Mak/J)[23] and wild-type controls were on the C57BL/6J background. Experiments were performed with young, adult and aged mice (aged 3, 12, 18 and 24 months) as indicated in the figures and legends. Only aged mice that were on inspection healthy were used for experiments. Animals were randomly assigned to the different groups. Treatment with antibodies against PD-1 and CTLA-4 and their respective isotype controls was performed in 18-month-old mice; mice were injected intraperitoneally with a mix of both antibodies of concentration 10 mg kg^{-1} (PD-1) and 20 mg kg^{-1} (CTLA-4) twice a week for 6 weeks in total. All animal experiments were reviewed and overseen by the institutional animal use and care committee of the DZNE in Munich and the University Hospital in Würzburg. All animals were free from the most common mouse viral pathogens, ectoparasites, endoparasites and mouse bacterial pathogens harbored in research animals. The battery of screened infective agents met the standard health profile established in the animal facility in the DZNE animal housing facility. The mice were kept in groups in Greenline IVC GM500 plastic cages and were housed in a temperature-controlled environment (21 ± 2 °C) on a 12 h light:dark cycle with standard chow and water freely available. Water was provided in a water bottle, which was changed weekly. Cages were changed every week.

Mice perfusion and cell isolation for Smart-seq2

Four young (3-month-old) and four old (24-month-old) male C57BL/6J mice were deeply anesthetized and perfused with cold phosphate-buffered saline (PBS; Sigma-Aldrich, catalog no. D8537). Each brain was carefully removed and individually microdissected under a dissection microscope; gray matter was isolated from the frontal cortex and white matter was carefully isolated from the optic tract, medial lemniscus and corpus callosum (attached gray matter and choroid plexus were removed). We used our previously established isolation protocol[63] using gentleMACS with the Neural Tissue Dissociation Kit (Papain; Miltenyi Biotec) and a final concentration of 45 mM actinomycin D (Act-D, Sigma-Aldrich, catalog no. A1410). Subsequently, cells were blocked with mouse FcR-blocking reagent (CD16/CD32 Monoclonal Antibody, eBioscience, catalog no. 14-0161-82,1100), stained with antibodies against CD11b (PE/Cy7, M1/70, eBioscience, catalog no. 48-0451-82, 1:200) and afterward washed with PBS. Before sorting, the cell suspensions were stained by the live/dead marker SYTOX Blue (final concentration 1 µM). Viable (SYTOX Blue-negative) nonmyeloid single cells (CD11b^{-} cells) were sorted by flow cytometry (Sony, catalog no. SH800). Single cells were sorted into 96-well plates filled with 4 ml of lysis buffer containing 0.05% Triton X-100 (Sigma-Aldrich) and ERCC (External RNA Controls Consortium) RNA spike-in Mix (Ambion, Life Technologies; 1:24,000,000 dilution), 2.5 mM oligo(dT), 2.5 mM dNTP and 2 U ml^{-1} of recombinant RNase inhibitor (Clontech), then spun down and frozen at −80 °C. Plates were thawed and libraries prepared as described below.

Library preparation for Smart-seq2

The 96-well plates containing the sorted single cells were first thawed and then incubated for 3 min at 72 °C and thereafter immediately placed on ice. To perform reverse transcription (RT) we added to each well a mix of 0.59 µl of H_2O, 0.5 µl of SMARTScribe Reverse Transcriptase (Clontech), 2 µl of 5× First Strand buffer, 0.25 µl of Recombinant RNase Inhibitor (Clontech), 2 µl of Betaine (5 M Sigma), 0.5 µl of dithiothreitol (100 mM), 0.06 µl of $MgCl_2$ (1 M, Sigma-Aldrich) and 0.1 µl of template-switching oligos (TSOs) (100 µM, AAGCAGTGGTATCAACGCAGAGTACrGrG + G). Next, RT reaction mixes were incubated at 42 °C for 90 min, followed by 70 °C for 5 min and 10 cycles of 50 °C for 2 min and 42 °C for 2 min, finally ending with 70 °C for 5 min for enzyme inactivation. Preamplification of complementary DNA was performed by adding 12.5 µl of KAPA HiFi Hotstart 2× (KAPA Biosystems), 2.138 µl of H_2O, 0.25 µl of ISPCR primers (10 µM, 5′-AAGCAGTGGTATCAACGCAGAGT-3′) and 0.1125 µl of lambda exonuclease under the following conditions: 37 °C for 30 min, 95 °C for 3 min, 23 cycles of 98 °C for 20 s, 67 °C for 15 s and 72 °C for 4 min, and a final extension at 72 °C for 5 min. Libraries were then cleaned using AMPure bead (Beckman-Coulter) clean-up at a 0.7:1 beads:PCR product ratio. Libraries were assessed using Bio-analyzer (Agilent, catalog no. 2100), using the High Sensitivity DNA analysis kit, and also fluorometrically using Qubit's DNA HS assay kits and a Qubit 4.0 Fluorometer (Invitrogen, Life Technologies) to measure the DNA concentrations. Further selection of samples was performed via quantitative PCR assay against ubiquitin transcript Ubb77 (primer 1 5′-GGAGAGTCCATCGTGGTTATTT-3′; primer 2 5′-ACCTCTAGGGTGATGGTCTT-3′; probe 5′-/5Cy5/TGCAGATCTTCGTGAAGACCTGAC/3IAbRQSp/−3′) measured on a LightCycler 480 Instrument II (Roche). Samples were normalized to 160 pg µl^{-1}. Sequencing libraries were constructed using in-house-produced Tn5 transposase33. Libraries were barcoded and pooled then underwent three rounds of AMPure bead (Beckman-Coulter) clean-up at a 0.8:1 ratio beads:library. Libraries were sequenced 2× 150 reads bp paired-end on Illumina HiSeq4000 to a depth of 3 × 105–4 × 105 reads per sample.

Processing, quality control and analyses of Smart-seq2 scRNA-seq data

BCL files were demultiplexed with the bcl2fastq software from Illumina. After quality control with FastQC, reads were aligned using rnaSTAR[64] to the GRCm38 (mm10) genome with ERCC synthetic RNA added. Read counts were collected using the parameter 'quantMode GeneCounts' of rnaSTAR and the unstranded values. Quantitative criteria were used to filter out low-quality cells as shown in Extended Data Fig. 1b. We observed the distribution of all samples for each quality metrics and defined thresholds to remove outliers or samples with abnormal values. In the same order as in Extended Data Fig. 1b, we considered the number of reads per sample (≥20,000 and ≤4 × 10^6), the number of genes per sample (≥1,000 and ≤6,500), the average sequence read length after trimming (≥180 and ≤200), the mismatch rate during alignment (≥0.15 and ≤0.5), the percentage of uniquely mapped reads (≥68 and ≤100), the percentage of multimapped reads (≥2.3 and ≤7.7), the percentage of reads considered too short (≥0 and ≤17), the percentage of ERCCs (≥0 and ≤0.011) and the percentage of mitochondrial genes (≥0 and ≤0.006). From 2,650 single cells, 2,538 passed quality control. From that point, Seurat v.3.2.3R package was utilized[65]. Gene expressions were normalized using the SCTransform function (3,000 variable features) within Seurat. The first eight PCs were selected based on the elbow plot and heatmap of PC embeddings and used for downstream analysis steps. Cell-type clusters were identified using the Louvain algorithm and annotated by canonical cell-type markers (Extended Data Fig. 1c,d). Oligodendrocytes (2,413 single cells) were extracted and analyzed separately. After processing with SCTransform (2,000 variable features), the first 10 PCs were considered for downstream analyses. Unbiased clustering was performed using the Louvain algorithm that led to the identification of the four aforementioned oligodendrocyte populations. Gene sets of clusters 1, 2, 3 and 4 were defined by using the FindMarkers function with a threshold of avg_log$_2$(fold-change) (avg_log$_2$(FC)) > 1 (Fig. 1g). GO analyses were performed with the DAVID annotation tool[66], STRING[67] and Metascape[68].

Mice perfusion and cell isolation for 10× genomic experiments

For 10× genomic experiments, mice were deeply anesthetized and perfused with cold PBS. Each brain was removed, individually

microdissected under a dissection microscope and dissociated in the same way as described above (10× mice information is provided in Supplementary Table 2). To collect enough cells for loading on to the 10× Genomics Chromium chip, two gray matter/white matter tissue samples were combined into one sample. After tissue dissociation, SYTOX Blue-negative cells were sorted into a 2-ml Eppendorf tube with 1 ml of RPMI + 5% fetal bovine serum (FBS). Sorted cells were centrifuged at 300*g* for 10 min at 4 °C. Cell pellets were resuspended in 0.04% bovine serum albumin (BSA) + PBS catching medium at a concentration of 700–900 cells per µl.

Library preparation for 10× genomic experiments

Single-cell suspensions were loaded on to the Chromium Single Cell Controller using the Chromium Single Cell 3′ Library & Gel Bead Kit v.3.1 (10× Genomics) chemistry following the manufacturer's instructions. Sample processing and library preparation were performed according to the manufacturer's instructions using AMPure beads (Beckman-Coulter). Libraries were sequenced on the DNBSEQ Sequencing System (BGI group).

Preprocessing and analyses of 10× data

Fastq files were processed with Cell Ranger v.3.0.2 (wild-type aging), 4.0.0 (Rag1KO 1st batch) and 6.1.2 (Rag1KO 2nd batch). From that point, the Seurat v.3.2.3R package[65] was used for downstream analyses. Unless stated otherwise, all gene expression matrices were filtered with the parameters 'min.cells=3', 'min.genes=200' and 'mitochondrial percentage>0.10' (Extended Data Fig. 6c), removing cells with <200 genes and mitochondrial gene percentage >10% and keeping genes with expression in at least 3 cells. Further sets of filters are explained in detail for each sample.

Wild-type aging datasets. The two batches of libraries (Supplementary Table 2) were processed separately. For the first batch, expression matrices were filtered by number of unique molecular modifiers (UMIs) (<30,000) and genes (<6,000). Processed data were normalized with the SCTransform function (variable.features.rv.th=1.4) and the top 9 PCs were selected for downstream analyses on inspection. Major cell types were identified using Louvain clustering and canonical cell-marker expression. Oligodendrocytes were extracted to be analyzed separately. The oligodendrocyte subset dataset was processed with SCTransform (variable.features.rv.th=1.5), principal component analysis (ten PCs) and Louvain clustering as explained earlier. In addition, *Gm42418* and *AY036118* genes were removed from the expression matrix because they indicate ribosomal RNA contamination[69].

The samples in the second batch were analyzed similarly; by extracting the oligodendrocytes after processing the libraries by quality control (QC) filtering, normalization, dimensionality reduction, clustering and cell-type annotation. QC filtering was done by number of UMIs (<50,000) and genes (<8,000). The filtered expression matrix was normalized by SCTransform (variable.features.rv.th=1.4 and regression by 'mitochondrial percentage'). The top 30 PCs were picked for downstream analyses. The oligodendrocyte subset dataset was again put through the same processing steps: SCTransform (top 750 variable genes) normalization, preceding downstream analyses conducted with the top 10 PCs.

To avoid batch-specific effects while still preserving biological variability, the sequenced libraries (four sequencing runs from eight animals) were integrated using the Seurat 3 CCA integration workflow[70]. Both the dataset with all cell types and the oligodendrocyte subset dataset were integrated using the integration steps tailored for SCTransform-normalized datasets. For the dataset with all cell types, the first 30 PCs were selected for the downstream analyses. Major cell types were identified using Louvain clustering and canonical cell-marker expression (Extended Data Fig. 1e,f).

For the oligodendrocyte dataset integration, the top 750 most variable genes and the top 20 PCs were selected for the 'anchoring'. After the integration, the top 10 PCs were used for downstream steps and unbiased clustering with a resolution of 0.5 identified the aforementioned 7 oligodendrocyte populations.

Rag1KO datasets. Samples from the two batches were analyzed separately, similar to the steps described for the wild-type aging datasets. For the first batch, expression matrices were filtered by number of UMIs (<20,000). Processed data were normalized using the SCTransform function (variable.features.rv.th=1.4 and regression by 'mitochondrial percentage'). The top 30 PCs were selected for downstream analyses and major cell types were identified using Louvain clustering and canonical cell-marker expression. A small cluster with high microglial-marker gene expression was removed. Oligodendrocytes were extracted and analyzed separately before integration. *Gm42418* and *AY036118* genes were removed from the expression matrix to prevent technical artifacts. In addition, a small cluster with high microglial-marker gene expression were removed. The same normalization parameters were applied: variable.features.rv.th=1.4 and regression by 'mitochondrial percentage'. The second batch of samples (both all cell types and oligodendrocyte subsets) were analyzed in the same way with the exception of filtering parameters (number of UMIs <25,000 and genes <8,000).

Integration of wild-type and Rag1KO datasets. The Seurat v.3 RPCA integration method was used to analyze wild-type and Rag1KO samples together. Previously described four batches of oligodendrocytes subsets (eight sequencing runs in total, four per genotype) were integrated (Fig. 3d and Extended Data Fig. 6c). The 500 most variable genes from each batch and the top 20 PCs were used in the 'anchoring' (k.anchor=3) of the Seurat objects. Postintegration, the top 15 PCs were selected for downstream analyses. Unbiased clustering identified the same oligodendrocyte populations as previously described.

To analyze wild-type and Rag1KO microglia, our previously described microglia dataset[18] was integrated together with the microglia from our Rag1KO libraries. Four batches of microglia subsets (eight sequencing runs in total, four per genotype) were integrated (Fig. 4a and Extended Data Fig. 6c). The 750 most variable genes from each batch and the top 15 PCs were used in the 'anchoring' (k.anchor=4, max. features=100) of the Seurat objects. Postintegration, the top 15 PCs were selected for downstream analyses. Unbiased clustering identified the same microglial populations in Safaiyan et al.[18] with addition to IFN-responsive microglia.

Datasets generated in the present study and external datasets (12 sequencing runs, 4 from Safaiyan et al.[18], 8 from the present study) were integrated using RPCA (Fig. 3a). The 3,000 most variable genes and default parameters for other functions were used in the 'anchoring'. The first 30 PCs were selected for clustering analysis and major cell types were identified using canonical marker genes.

Integration of CD8 T-cell datasets. Processed gene expression matrices and metadata of brain (FACS), kidney (droplet), lung (droplet) and spleen (droplet) datasets from the mouse aging single-cell transcriptomic atlas[36] were downloaded. After filtering based on gene expression and age, only $CD8^+$ T cells from 21- and 24-month-old samples were kept. The processed gene expression matrix and metadata were provided on request by the authors for the Groh et al. dataset[34]. These five datasets were integrated with the RPCA workflow for log(normalized datasets); the 500 most variable genes and the top 10 PCs were used in the anchoring steps. The integrated dataset was scaled with default parameters and the top ten PCs were used to calculate the UMAP.

All differential gene expression analyses were conducted using the FindMarkers function with Wilcoxon's rank-sum test. The scCODA v.0.1.6 package was used for compositional analysis of the single-cell data. The

false discovery rate (FDR) value was set to 0.4 to be able to detect subtle yet biologically relevant changes, as described by the authors in their documentation. In all boxplots, the central line denotes the median, boxes represent the interquartile range (IQR) and whiskers show the distribution except for outliers. Outliers are all points outside 1.5× the IQR.

Immunohistochemistry

Animals were anesthetized by 10 mg ml^{-1} of ketamine and 1 mg ml^{-1} of xylazine solution intraperitoneally and perfused transcardially with 4% paraformaldehyde (PFA). Postfixation of brain tissue was done in 4% PFA overnight. Then the brain tissue was further cryoprotected in 30% sucrose in PBS for 24 h. After freezing the tissue on dry ice using Tissue-Tek O.C.T, 30-µm coronal sections were cut using a cryostat Leica CM1900. Free-floating sections were collected in a solution containing 25% glycerol and 25% ethylene glycol in PBS. The sections were rinsed with 1× PBS containing 0.2% Tween-20 and permeabilized in 0.5% Triton X-100 for 30 min. Fab fragment goat anti-mouse immunoglobulin G (1:100, Dianova) was added for 1 h at room temperature to block endogenous mouse tissue immunoglobulins. After a brief wash the sections were blocked for 1 h at room temperature in a solution containing 2.5% fetal calf serum, 2.5% BSA and 2.5% fish gelatin in PBS. Primary antibodies, diluted in 10% blocking solution, were incubated overnight at 4 °C. On the following day, sections were incubated with secondary antibodies, diluted in 10% blocking solution, for 2 h at room temperature. The sections were washed with PBS followed by DAPI incubation in 1× PBS for 10 min and mounted. The following antibodies were used: mouse anti-APC (Millipore, catalog no. OP80-100UG, 1:100), rabbit anti-B2m (abcam, catalog no. ab75853-100ul, 1:100), rabbit anti-STAT1 (Cell Signaling Technology, catalog no. 14994S, 1:250), rat anti-CD8 (Promega, catalog no. 100702, 1:100), rabbit anti-Iba1 (Wako, catalog no. 234 004, 1:250), goat anti-Serpina3n (Bio-Techne, catalog no. AF4709, 1:100), rat anti-C4b (Thermo Fisher Scientific, catalog no. MA1-40047,1:25), rabbit anti-Olig2 (Millipore, catalog no. AB9610, 1:250), mouse anti-Gstp (BD, catalog no. 610719, 1:250), rat anti-Mac2 (BioLegend, catalog no. 125402, 1:250), chicken anti-MBP (Thermo Fisher Scientific, catalog no. PA1-10008, 1:1,000), chicken anti-neurofilament heavy polypeptide (abcam, catalog no. ab4680, 1:400), anti-PDGF-Ralpha (R&D Systems, catalog no. 1:100), goat anti-CD69 (R&D Systems,1:100), goat anti-PD-1 (R&D Systems,1:100), rabbit anti-LAG-3 antibody (Abcam, 1:100), AF1062FM green fluorescent myelin stain (Thermo Fisher Scientific, catalog no. F34651, 1:400), anti-mouse 555 (Thermo Fisher Scientific, catalog no. A-21422, 1:500), anti-mouse 647 (Thermo Fisher Scientific, catalog no. A-21235, 1:500), anti-mouse 488 (Thermo Fisher Scientific, catalog no. A-21202, 1:500), anti-rabbit 555 (Thermo Fisher Scientific, catalog no. A-21428, 1:500), anti-rabbit 488 (Thermo Fisher Scientific, catalog no. A-11008,1:500), anti-rat 555 (Thermo Fisher Scientific, catalog no. A-21434, 1:5600), anti-goat 555 (Thermo Fisher Scientific, catalog no. A-32116, 1:500), donkey anti-rat 488 (Thermo Fisher Scientific, 1:500), donkey anti-goat 555 (Thermo Fisher Scientific, 1:500) and donkey anti-rabbit 647 (Thermo Fisher Scientific, 1:500). For CC1, B2m, Gstp, OLIG2, STAT1 and Serpina3n staining, antigen retrieval protocol using citrate buffer (10 mM, pH 6) was performed on free-floating sections, followed by a staining protocol as mentioned above. For CD8, STAT1 and CC1/IBA1 combined staining, the sections were permeabilized with 0.5% Triton X-100 for 30 min at room temperature and blocked in 5% goat serum, and primary antibodies, diluted in 10% blocking solution, were added and incubated overnight at 4 °C with 0.5% Triton X-100 for 30 min at room temperature and blocked in 5% goat serum; secondary antibodies include goat anti-rabbit IgG antibody (H + L), biotinylated (Vector Laboratories, 1:200), goat anti-rat 488 and goat anti-mouse 647 (Invitrogen, 1:500) for 1 h at room temperature. Sections were then washed with PBS and incubated with streptavidin 555 (Invitrogen, 1:500). To determine the proximity of $CD8^+$ T cells to $STAT1^+CC1^+$ oligodendrocytes (IROs), $CD8^+$ T cells (or random $DAPI^+$ cells) were selected manually, from which a circle with a 20-µm radius was drawn from the center of the cell via ImageJ automatically. We then quantified the percentage of $STAT1^+CC1^+$ oligodendrocytes located within that circle. Conversely, we proceeded similarly but took oligodendrocytes as a reference and quantified the T cells within a circle with a 20-µm radius. The same quantification method was applied to determine the proximity of $CD8^+$ T cells to $STAT1^+IBA1^+$ microglia (IRM). Images were acquired via a Leica TCS SP5 confocal microscope or with an LSM900 Zeiss microscope and were processed and analyzed with ImageJ 1.41 image-processing software.

Correlated light and electron microscopy

Mice were perfused by 4% PFA (electron microscope (EM) grade, Science Services) in PBS (pH 7.4), the brain dissected and vibratome sectioned coronally at 100-µm thickness. Every second section was subjected to immunohistochemistry, whereas the remaining sections were postfixed with 2.5% glutaraldehyde in 0.1 M cacodylate buffer (Science Services) for potential EM. The method of immunohistochemistry for Iba1 staining was described as above. Sections were assessed by fluorescence imaging for sites of Iba1 enrichment in the corpus callosum, indicative of microglial nodules. The adjacent EM section was selected and subjected to a standard rOTO contrasting procedure. After postfixation in 2% osmium tetroxide (Electron Microscope Services), 1.5% potassium ferricyanide (Sigma-Aldrich) in 0.1 M sodium cacodylate, staining was enhanced by reaction with 1% thiocarbohydrazide (Sigma-Aldrich) for 45 min at 40 °C. The tissue was washed in water and incubated in 2% aqueous osmium tetroxide, washed and further contrasted by overnight incubation in 1% aqueous uranyl acetate at 4 °C and 2 h at 50 °C. Samples were dehydrated in an ascending ethanol series and infiltration with LX112 (LADD). We serially sectioned the tissue at 200-nm thickness on to carbon nanotube (CNT) tape (Science Services) on an ATUMtome (Powertome, RMC) using a 35° ultra-diamond knife (Diatome). CNT tape stripes were assembled on to adhesive carbon tape (Science Services) attached to 4-inch silicon wafers (Siegert Wafer) and grounded by adhesive carbon tape strips (Science Services). EM micrographs were acquired on a Crossbeam Gemini 340 SEM (Zeiss) with a four-quadrant backscatter detector at 8 kV. Overview scans were taken at 200-nm lateral and higher resolution scans at 20-nm lateral resolution. Serial section data were aligned by a sequence of automatic and manual processing steps in Fiji TrakEM2 (ref. [71]) and relevant regions selected.

Subregional localization analysis

To compare the difference between frontal white matter and medial white matter, coronal sections with corpus callosum were divided into two groups following the *Allen Mouse Brain Atlas*: the white matter in the front of the brain, which does not contain lateral ventricles, was defined as 'frontal white matter' and white matter from sections that have lateral ventricles is defined as 'medial white matter'. For each quantification, two brain sections were selected from each group of three to four mice. For statistical analysis the paired Student's *t*-test was used.

RNAscope in situ hybridization

RNAscope in situ hybridization assay was applied to detect *Mbp* mRNA in the brain cryosections prepared from aged wild-type mice as performed previously[18]. The assay was performed using a commercially available RNAscope Multiplex Fluorescent Detection Reagent v.2 (Advanced Cell Diagnostics) kit and the manufacturer's instructions were followed. Briefly, 30-µm cryosections were fixed on superfrost plus slides; they were pretreated with hydrogen peroxide for 10 min at room temperature and then with antigen retrieval reagent (5 min of boiling) to unmask the target RNA. After applying Protease III on the sections for 30 min at 40 °C, probe hybridization was done by incubating sections in mouse *Mbp* probe assigned to channel 3, diluted 1:50 in probe diluent, for 2 h at 40 °C. Afterwards, signal amplification and detection were performed according to the kit's instruction. Signal

detection was done using Opal dyes (Opal520-green) diluted 1:3,000 in tyramide signal amplification (TSA) buffer. To visualize microglia, after in situ hybridization, an immunohistochemistry assay was performed using Iba1 antibody (Wako, 1:1,000). After washing with 1× PBS, sections were incubated for 30 s with 1× TrueBlack to remove autofluorescence background. The nuclei of cells were counterstained with DAPI and mounted. Images were acquired via a Leica TCS SP5 confocal microscope or with an LSM900 Zeiss microscope and were processed and analyzed with ImageJ 1.41 image-processing software.

Cell culture

OPCs were prepared from P8 C57BL/6J mouse brains by immunopanning[72]. Briefly, brains were dissociated to single-cell suspension, which was passed through two negative-selection plates coated with BSL1 to remove microglia. The remaining cell suspension was then incubated in a positive-selection plate coated with anti-CD140a antibodies. The attached cells were collected by accutase and cultured on poly(L-lysine)-coated coverslips in proliferation medium containing Dulbecco's modified Eagle's medium (DMEM; Thermo Fisher Scientific, catalog no. 41965), Sato Supplement, B-27 Supplement, GlutaMAX, Trace Elements B, penicillin–streptomycin, sodium pyruvate, insulin, *N*-acetyl-L-cysteine, D-biotin, forskolin, ciliary neurotrophic factor (CNTF), platelet-derived growth factor (PDGF) and neurotrophin-3 (NT-3). Primary microglia cultures were prepared from p11 C57BL/6J mouse brains. The brains were homogenized to a single-cell suspension using the neural tissue dissociation kit (Miltenyi Biotech, catalog no. 130-092-628) and by filtering the homogenate through a 70-µm cell strainer to remove tissue debris. Then, the cells were incubated with magnetic beads against CD11b and the solution was passed through a magnetic column. Microglia were flushed and plated in DMEM supplemented with 10% bovine calf serum, 10 ng ml^{-1} of monocytic colony-stimulating factor, 1% penicillin–streptomycin and 1% glutamate for 4–7 d before using them for experiments. For the coculture experiments, OPCs were cultured in differentiation medium containing DMEM (Thermo Fisher Scientific), Sato Supplement, B-27 Supplement, GlutaMAX, Trace Elements B, penicillin–streptomycin, sodium pyruvate, insulin, *N*-acetyl-l-cysteine, D-biotin, forskolin, CNTF and NT-3. After 1.5 d, when OPCs had differentiated into oligodendrocytes, microglia were collected after scraping, counted and plated with oligodendrocytes. After 6 h, IFN-γ (Millipore, catalog no. IF005) in 5 mM phosphate buffer, pH 8.0 containing 0.1% BSA was diluted 1:5,000 in the coculture to a final concentration of 0.1 ng µl^{-1}. For the control, phosphate buffer containing BSA was diluted in the same way. After 2 d, the coculture was fixed and analyzed by immunocytochemistry. Briefly, the cells were permeabilized with 0.1% Triton X-100 for 1 min and blocked in 10% blocking solution for 1 h. The cells were then incubated with primary antibodies overnight at 4 °C, washed twice in PBS and incubated for 1 h at room temperature with secondary antibodies. Oligodendrocytes were stained for O1 (mouse hybridoma, 1:5), microglia for IBA1 (Wako, catalog no. 234 004, 1:250) and nuclei were stained with DAPI. After mounting, the cells were imaged on a Leica DMI6000 widefield microscope (×20, 0.4 numerical aperture, air objective) and analyzed using Fiji.

Stereotactic injection in the corpus callosum

A solution of 10 ng µl^{-1} of IFN-γ was prepared by mixing IFN-γ with sterile 1× PBS. Monastral blue (Sigma-Aldrich, catalog no. 274011; autoclaved and sterile filtered) was added to a final concentration of 0.03% just before injection to identify the lesion area during tissue processing. Mice were anesthetized with an intraperitoneal injection of MMF solution (0.5 mg medetomidin per kg (body weight), 5 mg midazolam per kg (body weight) and 0.05 mg fentanyl per kg (body weight)). Then the head was shaved and the eyes were protected with bepanthene cream (Bayer, catalog no. 1578847). A small incision was performed in the skin to expose the skull. The mouse was positioned into a stereotactic injection apparatus and a small hole was drilled at the injection coordinates: *X*, ±0.55 mm; *Y*, −1.22 mm (from the bregma). The glass capillary containing the IFN-γ solution or the control solution (PBS) was then lowered to *Z* of −1.25 mm from bregma, and 1 µl was injected at a rate of 100 nl min^{-1}. Then, 3 min after the delivery of the solution, the capillary was slowly retracted. The mouse was then injected with 0.05 mg of buprenorphin per kg (body weight) and the skin wound was sutured. Anesthesia was terminated by the injection of the antagonist solution, containing 2.5 mg kg^{-1} of atipamezol, 1.2 mg kg^{-1} of naloxone and 0.5 mg kg^{-1} of flumazenil. After 48 h, the animals were perfused transcardially with 4% PFA. Postfixation of brain tissue was done in 4% PFA overnight. Then the brain tissue was further cryoprotected in 30% sucrose and PBS for 24 h. The brain lesions were sectioned and stained using the same method as used in Immunohistochemistry.

Statistical analysis

For immunohistochemistry analysis three to six sections from each animal were analyzed. Data are shown as mean ± s.e.m. No statistical methods were used to predetermine sample sizes, but our sample sizes are similar to those generally employed in the field[16–20]. Each dot represents one animal. Normal distribution of the samples was tested using the Shapiro–Wilk test. For statistical analysis, paired or unpaired Student's *t*-test, or the Mann–Whitney *U*-test, was used to compare two groups. Two-sided, one-way analysis of variance (ANOVA) followed by post hoc Tukey's test was used for multiple comparisons. Test were chosen according to their distribution. In all tests a *P* value <0.05 was considered significant with $^{*}P < 0.05$, $^{**}P < 0.01$ and $^{***}P < 0.001$. Statistical analyses were done using GraphPad Prism (GraphPad Software, Inc.). Data acquisition and analysis were performed in a blinded manner. No animals were excluded from the analyses.

Reporting summary

Further information on research design is available in the Nature Research Reporting Summary linked to this article.

Data availability

The datasets we used (scRNA-seq) are deposited at the Gene Expression Omnibus (National Center for Biotechnology Information) under accession no. GSE202579. External datasets used in the present study include data from accession nos. GSE166548, GSE138891 and GSE132042. Source data are provided with this paper.

Code availability

The R code used for the analyses can be found at the github web-page: https://github.com/ISD-SystemsNeuroscience/Aging_Oligos_Microglia.

References

62. Turnbull, I. R. et al. Cutting edge: TREM-2 attenuates macrophage activation. *J. Immunol.* **177**, 3520–3524 (2006).
63. Liu, L. et al. Dissociation of microdissected mouse brain tissue for artifact free single-cell RNA sequencing. *STAR Protoc.* **2**, 100590 (2021).
64. Dobin, A. et al. STAR: ultrafast universal RNA-seq aligner. *Bioinformatics* **29**, 15–21 (2013).
65. Butler, A., Hoffman, P., Smibert, P., Papalexi, E. & Satija, R. Integrating single-cell transcriptomic data across different conditions, technologies, and species. *Nat. Biotechnol.* **36**, 411–420 (2018).
66. Huang, D. W., Sherman, B. T. & Lempicki, R. A. Systematic and integrative analysis of large gene lists using DAVID bioinformatics resources. *Nat. Protoc.* **4**, 44–57 (2009).
67. Szklarczyk, D. et al. STRING v11: protein–protein association networks with increased coverage, supporting functional discovery in genome-wide experimental datasets. *Nucleic Acids Res.* **47**, D607–D613 (2019).

68. Zhou, Y. et al. Metascape provides a biologist-oriented resource for the analysis of systems-level datasets. *Nat. Commun.* **10**, 1523 (2019).
69. Akama-Garren, E. H. et al. Follicular T cells are clonally and transcriptionally distinct in B cell-driven mouse autoimmune disease. *Nat. Commun.* **12**, 6687 (2021).
70. Stuart, T. et al. Comprehensive integration of single-cell data. *Cell* **177**, 1888–1902.e1821 2019).
71. Schindelin, J. et al. Fiji: an open-source platform for biological-image analysis. *Nat. Methods* **9**, 676–682 (2012).
72. Emery, B. & Dugas, J. C. Purification of oligodendrocyte lineage cells from mouse cortices by immunopanning. *Cold Spring Harb. Protoc.* **2013**, 854–868 (2013).

Acknowledgements

The work was supported by grants from the German Research Foundation (DFG, grant no. SI/746 15-1 to M.S.), TRR 128-2 (to M.S.), project no. 408885537-TRR 274 and SyNergy Excellence Cluster, EXC2145, project no. ID390857198 (to M.S. and O.G.), the Human Frontier Science Program (to M.S.), the ERC-ADG (grant no. 101019594 to M.S.), and the Dr. Miriam and Sheldon G. Adelson Medical Research Foundation (to M.S.), Chan-Zuckerberg Initiative grant (to M.S. and O.G.), the China Scholarship Council (CSC) fellowship program (to L.L. and H.J.) and Else Kröner-Fresenius-Stiftung grant (to O.G.). For the single-cell and sorting studies, we thank the 'Flow Cytometric Cell Sorter Sony SH800 Core Unit' run by the Department of Vascular Biology at the Institute for Stroke and Dementia Research and SyNergy EXC2145 for their support. The funders had no role in study design, data collection and analysis, decision to publish or preparation of the manuscript. We thank C. Haass for providing TREM2 knockout (KO) mice.

Author contributions

M. Simons and O.G. conceived and supervised the project. T.K., N.M., L.L., S.B.-G., H.J., S.K., O.G., J.W., L.C. and M. Schifferer performed experiments and analyzed the data. M. Simons and O.G. analyzed the data or supervised data acquisition. A.L. and J.G. provided essential reagents. M. Simons and O.G. wrote the manuscript with input from all authors.

Funding

Open access funding provided by Deutsches Zentrum für Neurodegenerative Erkrankungen e.V. (DZNE) in der Helmholtz-Gemeinschaft.

Competing interests

The authors declare no competing interests.

Additional information

Extended data is available for this paper at https://doi.org/10.1038/s41593-022-01183-6.

Supplementary information The online version contains supplementary material available at https://doi.org/10.1038/s41593-022-01183-6.

Correspondence and requests for materials should be addressed to Ozgun Gokce or Mikael Simons.

Peer review information *Nature Neuroscience* thanks Goncalo Castelo-Branco, Akiko Nishiyama, and the other, anonymous, reviewer(s) for their contribution to the peer review of this work.

Part III

DISCUSSION

The presented articles illustrate how single-cell technologies can provide a unique perspective on ageing, neurodegeneration and the role of the immune cells. As immune residents of the central nervous system, microglia have an important role in the ageing brain. Their spatial location and direct neighbourhood strongly influence their functional identity, as the micro-environment contributes to challenging the surrounding cells of the environment. In pathological condition, other non-resident immune cells penetrate the immunologically privileged parenchyma. Although a systemic approach enables a more comprehensive understanding of ageing and disease, these highly-detailed results, now achievable with single-cell technologies, challenge our definitions of cell type and cell states. Overcoming the question of documenting, representing and classifying what appears to be a continuous diversity is an ongoing challenge that the field embraces.

If the only tool you have is a hammer, you tend to see every problem as a nail.

— Abraham H. Maslow

5 AGEING WHITE-MATTER, A FERTILE SOIL FOR NEURODEGENERATION

The contribution of the immune component in the aged white-matter is still not fully understood. Nevertheless, the two publications presented in this thesis significantly contributed to further delineate and describe the role of the immune system in the brain, in the context of ageing and as premise of ulterior development of pathologies. We studied the role of the CNS-specific immune resident macrophages of the brain – the microglia – but also the perversive interruption of homeostasis by the adaptive immune system, normally exempt from the parenchymal area, but intervening in the context of ageing, and driving oligodendrocytes reaction and death. We propose a strong lead for explaining, at least partially, the diversity of the glial response and the white-matter volume loss observed in ageing.

We focused first on microglia and the specific phenotype and transcriptomic signature that they express in the aged white-matter. Originally searching for an eventual cause for the specific loss of white-matter observed in stereotactical studies in ageing, we characterised this ageing signature in contrast to the grey matter. We found a microglial population that was specific to the white-matter tissue but did not fully address the loss of white-matter volume. We then focused on oligodendrocytes, the cell type primarily constituting for the myelin formation.

We identified a population of oligodendrocytes that reacted to invading peripheral CD8 T-cells. We histologically quantified the close proximity of CD8 T cells with our oligodendrocyte population. We have shown that the presence of the adaptive immune system in the CNS is detrimental in ageing by production of interferon gamma cytokines. The newly identidied oligodendrocyte population reacted specifically in response to interferon (IRO, interferon response oligodendrocyte). We also validated experimentally the increase of interferon response from oligodendrocytes by using checkpoint inhibitors that enhanced the CD8 T cells number. Conversely, $Rag1^{-/-}$ mice, lacking functional lymphocytes, showed a reduction of the interferon response by oligodendrocytes. We further confirmed the presence of a microglial population also interferon responsive (IRM), and in proximity of CD8 T cells.

Altogether, we presented strong evidence for a decrease of the white-matter volume loss in ageing due to peripheral immune cell

invasion and its interaction with the resident microglia and oligodendrocytes, notably by secretion of detrimental cytokines in the aged brain.

Finally, we will discuss some epistemological considerations arising from the use of single-cell transcriptomics – more specifically in the microglial research field – and that are closely related to the publication of the first article on WAM microglia. The main topic discussed is the relation between the continuity of cell states observed through the prism of single-cell transcriptomics and the discretisation that is made when representing and reporting results to the scientific community.

5.1 CONTEXTUALISING OUR MICROGLIAL RESULTS

The good and the bad microglia

The microglial research field was long dominated by the dichotomous view of the M1 and M2 microglia – often personified as a "bad" and a "good" microglia, respectively – itself derived from a characterisation of macrophage activation states in peripheral tissues. The M1 phenotype describes a microglia that releases pro-inflammatory cytokines, reactive oxygen species (ROS) and nitric oxide (NO), while the M2 phenotype describes a microglia that releases anti-inflammatory cytokines and molecules involved in tissue repair, phagocytosis and extracellular matrix remodelling.

A pathological microglia signature

The microglial research field has been marked in 2017 by two transcriptomics studies that characterised the disease associated microglia (DAM) (Keren-Shaul et al., 2017) and the microglial neurodegenerative phenotype (MGnD) (Krasemann et al., 2017). They identified this microglial population in 5xFAD mice, and APP-PS1 mice, respectively, mimicking the amyloidosis, one of the hallmark of Alzheimer's disease. The DAM study was the first to employ single-cell RNA-sequencing to characterise AD-related microglia, while the MGnD study used the Nanostring technology with a limited set of pre-selected markers. The DAM/MGnD populations and single-cell phenotype has further been found in the context of other neurodegenerative diseases and – to some extent – in ageing (Mathys et al., 2019, Hammond et al., 2019, Jordão et al., 2019, Krasemann et al., 2017).

The DAM phenotype is characterised by a strong activation of less than 5% of the microglia (Keren-Shaul et al., 2017). The associ-

ated transcriptomic profile demonstrated an upregulation of genes involved in the inflammatory response, phagocytosis, and antigen presentation. These cells contribute to clearing the toxic protein aggregation but also exacerbating neuroinflammation. DAM microglia presented intracellular amyloid plaques and were releasing pro-inflammatory cytokines in their immediate environment, which can be detrimental and further promote neurodegeneration (Keren-Shaul et al., 2017).

The white-matter hypothesis and experimental design

Our study differs from the previous ones as it begins from the hypothesis of the white-matter as a main driver of the microglial diversity of response in the ageing brain. This assumption motivated the dissection and segregation of the grey and white matter from the tissue dissociation steps to the final data analysis. By retaining that tissue information, and integrating it in the analytical process, we could approach the data from the specific angle of the white-matter influence, and isolate a signature and a population of cells that was not yet characterised in previous single-cell ageing studies.[1]

[1] *The spatial information (tissue) contributes to acknowledging the micro-environment of cells as a critical factor to define the cellular transcriptomic identity. The relationship between spatial neighborhood and cell identity becomes clearer with nowadays studies.*

"Physiological ageing", the microglial case

In the WAM study, we isolated a population of microglia that specifically reacted to the white-matter degradation in ageing. These white-matter associated microglia (WAM) appeared gradually with ageing. Compared to the Alzheimer's disease DAM population, WAM exhibited a unique transcriptomic signature that is distinct from DAM, with the upregulation of genes involved in lipid metabolism, myelin phagocytosis, and the regulation of the extracellular matrix. While both DAM and WAM present some overlap in their transcriptome, these cellular states translate of different functions being executed as they were found in different locations and context in the brain.

To further understand the WAM profile, but also – in the face of the strong landmark that the DAM signature became in pathological conditions – to distinguish them further from DAM, we reanalysed microglia at different ages in a murine model of Alzheimer's disease that is more suitable for ageing the mice (APP^{NL-G-F} from Frigerio et al., 2019) which characterised the activated response microglia (ARM). While we found both populations of DAM/ARM and WAM, the WAM population appeared earlier than DAM/ARM, probably triggered by an early and gradual myelin uptake. When comparing the gene expression in those two populations, the gene enrichment pathways analysis characterised the WAM population with Cytokine

receptor, NF-κB, apoptosis and atherosclerosis pathways, while the DAM's top pathways pointed to different diseases such as Parkinson's, Huntington's and Alzheimer's disease, highlighting the associated pathological character of the DAM transcriptomic signature in contrast to the more tenuous and somehow "physiological" WAM reaction.

[2] *and this opens the translational problem*

Moreover[2], the ageing mouse model may more accurately depict the progression of microglial phenotypes during the ageing process, while the 5xFAD mouse model might be overly aggressive in its representation of Alzheimer's disease. Indeed, by overexpressing the human APP and presenilin 1 (PS1) genes – and all the mutations that each gene carry – the mice exhibit early-onset deposition of Aβ plaque from 1.5 months, with cognitive deficits from 4 to 5 months old. The 5xFAD mouse model is a very severe amyloidosis model from which mice cannot survive as long as in other AD mice models (Jankowsky and Zheng, 2017). Figure 4, page 70 shows the WAM and DAM expression with, as reference, the DAM signature genes. Taken from the supplementaries of our WAM article, this figure illustrates the large panel of response into which the DAM microglia are engaged, when the same genes are not highly expressed in WAM microglia. With this in mind, one of the comments that came up regularly is that WAM state is an intermediary state before the DAM. This would suggest that, with more time, the microglia in a WAM state would differentiate into a state more similar to DAM. Although this is to be checked further with fate mapping methods with lineage traceing, one can hardly disregard that the stimuli around the WAM microglia is different from the stimuli that DAM have to respond to, so that WAM does not necessarily produce a similar response than DAM in the context of ageing. Our more tenured and specific white-matter ageing signature might already be the more severe state engaged by microglia in normal ageing.

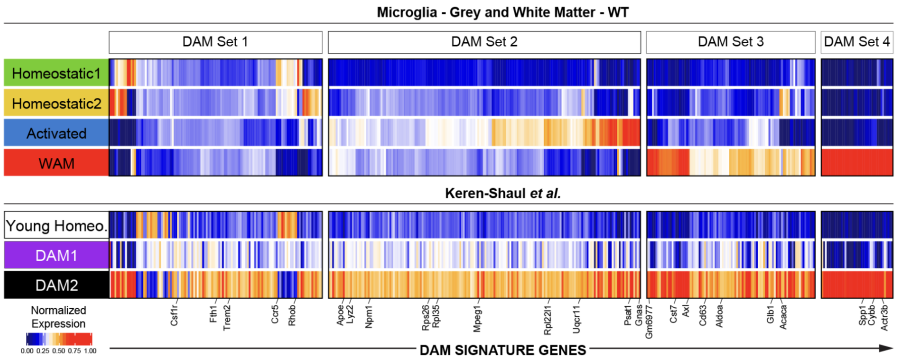

Figure 4: Heatmap of the average expression of the DAM signature comparing the WAM and the DAM clusters – reproduced from Safaiyan et al., 2021

5.1.1 *Risk factors and microglial activation*

As reminded previously, microglial states and gene expression are mainly triggered by their environment. Specific metabolic pathways and receptors have been identified. Among those, two genes particularly of interest in our case were identified as risk factors for Alzheimer's disease: Trem2 and Apoe (Long and Holtzman, 2019). The fact that these two genes have critical roles in glial cells, and notably here in microglial activation, happen to also be risk factors for AD is an indicator of the important role of microglia in ageing and emergence of disease.

The first one, is the TREM2 receptor which is critical for the formation of the full DAM2 state. To test the role of TREM2 in WAM differentiation, we used aged TREM2 knock-out mice model, into which, the WAM could not be found anymore. Moreover, our functional assays have shown that TREM2 remains necessary for WAM to fully develop and to digest myelin debris despite active phagocytic uptake functions still ongoing. During that process, they present antigen processing functions which suggests communication with other immune components that remained to be identified.

The second one is APOE, involved in the clearance of Aβ in AD. When using aged APOE knock-out mice, we could still see microglia with the WAM signature. This later result advocates for an independance of the formation of WAM and the presence of APOE protein. It is very likely that APOE is not the sole factor necessary to the clearance of myelin debris in ageing, and its absence might be less impactful for myelin clearance by microglia than it is for Aβ clearance.

Overall, WAM appear as a population that maintains the white-matter homeostasis in ageing via nodule formation and myelin debris clearing. However, this first study did not address our initial question of the white-matter volume loss during ageing. Our microglial myelin reactive population is not fully explaining the reduction of the volume of the white-matter.

5.2 ENTERS THE ADAPTIVE IMMUNE SYSTEM

To address more precisely the question of the white matter volume loss, we studied the oligodendrocytes diversity via single-cell RNA-sequencing, by combining two different technologies that both led to the same conclusions. We found, in the ageing white-matter, an oligodendrocyte population that was reacting to interferon signal (IRO). We also demonstrated that the sensitivity of oligodendrocytes to interferon gamma (IFN-γ) was specific to aged tissue. We further confirmed by immunochemistry that these IRO were found in prox-

imity of CD8 T cells that may be the producers of deleterious IFN-γ. We also characterised a microglial population that was responsive to IFN-γ (IRM). This study addresses more directly the white-matter volume loss and provides mechanistic insights. Furthermore, these results provide hypotheses for previously observed treatment results. As we used antibodies against checkpoint receptors to enhance CD8 functions, we observed an increase in CD8 T cells but also an increase in IRO and IRM populations and oligodendrocyte loss. This could explain the behavioural and cognitive changes observed in cancer treatment with checkpoint inhibitors.

5.3 AGEING AS AN IMMUNE CASCADE

While our studies still leave opened questions, such as how CD8 T cells enter the brain and what exactly triggers their migration to the brain, we provided mechanistic insights involving the adaptive immune system as a source of pathological ageing and dementia.

A recent editorial summarised that paradigm shift and illustrated our findings and the context of our research in the figure reported below (figure 5, page 72).

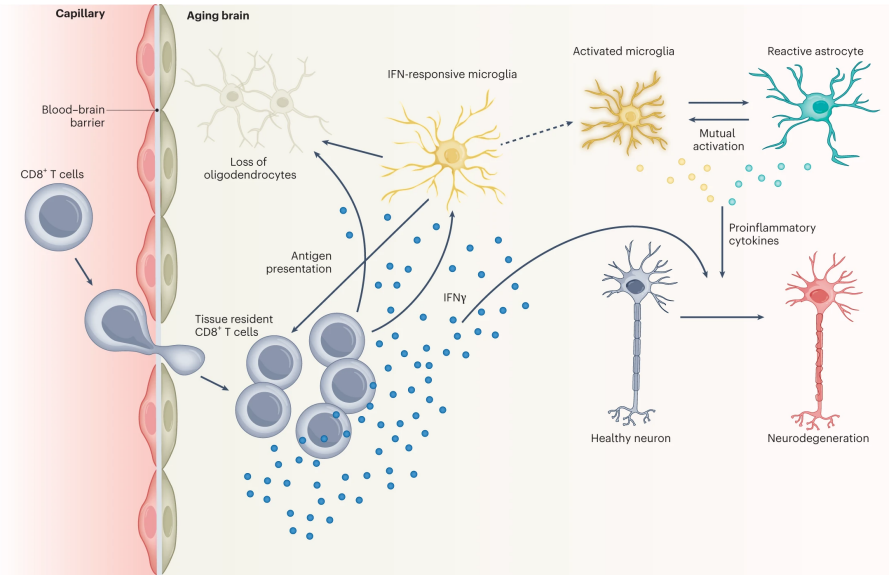

Figure 5: T cells drive ageing in the brain – reproduced from Liston and Yshii, 2023

In lieu of considering the activation of the adaptive immune system as a mere consequence of neurodegeneration, we presented a chain of events where CD8 T cells would be driving neurodegeneration. The invasion of CD8 T cells and the production of IFN-γ would lead to direct oligodendrocyte loss but also trigger the formation of an IFN-responsive oligodendrocyte and microglia popula-

tions that further positively feedback CD8 T cells by upregulating the antigen-presentation pathways in microglia. These activated microglia, could trigger astrocytosis, or they may co-inertially activate each others, leading to secretion of proinflammatory cytokines and enhancing neurodegeneration, compounding with the initial IFN-γ CD8 T cell secretion (Liston and Yshii, 2023).

5.3.1 *A viral background*

The IFN-γ, type II interferon response, is typically induced by cytokines such as IL-12 or IL-18 released by activated macrophages or microglia, and is expressed in T- and NK-cells (Fensterl and Sen, 2009). Interferon response originally occurs to interfere with the replication of a virus during infection. These mechanisms connect the T-cell IFN-γ reponse that we observed in ageing with viral infections. This link is the object of recent studies where they develop the idea of virally induced dementia on the long term. The development of dementia-related pathologies such as multiple sclerosis has been recently published where an infection with the Epstein-Barr virus (EBV) was associated with a significantly higher risk of developping multiple sclerosis (MS) (Bjornevik et al., 2022). In this study, based on a cohort of a thousand MS-diagnosed militaries and a control cohort of millions of individuals, the increased risk of developing MS was 32-fold higher after infection with the EBV.

Similarly, another study expanded this idea to a larger spectrum of neurodegenerative diseases. They identified 45 viruses associated with significantly increased risks of dementia. That study also replicated the previous EBV association with the development of MS (Levine et al., 2023).

These findings are improving our understanding of the brain and its interactions with the immune system. These viral associations highlight the importance of the history of infection of the patient. In that context, the white matter appears as a tissue that is very susceptible to immune attacks that could further lead to apparition of AD. The age dependent process can be accelerated by certain diseases and interactions of the genetics and the environment, such as viral exposure. The significance of the patient's viral exposure history brings interaction points that appear critical on the long term.

5.4 CONCLUSION

In the presented articles of this thesis, we first showed that in ageing, the most impactful change in microglia is due to myelin degeneration. We identified a population of microglia (WAM) that is

specialised in digesting and clearing myelin debris. This population increases with ageing and is transcriptomically distinct from other already described microglial population in neurodegenerative context. The absence of WAM led to myelin whorls accumulating in the brain, suggesting a mainly beneficial role of the WAM.

We also identified a population of interferon responsive microglia (IRM) and oligodendrocytes (IRO) that reacted to IFNγ cytokine secretion from invading CD8 T-cells and led to further inflammation and secretion of interferon. IRM are then presented as mainly deleterious and contributing to neuronal death. It appears that the immune privilege of the brain gets revoked in ageing, as deleterious peripheral immune cells can be found in the aged brain. The sensitivity of the white-matter to T cell invasion is of importance with regard to mechanisms of neurodegeneration, white-matter volume loss and cognitive decline in ageing.

While the specific lethal sensitivity of aged oligodendrocytes to IFNγ – compared to young ones – is not explained, the recent studies emphasising on the role of viral infections in the patient's history is echoed by the anti-viral interferon response observed in our study. The priming of T-cells in the periphery may be detrimental in ageing.

One need to remain careful of the diversity of detrimental and beneficial functions carried by microglial populations. To some extent, inflammation is a necessary process for healing. As we leave the dichotomous M1/M2 classification, technology gives us a higher resolution that leads to a continuity that is difficult to grasp.

Overall, we described a nuanced landscape of the white-matter ageing and the different actors at hand, explaining the white-matter volume loss that is characteristic of ageing. These new concepts provide a systemic paradigm for innovative therapeutical approach, and provides hope for finding both preventive and curative targets.

Solving questions as difficult as the mechanisms of ageing as a source of emerging pathologies is very likely to imply a deep understanding of the functional diversity, with the help of a map of the ageing and disease landscape (Regev et al., 2017) and the observable states herein[3]. While the WAM and the T Cell articles contributed to collecting and characterising observations in mice, a lot of work remain towards the translation to human pathologies.

[3] *while the reader might think about the empirical cell atlases, I also refer to computational models that would make up for the lack of observations but also help defining the limits of what can be observed*

OUTLOOK

6

6.1 FUNCTION OVER IDENTITY, EVOLUTION OF THE FIELD

The acronym race distraction

Following the publication of the WAM paper, our group was invited to take part in a field-wise decennial nomenclature-defining white paper. In this paper, the 96 group leaders aimed to grasp the direction of the field, and provide guidance on the future developments as to improve the ongoing collaborative effort (Paolicelli et al., 2022).

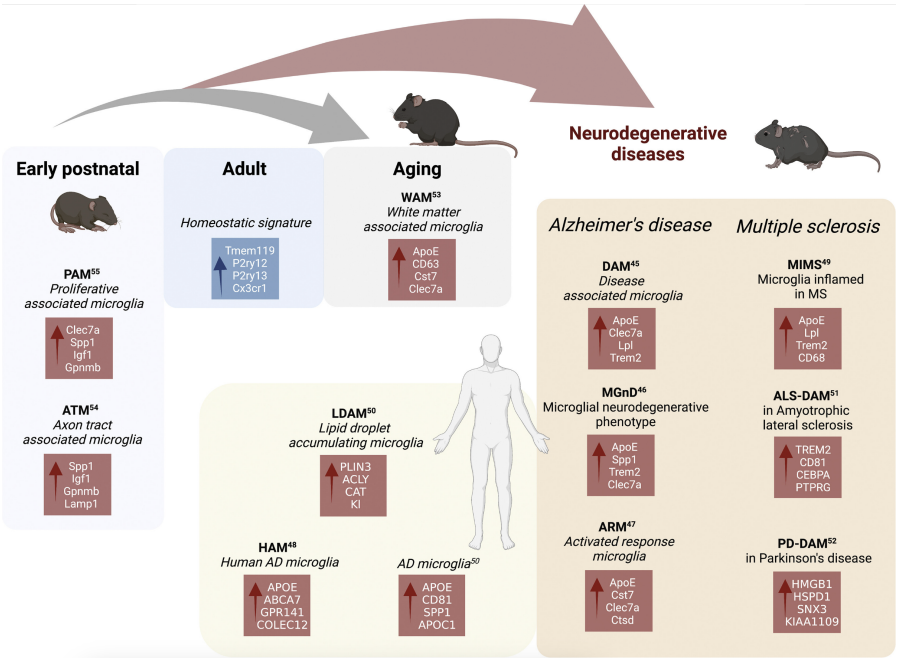

Figure 6: Microglial transcriptomic signatures – reproduced from Paolicelli et al., 2022

In this white paper, our greatest pride is the early adoption by the field of the WAM microglial population as representative of the microglial ageing state (figure 6, page 75). While the disease states were represented under multiple angles with a collection of acronyms, the mouse ageing microglial population had not yet found a representative and impactful single-cell publication before the publication of the WAM.

However, the inscription of the WAM acronym in the microglial states landscape contributed to a phenomenon which was most likely the main motivation for writing this white paper. Indeed, there is an axiomatic gap between the continuous reality of the cell states — as observed via single-cell technologies — and the reductive nature of a discrete acronym. Ultimately, the dichotomous M1/M2 classification was almost fully acknowledged as obsolete but was being replaced by another discrete and linear paradigm that settled with the milestone publication of the DAM microglia (Keren-Shaul et al., 2017). To avoid a simple substitution of the M1 vocabulary into DAM, the white paper suggests to focus instead[1] on the description of microglia in functional terms; and more specifically in reaction to environmental (or internal) triggers and adaptation of the cell to its local environment and cues.

[4] *instead of creating a new acronym to acknowledge and describe a novel state*

From cause to consequence

The proliferation of acronyms create axiomatic archetypes of microglia that can unfortunately harm research. Notably, any new observation will then be defined not for what it is by itself, but by quantifying how different it is from the predefined archetype, however big that difference might be. Especially in terms of functions, a single entity, fixed by its name, is implying a fixed associated set of functions; which goes against the idea of considering a population of microglia currently investigated in its own functional terms. Having reference points is good, and it is also important to acknowledge historical milestone discoveries. However, the profusion of acronyms can shift the focus of research from cause to consequence. By creating these archetypes, we focus on pattern matching identification (finding back the DAM in this new dataset, or in this new disease model), rather than making raw description of the cells at hand. We therefore change the focus on the cell state — the consequence[2]— instead of making a thorough investigation of the micro-environment and queues that triggered the actually observed cell states, and the specific functions carried by the cells of interest in response to this environment.

[5] *cell state as a particular configuration of gene expression in reaction to the environment*

Having a new archetype — regardless of how meticulously defined — can be similar to creating a new dichotomous M1 state. The kind of research that follows is very likely to fall into the trap of discretisation of a continuous reality and the associated binary and linear approach of our understanding of biology. Instead, we should focus on the underlying factors shaping the cellular state and the context in which these factors emerge. These factors can be for instance the location, diseases, sex, age, molecular cues, pathogens, etc., as they create

a particular context into which microglia evolve to become unique, on a continuous spectrum, carrying a large diversity of functions.

On the other hand, the continuity that we can now observe is also an infinite precipice. This is why the railguard that prevents tripping in these slippery stairs is the thinking in functional terms.

It's a fine-tuned balance. On one hand, continuity is a physical reality that needs to be taken into account when designing drugs and performing pharmacodynamic studies. On the other hand, the phenotypic outcomes are functional and more discrete in their realisation or not[3].

[6] *the presence – or functional expression – of the phenotype (or not) is a more boolean concept*

On interdisciplinary research

This continuous vision of cell states is the object of another field of research which applies physical and mathematical modelling into the description of the, now accessible, heterogeneity of cell populations (Teschendorff and Feinberg, 2021). Somehow, the smallest is the object considered, the more the mechanisms and rules fall into the physical and statistical realm (statistical mechanics, entropy, etc.). For the scale of single-cell biology, the early concept of cellular landscape from Conrad Waddington appear nowadays as a surprisingly appropriate metaphor of the mechanisms at hand and the observable reality. The term landscape is often used to characterise transcriptome overview. The recent emphasis on the importance of focusing on the functional diversity (Paolicelli et al., 2022) echoes the work of Leeland Hartwell (Hartwell et al., 1999) describing how the molecular diversity can be grouped in functional terms, and more specifically, in interconnected modules that can be defined by their functional separability, even though greatly interconnected.

During my graduate studies, I began to see how molecular and cellular biologists with their precise knowledge of the cell content and metabolism, along with computational biologists with their large-scale and high-throughput observations and modelling of the cell diversity across different modalities (genomics, transcriptomics, epigenetics, etc.), working along with the disease specialists working on ageing or Alzheimer's disease, can all enrich their practice with each their own understanding of what is actually happening at the microscopic and macroscopic levels.

BIBLIOGRAPHY

Bjornevik, Kjetil, Marianna Cortese, Brian C. Healy, Jens Kuhle, Michael J. Mina, Yumei Leng, Stephen J. Elledge, David W. Niebuhr, Ann I. Scher, Kassandra L. Munger, and Alberto Ascherio (2022). "Longitudinal analysis reveals high prevalence of Epstein-Barr virus associated with multiple sclerosis." In: *Science* 375.6578, pp. 296–301. ISSN: 0036-8075. DOI: 10.1126/science.abj8222.

Blinkouskaya, Yana, Andreia Caçoilo, Trisha Gollamudi, Shima Jalalian, and Johannes Weickenmeier (2021). "Brain aging mechanisms with mechanical manifestations." In: *Mechanisms of Ageing and Development* 200, p. 111575. ISSN: 0047-6374. DOI: 10.1016/j.mad.2021.111575.

Fensterl, Volker and Ganes C. Sen (2009). "Interferons and viral infections." In: *BioFactors* 35.1, pp. 14–20. ISSN: 0951-6433. DOI: 10.1002/biof.6.

Frigerio, Carlo Sala, Leen Wolfs, Nicola Fattorelli, Nicola Thrupp, Iryna Voytyuk, Inga Schmidt, Renzo Mancuso, Wei-Ting Chen, Maya E. Woodbury, Gyan Srivastava, Thomas Möller, Eloise Hudry, Sudeshna Das, Takaomi Saido, Eric Karran, Bradley Hyman, V. Hugh Perry, Mark Fiers, and Bart De Strooper (2019). "The Major Risk Factors for Alzheimer's Disease: Age, Sex, and Genes Modulate the Microglia Response to abeta Plaques." In: *Cell reports* 27.4, 1293–1306.e6. ISSN: 2211-1247. DOI: 10.1016/j.celrep.2019.03.099.

Ge, Yulin, Robert I Grossman, James S Babb, Marcie L Rabin, Lois J Mannon, and Dennis L Kolson (2002). "Age-related total gray matter and white matter changes in normal adult brain. Part I: volumetric MR imaging analysis." In: *American journal of neuroradiology* 23.8, pp. 1327–1333.

Hammond, Timothy R., Connor Dufort, Lasse Dissing-Olesen, Stefanie Giera, Adam Young, Alec Wysoker, Alec J. Walker, Frederick Gergits, Michael Segel, James Nemesh, Samuel E. Marsh, Arpiar Saunders, Evan Macosko, Florent Ginhoux, Jinmiao Chen, Robin J.M. Franklin, Xianhua Piao, Steven A. McCarroll, and Beth Stevens (2019). "Single-Cell RNA Sequencing of Microglia throughout the Mouse Lifespan and in the Injured Brain Reveals Complex Cell-State Changes." In: *Immunity* 1, 253–271.e6. ISSN: 1074-7613. DOI: 10.1016/j.immuni.2018.11.004. URL: https://linkinghub.elsevier.com/retrieve/pii/S1074761318304850.

Hartwell, Leland H., John J. Hopfield, Stanislas Leibler, and Andrew W. Murray (1999). "From molecular to modular cell biology." In:

Nature 402.Suppl 6761, pp. C47–C52. ISSN: 0028-0836. DOI: 10.1038/35011540.

Ionescu-Tucker, Andra and Carl W. Cotman (2021). "Emerging roles of oxidative stress in brain aging and Alzheimer's disease." In: *Neurobiology of Aging* 107, pp. 86–95. ISSN: 0197-4580. DOI: 10.1016/j.neurobiolaging.2021.07.014.

Jack, C R., M M. Shiung, S D. Weigand, P C. O'Brien, J L. Gunter, B F. Boeve, D S. Knopman, G E. Smith, R J. Ivnik, E G. Tangalos, and R C. Petersen (2005). "Brain atrophy rates predict subsequent clinical conversion in normal elderly and amnestic MCI." In: *Neurology* 65.8, pp. 1227–1231. ISSN: 0028-3878. DOI: 10.1212/01.wnl.0000180958.22678.91.

Jankowsky, Joanna L and Hui Zheng (2017). "Practical considerations for choosing a mouse model of Alzheimer's disease." In: *Molecular neurodegeneration* 12, pp. 1–22.

Jiménez, Antonio J, María-Dolores Domínguez-Pinos, María M Guerra, Pedro Fernández-Llebrez, and José-Manuel Pérez-Fígares (2014). "Structure and function of the ependymal barrier and diseases associated with ependyma disruption." In: *Tissue barriers* 2.1, e28426.

Jordão, Marta Joana Costa, Roman Sankowski, Stefanie M Brendecke, Sagar, Giuseppe Locatelli, Yi-Heng Tai, Tuan Leng Tay, Eva Schramm, Stephan Armbruster, Nora Hagemeyer, et al. (2019). "Single-cell profiling identifies myeloid cell subsets with distinct fates during neuroinflammation." In: *Science* 363.6425, eaat7554.

Keren-Shaul, Hadas, Amit Spinrad, Assaf Weiner, Orit Matcovitch-Natan, Raz Dvir-Szternfeld, Tyler K. Ulland, Eyal David, Kuti Baruch, David Lara-Astaiso, Beata Toth, Shalev Itzkovitz, Marco Colonna, Michal Schwartz, and Ido Amit (2017). "A Unique Microglia Type Associated with Restricting Development of Alzheimer's Disease." In: *Cell*. ISSN: 0092-8674. DOI: 10.1016/j.cell.2017.05.018. URL: http://www.sciencedirect.com/science/article/pii/S0092867417305780.

Kierdorf, Katrin, Daniel Erny, Tobias Goldmann, Victor Sander, Christian Schulz, Elisa Gomez Perdiguero, Peter Wieghofer, Annette Heinrich, Pia Riemke, Christoph Hölscher, Dominik N Müller, Bruno Luckow, Thomas Brocker, Katharina Debowski, Günter Fritz, Ghislain Opdenakker, Andreas Diefenbach, Knut Biber, Mathias Heikenwalder, Frederic Geissmann, Frank Rosenbauer, and Marco Prinz (2013). "Microglia emerge from erythromyeloid precursors via Pu.1- and Irf8-dependent pathways." In: *Nature Neuroscience* 16.3, pp. 273–280. ISSN: 1097-6256. DOI: 10.1038/nn.3318.

Kolodziejczyk, Aleksandra A., Jong Kyoung Kim, Valentine Svensson, John C. Marioni, and Sarah A. Teichmann (2015). "The Technology and Biology of Single-Cell RNA Sequencing." In: *Molecular Cell* 58.4, pp. 610–620. ISSN: 1097-2765. DOI: 10.1016/j.molcel.

2015.04.005. URL: http://www.sciencedirect.com/science/article/pii/S1097276515002610.

Krasemann, Susanne, Charlotte Madore, Ron Cialic, Caroline Baufeld, Narghes Calcagno, Rachid El Fatimy, Lien Beckers, Elaine O'Loughlin, Yang Xu, Zain Fanek, David J. Greco, Scott T. Smith, George Tweet, Zachary Humulock, Tobias Zrzavy, Patricia Conde-Sanroman, Mar Gacias, Zhiping Weng, Hao Chen, Emily Tjon, Fargol Mazaheri, Kristin Hartmann, Asaf Madi, Jason D. Ulrich, Markus Glatzel, Anna Worthmann, Joerg Heeren, Bogdan Budnik, Cynthia Lemere, Tsuneya Ikezu, Frank L. Heppner, Vladimir Litvak, David M. Holtzman, Hans Lassmann, Howard L. Weiner, Jordi Ochando, Christian Haass, and Oleg Butovsky (2017). "The TREM2-APOE Pathway Drives the Transcriptional Phenotype of Dysfunctional Microglia in Neurodegenerative Diseases." In: *Immunity* 47.3, 566–581.e9. ISSN: 1074-7613. DOI: 10.1016/j.immuni.2017.08.008.

Levine, Kristin S., Hampton L. Leonard, Cornelis Blauwendraat, Hirotaka Iwaki, Nicholas Johnson, Sara Bandres-Ciga, Luigi Ferrucci, Faraz Faghri, Andrew B. Singleton, and Mike A. Nalls (2023). "Virus exposure and neurodegenerative disease risk across national biobanks." In: *Neuron*. ISSN: 0896-6273. DOI: 10.1016/j.neuron.2022.12.029.

Liston, Adrian and Lidia Yshii (2023). "T cells drive aging of the brain." In: *Nature Immunology* 24.1, pp. 12–13. ISSN: 1529-2908. DOI: 10.1038/s41590-022-01390-0.

Long, Justin M. and David M. Holtzman (2019). "Alzheimer Disease: An Update on Pathobiology and Treatment Strategies." In: *Cell* 179.2, pp. 312–339. ISSN: 0092-8674. DOI: 10.1016/j.cell.2019.09.001.

Mathys, Hansruedi, Jose Davila-Velderrain, Zhuyu Peng, Fan Gao, Shahin Mohammadi, Jennie Z Young, Madhvi Menon, Liang He, Fatema Abdurrob, Xueqiao Jiang, et al. (2019). "Single-cell transcriptomic analysis of Alzheimer's disease." In: *Nature* 570.7761, pp. 332–337.

Orihuela, Ruben, Christopher A McPherson, and Gaylia Jean Harry (2016). "Microglial M1/M2 polarization and metabolic states." In: *British Journal of Pharmacology* 173.4, pp. 649–665. ISSN: 0007-1188. DOI: 10.1111/bph.13139.

Paolicelli, Rosa C., Amanda Sierra, Beth Stevens, Marie-Eve Tremblay, Adriano Aguzzi, Bahareh Ajami, Ido Amit, Etienne Audinat, Ingo Bechmann, Mariko Bennett, Frederick Bennett, Alain Bessis, Knut Biber, Staci Bilbo, Mathew Blurton-Jones, Erik Boddeke, Dora Brites, Bert Brône, Guy C. Brown, Oleg Butovsky, Monica J. Carson, Bernardo Castellano, Marco Colonna, Sally A. Cowley, Colm Cunningham, Dimitrios Davalos, Philip L. De Jager, Bart de Strooper, Adam Denes, Bart J.L. Eggen, Ukpong Eyo, Elena Galea, Sonia Garel, Florent Ginhoux, Christopher K. Glass, Ozgun Gokce, Diego

Gomez-Nicola, Berta González, Siamon Gordon, Manuel B. Graeber, Andrew D. Greenhalgh, Pierre Gressens, Melanie Greter, David H. Gutmann, Christian Haass, Michael T. Heneka, Frank L. Heppner, Soyon Hong, David A. Hume, Steffen Jung, Helmut Kettenmann, Jonathan Kipnis, Ryuta Koyama, Greg Lemke, Marina Lynch, Ania Majewska, Marzia Malcangio, Tarja Malm, Renzo Mancuso, Takahiro Masuda, Michela Matteoli, Barry W. McColl, Veronique E. Miron, Anna Victoria Molofsky, Michelle Monje, Eva Mracsko, Agnes Nadjar, Jonas J. Neher, Urte Neniskyte, Harald Neumann, Mami Noda, Bo Peng, Francesca Peri, V. Hugh Perry, Phillip G. Popovich, Clare Pridans, Josef Priller, Marco Prinz, Davide Ragozzino, Richard M. Ransohoff, Michael W. Salter, Anne Schaefer, Dorothy P. Schafer, Michal Schwartz, Mikael Simons, Cody J. Smith, Wolfgang J. Streit, Tuan Leng Tay, Li-Huei Tsai, Alexei Verkhratsky, Rommy von Bernhardi, Hiroaki Wake, Valérie Wittamer, Susanne A. Wolf, Long-Jun Wu, and Tony Wyss-Coray (2022). "Microglia states and nomenclature: A field at its crossroads." In: *Neuron* 110.21, pp. 3458–3483. ISSN: 0896-6273. DOI: 10.1016/j.neuron.2022.10.020.

Regev, Aviv, Sarah A Teichmann, Eric S Lander, Ido Amit, Christophe Benoist, Ewan Birney, Bernd Bodenmiller, Peter J Campbell, Piero Carninci, Menna Clatworthy, Hans Clevers, Bart Deplancke, Ian Dunham, James Eberwine, Roland Eils, Wolfgang Enard, Andrew Farmer, Lars Fugger, Berthold Göttgens, Nir Hacohen, Muzlifah Haniffa, Martin Hemberg, Seung K Kim, Paul Klenerman, Arnold Kriegstein, Ed Lein, Sten Linnarsson, Emma Lundberg, Joakim Lundeberg, Partha Majumder, John C Marioni, Miriam Merad, Musa Mhlanga, Martijn Nawijn, Mihai Netea, Garry Nolan, Dana Pe'er, Anthony Phillipakis, Chris P Ponting, Stephen R Quake, Wolf Reik, Orit Rozenblatt-Rosen, Joshua R Sanes, Rahul Satija, Ton N Schumacher, Alex K Shalek, Ehud Shapiro, Padmanee Sharma, Jay W Shin, Oliver Stegle, Michael R Stratton, Michael J T Stubbington, Fabian J Theis, Matthias Uhlen, Alexander van Oudenaarden, Allon Wagner, Fiona M Watt, Jonathan S Weissman, Barbara J Wold, Ramnik J Xavier, Nir Yosef, and Human Cell Atlas Meeting Participants (2017). "Science Forum: The Human Cell Atlas." In: *eLife* 6, e27041. ISSN: 2050-084X. DOI: 10.7554/elife.27041. URL: https://elifesciences.org/articles/27041http://www.ncbi.nlm.nih.gov/pubmed/29206104http://www.pubmedcentral.nih.gov/articlerender.fcgi?artid=PMC5762154.

Safaiyan, Shima, Simon Besson-Girard, Tŭgberk Kaya, Ludovico Cantuti-Castelvetri, Lu Liu, Hao Ji, Martina Schifferer, Garyfallia Gouna, Fumere Usifo, Nirmal Kannaiyan, Dirk Fitzner, Xianyuan Xiang, Moritz J Rossner, Matthias Brendel, Ozgun Gokce, and Mikael Si-

mons (2021). "White matter aging drives microglial diversity." In: *Neuron*. ISSN: 0896-6273. DOI: 10.1016/j.neuron.2021.01.027.

Teschendorff, Andrew E and Andrew P Feinberg (2021). "Statistical mechanics meets single-cell biology." In: *Nature Reviews Genetics* 22.7, pp. 459–476. ISSN: 1471-0056. DOI: 10.1038/s41576-021-00341-z.

Tremblay, Marie-Ève, Beth Stevens, Amanda Sierra, Hiroaki Wake, Alain Bessis, and Axel Nimmerjahn (2011). "The role of microglia in the healthy brain." In: *The Journal of neuroscience : the official journal of the Society for Neuroscience* 31.45, pp. 16064–9. DOI: 10.1523/jneurosci.4158-11.2011.

Verheggen, Inge C. M., Joost J. A. de Jong, Martin P. J. van Boxtel, Ed H. B. M. Gronenschild, Walter M. Palm, Alida A. Postma, Jacobus F. A. Jansen, Frans R. J. Verhey, and Walter H. Backes (2020). "Increase in blood–brain barrier leakage in healthy, older adults." In: *GeroScience* 42.4, pp. 1183–1193. ISSN: 2509-2715. DOI: 10.1007/s11357-020-00211-2.

Waddington, CH (1957). *The Strategy of the Genes*.

Yue, Nancy Chang, Alice M Arnold, William T Longstreth Jr, Allen D Elster, Charles A Jungreis, Daniel H O'Leary, Virginia C Poirier, and R Nick Bryan (1997). "Sulcal, ventricular, and white matter changes at MR imaging in the aging brain: data from the cardiovascular health study." In: *Radiology* 202.1, pp. 33–39.

Zenin, Aleksandr, Yakov Tsepilov, Sodbo Sharapov, Evgeny Getmantsev, L. I. Menshikov, Peter O. Fedichev, and Yurii Aulchenko (2019). "Identification of 12 genetic loci associated with human healthspan." In: *Communications Biology* 2.1, p. 41. DOI: 10.1038/s42003-019-0290-0.

PUBLICATIONS

Androvic, Peter, Martina Schifferer, Katrin Perez Anderson, Ludovico Cantuti-Castelvetri, Hao Ji, Lu Liu, Simon Besson-Girard, Johanna Knoferle, Mikael Simons, and Ozgun Gokce (2022). "Spatial Transcriptomics-correlated Electron Microscopy." In: *bioRxiv*, pp. 2021–05.

Benakis, Corinne, Alba Simats, Sophie Tritschler, Steffanie Heindl, Simon Besson-Girard, Gemma Llovera, Kelsey Pinkham, Anna Kolz, Alessio Ricci, Fabian J Theis, Stefan Bittner, Özgün Gökce, Anneli Peters, and Arthur Liesz (2022). "T cells modulate the microglial response to brain ischemia." In: *eLife* 11, e82031. DOI: 10.7554/elife.82031.

Ji, Hao, Simon Besson-Girard, Peter Androvic, Buket Bulut, Lu Liu, Yijing Wang, and Ozgun Gokce (2023). "High-Resolution RNA Sequencing from PFA-Fixed Microscopy Sections." In: *Neural Repair: Methods and Protocols*. Springer, pp. 205–212.

Kaya, Tuğberk, Nicola Mattugini, Lu Liu, Hao Ji, Ludovico Cantuti-Castelvetri, Jianping Wu, Martina Schifferer, Janos Groh, Rudolf Martini, Simon Besson-Girard, Seiji Kaji, Arthur Liesz, Ozgun Gokce, and Mikael Simons (2022). "CD8+ T cells induce interferon-responsive oligodendrocytes and microglia in white matter aging." In: *Nature Neuroscience*, pp. 1–12. ISSN: 1097-6256. DOI: 10.1038/s41593-022-01183-6.

Kolabas, Zeynep Ilgin, Louis B Kuemmerle, Robert Perneczky, Benjamin Förstera, Maren Büttner, Ozum Sehnaz Caliskan, Mayar Ali, Zhouyi Rong, Hongcheng Mai, Selina Hummel, Laura M Bartos, Gloria Biechele, Artem Zatcepin, Natalie L Albert, Marcus Unterrainer, Johannes Gnörich, Shan Zhao, Igor Khalin, Boris-Stephan Rauchmann, Muge Molbay, Michael Sterr, Ines Kunze, Karen Stanic, Simon Besson-Girard, Anna Kopczak, Sabrina Katzdobler, Carla Palleis, Ozgun Gokce, Heiko Lickert, Hanno Steinke, Ingo Bechmann, Katharina Buerger, Johannes Levin, Christian Haass, Martin Dichgans, Joachim Havla, Tania Kümpfel, Martin Kerschensteiner, Mikael Simons, Nikolaus Plesnila, Natalie Krahmer, Harsharan Singh Bhatia, Suheda Erener, Farida Hellal, Matthias Brendel, Fabian J Theis, and Ali Erturk (2021). "Multi-omics and 3D-imaging reveal bone heterogeneity and unique calvaria cells in neuroinflammation." In: *bioRxiv*, pp. 2021–12.

Krammer, Christine, Bishan Yang, Sabrina Reichl, Simon Besson-Girard, Hao Ji, Verena Bolini, Corinna Schulte, Heidi Noels, Kai Schlepckow, Georg Jocher, Georg Werner, Michael Willem, Omar El Bounkari, Aphrodite Kapurniotu, Ozgun Gokce, Christian Weber, Sarajo

Mohanta, and Jürgen Bernhagen (2023). "Pathways linking aging and atheroprotection in Mif-deficient atherosclerotic mice." In: *The FASEB Journal* 37.3. ISSN: 0892-6638. DOI: 10.1096/fj.202200056r.

Liu, Lu, Simon Besson-Girard, Hao Ji, Katrin Gehring, Buket Bulut, Tuğberk Kaya, Fumere Usifo, Mikael Simons, and Ozgun Gokce (2021). "Dissociation of microdissected mouse brain tissue for artifact free single-cell RNA sequencing." In: *STAR Protocols* 2.2, p. 100590. ISSN: 2666-1667. DOI: 10.1016/j.xpro.2021.100590.

Safaiyan, Shima, Simon Besson-Girard, Tŭgberk Kaya, Ludovico Cantuti-Castelvetri, Lu Liu, Hao Ji, Martina Schifferer, Garyfallia Gouna, Fumere Usifo, Nirmal Kannaiyan, Dirk Fitzner, Xianyuan Xiang, Moritz J Rossner, Matthias Brendel, Ozgun Gokce, and Mikael Simons (2021). "White matter aging drives microglial diversity." In: *Neuron*. ISSN: 0896-6273. DOI: 10.1016/j.neuron.2021.01.027.

Shrouder, Joshua James, Severin Filser, Daniel Peter Varga, Uta Mamrak, Simon Besson-Girard, Buket Bulut-Impraim, Fatma Burcu Seker, Benno Gesierich, Fabio Laredo, Antonia Clarissa Wehn, Igor Khalin, Patrick Bayer, Arthur Liesz, Ozgun Gokce, and Nikolaus Plesnila (2023). "Continued dysfunction of capillary pericytes promotes no-reflow after experimental stroke in vivo." In: *bioRxiv*, pp. 2023–03.

AFFIDAVIT

Hiermit versichere ich an Eides statt, dass ich die vorliegende Dissertation *Single-cell characterisation of ageing and disease* selbstständig angefertigt habe, mich außer der angegebenen keiner weiteren Hilfsmittel bedient und alle Erkenntnisse, die aus dem Schrifttum ganz oder annähernd übernommen sind, als solche kenntlich gemacht und nach ihrer Herkunft unter Bezeichnung der Fundstelle einzeln nachgewiesen habe.

I hereby confirm that the dissertation *Single-cell characterisation of ageing and disease* is the result of my own work and that I have only used sources or materials listed and specified in the dissertation.

Munich, 8th May 2023

Simon Besson-Girard

CONTRIBUTIONS

CONTRIBUTIONS TO THE WAM STUDY

Individual contributions: M. Simons and O.G. conceived and supervised the project. S.S., **S.B.-G.**, T.K., M. Schifferer, L.L., N.K., O.G., H.J., F.U., L.C.-C., M.J.R., R.P., G.G., M.B., D.F., and X.X. performed experiments and analyzed the data. **S.B.-G.** and T.K. developed software and curated and visualized the scRNA-seq data. O.G., M.R., and M. Simons analyzed the data or supervised data acquisition. M. Simons and O.G. wrote the manuscript with input from all authors.

In more details, as a co-first author, I established and optimised the single-cell library generation pipeline and the bionformatics data analysis pipeline that were used to generate the fundamental single-cell data in this publication. For the library generation, I contributed to the development of our protocol that includes actinomycin-D to prevent handling artefacts during the library generation. I performed the transcriptomics library generation and analyses to confirm our findings. I guided and assisted the isolation of the microglia via flow cytometry and I processed and analysed the single-cell data and categorised the different states of microglia, realising that one state was white-matter specific, I identified the WAM aging signature; thereby providing immunocytochemistry with specific markers. I provided continuous assistance to writing the manuscript.

CONTRIBUTIONS TO THE CD8 T CELL STUDY

Individual contributions: M. Simons and O.G. conceived and supervised the project. T.K., N.M., L.L., **S.B.-G.**, H.J., S.K., O.G., J.W., L.C. and M. Schifferer performed experiments and analyzed the data. M. Simons and O.G. analyzed the data or supervised data acquisition. A.L. and J.G. provided essential reagents. M. Simons and O.G. wrote the manuscript with input from all authors.

In more details, I developped and maintained the infrastructure (storage and process) necessary for the laboratory to generate the single-cell and computational data. I established and optimised the single-cell library generation pipeline and the bionformatics data analysis pipeline that were used to generate the single-cell data in this publication. For the library generation, I contributed to the development of our protocol that includes actinomycin-D to prevent handling artefacts during the library generation. I performed the oligodendro-

cytes transcriptomics library processing and analysis. I provided continuous assistance to writing the manuscript.

.....	.....	.....
Simon Besson-Girard	**Dr. Özgün Gökçe**	**Shima Safaiyan**
PhD student	**Group leader**	**Co-first author**